

LAPPEENRANTA UNIVERSITY OF TECHNOLOGY  
LUT School of Energy Systems  
LUT Mechanical Engineering

Ville Laitinen

**WELDABILITY OF POWDER BED FUSION FABRICATED STAINLESS STEEL  
316L SHEETS TO COLD ROLLED SHEET METAL**

Examiners: Prof. Antti Salminen  
D.Sc. (Tech) Joonas Pekkarinen

**ABSTRACT**

Lappeenranta University of Technology  
LUT School of Energy Systems  
LUT Mechanical Engineering

Ville Laitinen

**WELDABILITY OF POWDER BED FUSION FABRICATED STAINLESS STEEL 316L SHEETS TO COLD ROLLED SHEET METAL**

Master's thesis

2015

73 pages, 41 figures, 5 tables, and 6 appendices

Examiners: Prof. Antti Salminen  
D.Sc. (Tech) Joonas Pekkarinen

Advisor: D.Sc. (Tech) Heidi Piili

Keywords: Additive manufacturing, powder bed fusion, weldability, laser keyhole welding

Weldability of powder bed fusion (PBF) fabricated components has come to discussion in past two years due to recent developments in the PBF technology and limited size of the machines used in the fabrication process. This study concentrated on effects of energy input of welding on mechanical properties and microstructural features of welds between PBF fabricated stainless steel 316L sheets and cold rolled sheet metal of same composition by the means of destructive testing and microscopic analysis. Optical fiber diameter, laser power and welding speed were varied during the experiments that were executed following one variable at a time (OVAT) method.

One of the problems of welded PBF fabricated components has been lower elongations at break comparing to conventionally manufactured components. Decreasing energy input of the laser keyhole welding decreased elongations at break of the welded specimens. Ultimate tensile strengths were not affected significantly by the energy input of the welding, but fracturing of the specimens welded using high energy input occurred from the weld metal. Fracturing of the lower energy input welds occurred from the PBF fabricated base metal. Energy input was found to be critical factor for mechanical properties of the welds. Multioriented grain growth and formation of neck at fusion zone boundary on the cold rolled side of the weld was detected and suspected to be result from weld pool flows caused by differences in molten weld pool behaviour between the PBF fabricated and cold rolled sides of the welds.

## TIIVISTELMÄ

Lappeenrannan teknillinen yliopisto  
LUT School of Energy Systems  
LUT Kone

Ville Laitinen

### **PBF-TEKNIKALLA RUOSTUMATTOMASTA TERÄKSESTÄ 316L VALMISTETTUJEN LEVYJEN HITSATTAVUUS KYLMÄVALSSATTUIHIN LEVYIHIN**

Diplomityö

2015

73 sivua, 41 kuvaa, 5 taulukkoa ja 6 liitettä

Tarkastajat: Prof. Antti Salminen  
TkT Joonas Pekkarinen

Ohjaaja: TkT Heidi Piili

Hakusanat: Lisäävä valmistus, PBF-tekniikka, hitsattavuus, laserhitsaus

Powder bed fusion (PBF) -tekniikalla lisäävästi valmistettujen komponenttien hitsattavuus on noussut kahden viime vuoden aikana keskustelun kohteeksi PBF-tekniikassa tapahtuneen edistymisen ja kyseisessä tekniikkaa hyödyntävien koneiden kokorajoitteiden takia. Tässä tutkimuksessa keskityttiin laserhitsauksen energiantuonnin vaikutuksiin PBF-tekniikalla valmistettujen levyjen ja kylmävalssattujen levyjen välisten hitsien mekaanisissa ominaisuuksissa ja mikrorakenteissa. Sekä PBF-tekniikalla valmistetut että kylmävalssatut levyt olivat kaikki tyypin 316L ruostumatonta terästä. Hitsien ominaisuuksia tutkittiin rikkovan aineenkoetuksen ja mikrorakenneanalyysin keinoin. Optisen kuidun halkaisijaa, lasertehoa ja hitsausnopeutta varioitiin kokeiden aikana. Kokeet toteutettiin varioimalla yhtä parametria kerrallaan OVAT-metodin mukaisesti.

Yksi aiemmissa tutkimuksista todetuista ongelmista on ollut hitsattujen PBF-tekniikalla valmistettujen komponenttien murtovenymä, jonka on havaittu olevan merkittävästi perinteisillä menetelmillä valmistettujen komponenttien murtovenymiä alhaisempi. Hitsauksen lämmöntuonnin pienentämisen havaittiin nostavan murtovenymää. Murtojuuoksissa ei havaittu merkittäviä eroja lämmöntuontia muuttaessa, mutta suurilla energiantuonnin hitsit murtuivat hitsiaineesta. Pienen energiantuonnin hitsit murtuivat PBF-tekniikalla valmistetusta perusaineesta. Hitsauksen energiantuonnin todettiin olevan kriittinen tekijä hitsien mekaanisten ominaisuuksien kannalta. Hitsien multiorientoituneiden mikrorakenteiden ja kylmävalssatun perusaineen sularajalla havaitun kaulamaisen rakenteen muodostumisen arvioitiin johtuvan hitsisulassa esiintyvistä virtauksista, jotka olivat seurausta hitsisulan käyttäytymisen eroista PBF-tekniikalla valmistetun ja kylmävalssatun perusaineen välillä.

## ACKNOWLEDGEMENTS

This study was carried out as a part of the Finnish Metals and Engineering Competence Cluster (FIMECC)'s program MANU - Future Digital Manufacturing Technologies and Systems, P6 Next Generation Manufacturing. The author thanks all participants in the project for sharing their knowledge and for their input to this study.

I consider myself privileged to have worked with world-class laser processing professionals. I would like to thank examiners of my thesis Professor Antti Salminen and D.Sc. (Tech) Joonas Pekkarinen for providing me this opportunity to conduct important scientific research. I would also like to thank D.Sc. (Tech) Heidi Piili for providing me essential comments and advices as the research and experiments proceeded. Special thanks go to M.Sc. (Tech) Ville Matilainen and personnel of EOS Finland for the assistance in the fabrication of PBF sheets.

I want to ensure my gratitude to my family and friends, who were great support and encouragement during my studies at LUT.

I take this occasion to send love to Virginie.

*Ville Laitinen*

Nizza

10<sup>th</sup> of June 2015

## TABLE OF CONTENTS

### ACKNOWLEDGEMENTS

### TABLE OF CONTENTS

### LIST OF SYMBOLS AND ABBREVIATIONS

<b>1</b>	<b>INTRODUCTION .....</b>	<b>10</b>
1.1	Objectives and limitations .....	10
1.2	Research methods .....	11
1.3	Significance of the topic and used references.....	11
<b>2</b>	<b>LASER KEYHOLE WELDING .....</b>	<b>15</b>
2.1	Energy input in laser welding .....	16
2.1.1	Effect of laser welding parameters .....	16
2.2	Thermal cycle in laser welding.....	17
2.2.1	Heat conduction in the weld .....	18
2.3	Weld pool flows and keyhole behavior during laser welding .....	19
<b>3</b>	<b>WELDING METALLURGY OF AUSTENITIC STAINLESS STEELS.....</b>	<b>20</b>
3.1	Chemical composition and alloying elements of austenitic stainless steels .....	20
3.2	Weld zones.....	21
3.3	Solidification of weld metal in austenitic stainless steels.....	22
3.4	Nucleation and grain growth.....	23
3.4.1	Supercooling and constitutional supercooling .....	24
3.4.2	Microsegregation in austenitic stainless steels .....	25
3.4.3	Grain boundaries.....	25
3.5	Solidification modes .....	26
3.5.1	Primary austenitic solidification .....	27
3.5.2	Primary ferritic solidification.....	28
3.6	Prediction of weld metal microstructure.....	29

3.6.1	Effect of welding parameters on solidification.....	30
3.7	Solidification cracking in austenitic stainless steel welds .....	31
3.8	Effect of welding on alloying elements .....	32
<b>4</b>	<b>MICROSTRUCTURAL CHARACTERISTICS OF COMPONENTS FABRICATED WITH POWDER BED FUSION PROCESS.....</b>	<b>33</b>
4.1	Microstructural characteristics of additively manufactured parts.....	33
4.1.1	Density of components fabricated with PBF .....	33
4.1.2	Microstructure of austenitic stainless steel parts fabricated with PBF .....	36
4.2	Mechanical properties of components manufactured with PBF.....	38
4.3	Welding of PBF fabricated components .....	40
<b>5</b>	<b>EXPERIMENTAL SETUPS AND EXPERIMENTAL PROCEDURE.....</b>	<b>43</b>
5.1	Materials used in the study .....	44
5.2	Fabrication of PBF sheets .....	44
5.3	Laser welding of test pieces.....	46
5.3.1	Laser welding parameters .....	47
5.4	Destructive testing and microscopic examination .....	48
5.4.1	Tensile and bend test pieces and equipment .....	48
5.4.2	Microscopic examination.....	50
<b>6</b>	<b>RESULTS AND DISCUSSION .....</b>	<b>52</b>
6.1	Microstructural analysis of the welds .....	54
6.1.1	Predicted solidification of produced welds.....	55
6.1.2	Detected weld solidification .....	56
6.1.3	SEM analysis .....	57
6.1.4	Ferrite contents of the welds.....	58
6.2	Results of the bend tests.....	59
6.3	Results of the tensile tests .....	60
6.3.1	Fracturing of the tensile test samples.....	61

**7 CONCLUSIONS ..... 63**  
**8 FURTHER STUDIES ..... 65**  
**REFERENCES ..... 66**

**APPENDICES**

APPENDIX I: STRESS RELIEVING HEAT TREATMENT.

APPENDIX II: USED LASER WELDING PARAMETER SETS.

APPENDIX III: WELD MACROGRAPHS.

APPENDIX IV: WELD MICROGRAPHS.

APPENDIX V: ENERGY-DISPERSIVE ANALYSIS.

APPENDIX VI: RESULTS OF THE TENSILE TESTS.

## LIST OF SYMBOLS AND ABBREVIATIONS

$E$	Energy input	[J/mm]
$P$	Laser power	[W]
$T_l$	Temperature of the liquid	[°C]
$T_m$	Melting temperature of the liquid metal	[°C]
$v$	Welding speed	[mm/min, mm/s]
$\delta$ -ferrite	Delta-ferrite	
3D	Three dimensional	
A	Austenitic solidification	
A-F	Austenitic-ferritic solidification	
AM	Additive manufacturing	
C	Carbon	
CR	Cold rolled	
Cr	Chromium	
$Cr_{eq}/Ni_{eq}$	Chromium/nickel equivalent	
$Cr_{eq}$	Chromium equivalent	
Cu	Copper	
DMLS	Direct metal laser sintering	
EDA	Energy-dispersive analysis	
F	Ferritic solidification	
F-A	Ferritic-austenitic solidification	
F-A-F	Ferritic-austenitic-ferritic solidification	
FBB	Face bend test specimen of butt weld	
FIMECC	Finnish Metals and Engineering Competence Cluster	
HAZ	Heat affected zone	
HCF	High cycle fatigue	
L	Liquid	
LAM	Laser additive manufacturing	
MGB	Migrated grain boundary	
Mn	Manganese	

<i>Mo</i>	Molybdenum
<i>N</i>	Nitrogen
<i>Nb</i>	Niobium
<i>Nd:YAG</i>	Neodymium-doped yttrium aluminium garnet
<i>Ni</i>	Nickel
<i>Ni<sub>eq</sub></i>	Nickel equivalent
<i>OVAT</i>	One variable at a time
<i>PA</i>	Flat welding position
<i>PBF</i>	Powder bed fusion
<i>RBB</i>	Root bend test specimen of butt weld
<i>RP</i>	Rapid prototyping
<i>SEM</i>	Scanning electron microscope
<i>SGB</i>	Solidification grain boundary
<i>SLM</i>	Selective laser melting
<i>S/L</i>	Solid-liquid interface
<i>SSB</i>	Solidification subgrain boundary
<i>Si</i>	Silicon
<i>Ti</i>	Titanium
<i>WDA</i>	Width-depth area
<i>WDR</i>	Width-depth ratio
<i>wt%</i>	Weight percent
<i>Yb</i>	Ytterbium

## 1 INTRODUCTION

Additive manufacturing (AM) was invented during 1980s, when it was mainly used in production of prototypes (rapid prototyping, RP) (Gibson, Rosen & Stucker, 2010, p. 34). Even though additive manufacturing was developed for prototyping, it has proven its capability in fabrication of complex structures from large variety of materials. Material is added layer by layer to form a three dimensional (3D) object in additive manufacturing, which has led to naming of AM in media as 3D printing. Consumer printers (usually plastic materials) have become common during past decade due to expiration of some of the standards concerning AM.

Laser additive manufacturing (LAM) of metals has been adopted by high-demand industries such as aircraft manufacturers, dental prosthesis manufacturers and tool manufacturers in production of molds and end-products. LAM has made possible the manufacturing of weight and shape optimized structures. Fabrication of components using LAM is time consuming, and the size of the parts is limited comparing to conventional methods. Aspiration to manufacture complex high technology products without losing productivity and cost effectiveness has raised question about weldability of parts fabricated using LAM. Welding of LAM components to other LAM or conventionally manufactured components enables the utilization of AM in bigger structures, and may encourage adaptation of the technology in the manufacturing industries. However, there are only few studies about weldability of LAM components.

### 1.1 Objectives and limitations

The objective of this research was to study weldability of laser additive manufactured (Powder Bed Fusion process, PBF) stainless steel 316L components with cold rolled sheet metal components of same composition. The goal of this study was to provide information about effects of energy input during laser welding on mechanical properties of the welds and microstructural features of the welds. This study concentrates only on material weldability. Hardness and pendulum impact testing of the welds were left out of the study due to material properties of austenitic stainless steels.

Research questions of the study are:

1. What kind of studies has been executed about weldability of PBF components, and what is the general knowledge about the topic?
2. Is laser welding of PBF fabricated stainless steel 316L sheets and cold rolled sheet metal of same composition feasible?
3. What are the characteristics of weld solidification in welds between PBF fabricated stainless steel 316L sheets and cold rolled sheet metal of same composition?
4. Does energy input of the welding affect the ultimate tensile strength, elongation at break or fracturing of the welds between PBF fabricated stainless steel 316L sheets and cold rolled sheet metal of same composition?

## 1.2 Research methods

This study consists of two main sections: literature review and experimental part. Literature review introduces basics of heat input in welding and material flow during laser keyhole welding in chapter 2, welding metallurgy of austenitic stainless steels in chapter 3, and microstructural features of components fabricated with PBF and previous studies about weldability of PBF components in chapter 4. The objective of the literature review is to gain information from previous studies for the support of analysis of results of this study. Information presented in the literature review is based on scientific articles and textbooks. Reliability of the references is examined.

Welding experiments are implemented using laser keyhole welding. Varied parameters were optic fiber diameter, laser power and welding speed. Observation of effects of individual parameters on results of the study was enabled by use of one variable at a time (OVAT) method in the experiments. Destructive testing, microscopic examination and energy-dispersive analysis are used to study mechanical and microstructural properties of the welds.

## 1.3 Significance of the topic and used references

Reliability of references was ensured by use of recent scientifically relevant articles, books and conference papers. Information was gathered from multiple sources, and scientific accuracy of the information was ensured by use of cross referencing. Information was gathered from scientifically relevant databases, such as Science Direct, SpringerLink

eJournals, Google Scholar, IOPscience and Scopus. Scopus was also used for analysis of sources and general structure (type, year and country) of the literature concerning searched topics. Analysis of literature about searched topic was divided to two main sections: additive manufacturing and cross section of additive manufacturing and welding.

Scopus searches were executed using search terms:

- "powder bed fusion" OR "additive manufacturing"
- "additive manufacturing" OR "powder bed fusion" AND "welding" OR "weldability"

Purpose of using powder bed fusion and additive manufacturing as search terms was based on the information about additive manufacturing being relatively new topic of research in scientific community. Literature search using search term "powder bed fusion" OR "additive manufacturing" resulted 2580 documents. Most of the documents about the topic were produced in United States, United Kingdom, Germany and China in descending order. Amount of scientific documents published annually is visible in figure 1. It can be detected that amount of scientific documents published annually has been growing rapidly since year 2010.

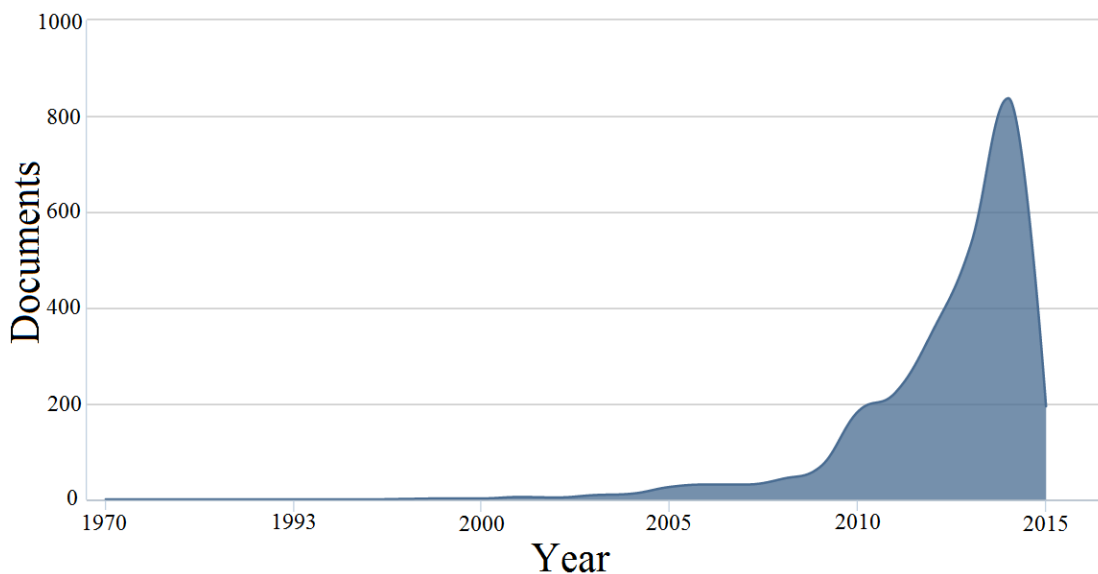


**Figure 1.** Documents published annually in the SCOPUS database that include the search term "powder bed fusion" OR "additive manufacturing" (modified from: Scopus, 2015).

Diagram in the figure 2 specifies types of documents published about additive manufacturing. Majority of documents published about additive manufacturing or powder bed fusion appear to be conference papers or scientific articles (total of 88.3 %), and only few books have been published about the topic. This supports the fact that additive manufacturing is relatively new topic of research, and most of the documents available in the used databases will be either scientific articles or conference papers. Analytical comparison of information obtained from the literature is required for ensuring of relevancy and veracity of the information.

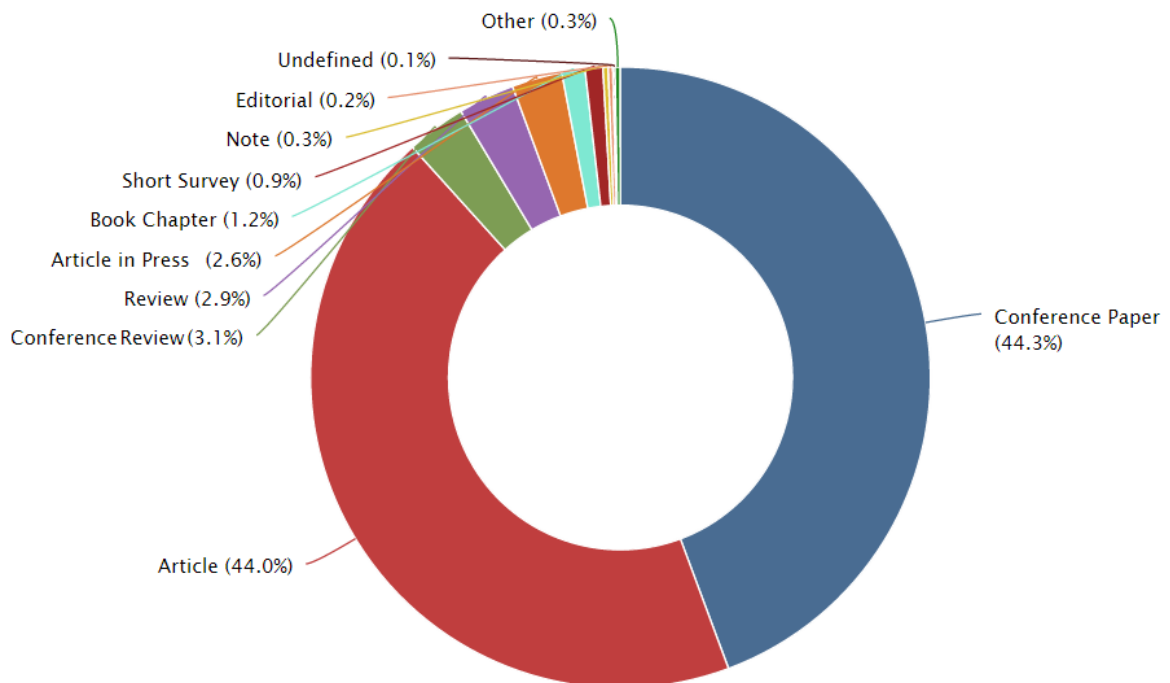


**Figure 2.** Documents published annually in the SCOPUS database that include the search term "powder bed fusion" OR "additive manufacturing" (Scopus, 2015).

Welding of powder bed fusion fabricated components could be defined to be totally new area of research due to research of additive manufacture being relatively new area of research. However welding of conventionally manufactured materials has been studied enormously, and most of the articles and books about welding date back to years 1970-2015. Search about welding of additively manufactured parts was performed in Scopus using search term "additive manufacturing" OR "powder bed fusion" AND "welding" OR "weldability", and it resulted 138 documents. Only two of the documents were related to

the topic of welding of additively manufactured pieces. Most of the search results only included a word from the search term (typically a reference of powder bed fusion being microscale laser welding). This is why this thesis has a huge industrial potential, as it provides new knowledge of such application which is not well known.

## 2 LASER KEYHOLE WELDING

Laser beam is reflected, absorbed and transmitted during the interaction between welded material and laser beam. Energy of absorbed laser beam transforms into heat in the welded material that is melted and evaporated due to high energy density of focused laser beam ( $10^{10}$ - $10^{12}$  W/m<sup>2</sup>). Evaporation of the welded material causes pressure that leads to formation of keyhole in surrounding molten material. Keyhole is sustained by the same pressure. Structure of the formed keyhole is cavity-like, which leads to multiple reflections of radiation of laser beam inside of the keyhole. Absorption of the laser beam to the welded material is high (even 99 %) inside of the keyhole due to this phenomenon. Movement of the laser beam along direction of the weld leads to melting and evaporation of the solid material in front of the keyhole. Simultaneously the molten material behind the keyhole begins to cool and solidify forming the weld. Principle of behavior of laser keyhole in laser welding is illustrated in figure 3. (Ion, 2005, p. 396-397; Steen & Mazumder, 2010, p. 199 and 202-203.)

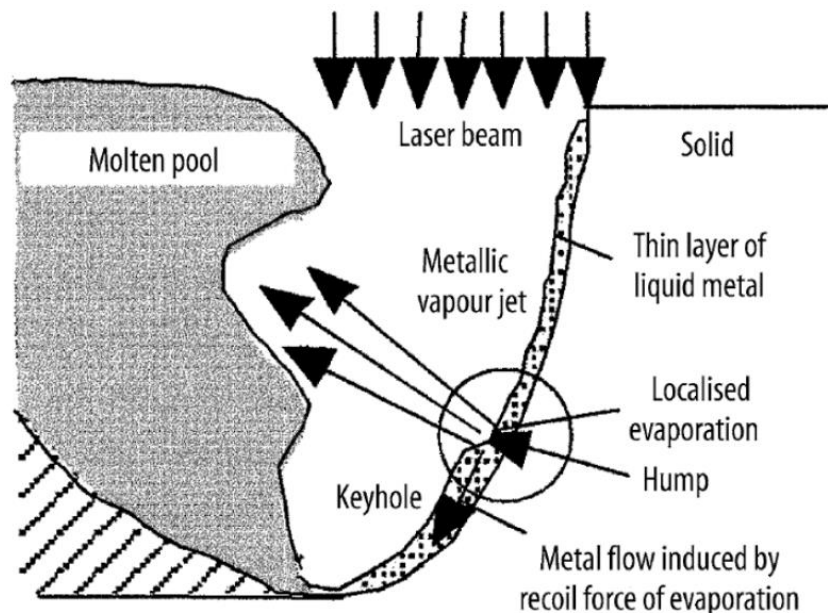


**Figure 3.** Shape of the keyhole produced by focused laser beam (Matsunawa, 2002).

## 2.1 Energy input in laser welding

Heat input of laser welding depends on absorption of laser beam to welded material, laser power and welding speed. However, determination of absorption is inaccurate because of dependence of absorption on multiple factors, such as laser beam wave length, temperature, surface films of the material, angle of incidence and material surface roughness (Steen & Mazumder, 2010, p. 90-93). Use of energy input instead of heat input enables comparison of results freely without errors caused by inaccurate determination of absorption. Energy input  $E$  in laser welding can be calculated as follows:

$$E = \frac{P}{v} \quad (1)$$

In the equation 1  $P$  is laser power and  $v$  is welding speed. (modified from: Dahotre & Harimkar, 2008, p. 317; Hafez & Katayama, 2009, p.70; Kujanpää & Salminen & Vihinen, 2005, p. 44.)

### 2.1.1 Effect of laser welding parameters

Laser power is one of the most important process parameters in laser welding. Laser power combined with welding speed defines energy input of the welding, and therefore are affecting most of the characteristics and phenomena (keyhole behaviour, molten pool size and shape, penetration depth and width of the weld) occurring during laser welding process. Welding speed has been observed to affect the formation of weld defects, such as porosity, spattering, humping and cracking (Kawahito, Mizutani & Katayama, 2007, p. 13). Increase in laser power and/or decrease in welding speed increases energy input and also heat input of the welding. (Dahotre & Harimkar, 2008, p. 434-435 and 437; Hafez & Katayama, 2009, p. 70; You et al., 2014, p. 50.)

Diameter of the used optical fiber defines diameter of raw laser beam and therefore affects the achieved focal spot diameter. Increase in diameter of optical fiber increases the focal spot diameter and decreases the power density in the focal spot by increasing the area where the laser power is divided. Decreasing power density reduces achieved penetration of the weld and increases width of the weld. Focal spot position has been found to affect keyhole geometry. Effects of welding speed and laser beam diameter to formation of weld

defects and achieved weld penetration are illustrated in figure 4. (Kawahito & Mizutani & Katayama, 2007, p.12-13; Vänskä et al., 2013, p. 202-204 and 207.)

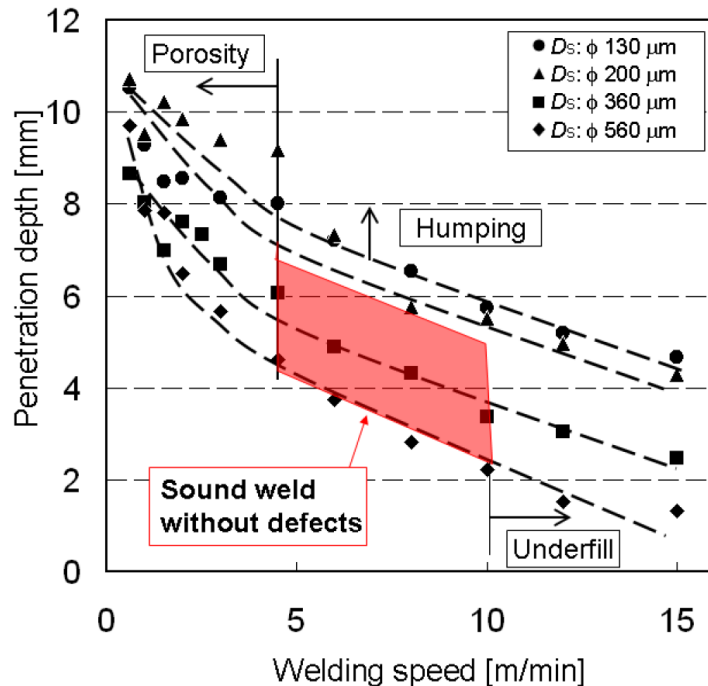


**Figure 4.** Effect of laser beam diameter and welding speed on penetration and formation of various weld defects. Beam was focused on the work piece surface, and used fiber laser power was 6 kW. (Kawahito, Mizutani & Katayama, 2007, p. 13.)

## 2.2 Thermal cycle in laser welding

Heat input during welding affects cooling rate and solidification of the welded material. Increasing heat input decreases cooling rate of the weld, and therefore may affect the solidification mode in the weld fusion zone. Welded material exposes to thermal cycle during welding, which begins with introduction of energy (focused laser beam in the case of laser welding) that transforms to heat in the material. Creation of heat in the welded material leads to evaporation and melting, and the material cools after laser beam is moved in the direction of welding. Heat input of the laser welding is relatively even in different parts of the weld due to absorption of laser beam to full length of the keyhole boundary. Conduction of heat in laser welding of thin plates is parallel to plate surfaces (two dimensional heat flow), which differs from multidirectional conduction of heat (three dimensional heat flow) in arc welding where heat is brought to welded plates from one direction by the electric arc. Differences in heat input in different parts of weld and effect

of increasing heat input on cooling rate are illustrated in figure 5. (Chandel & Bala, 1985, p. 207s-208s; Rai et al., 2008, p. 107; Signes, 1972, p. 474s; Steen & Mazumder, 2010, p. 203.)

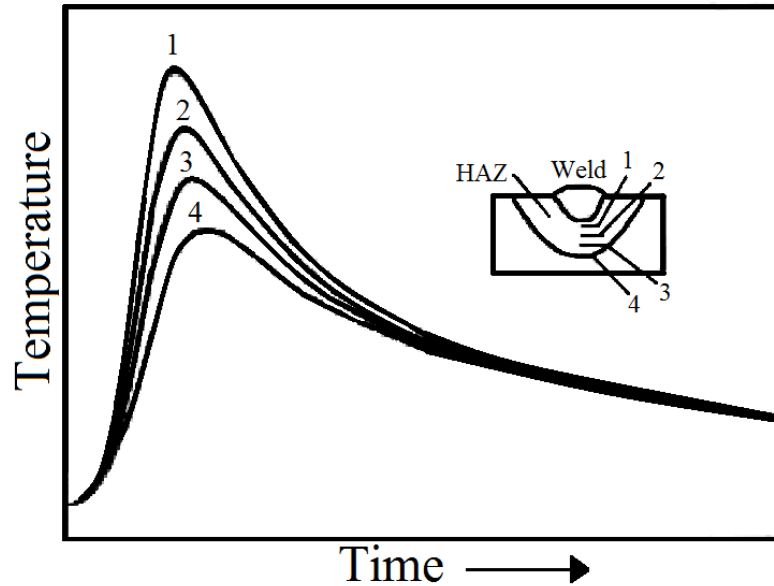


**Figure 5.** Thermal cycle in welding. Heat input decreases from point 1 to 4. (modified from: ASM International, 1993, p. 180.)

Cooling rate of the weld can be described as a function of heat gradient and solidification rate, which depends on welding speed and angle of solidification boundary during welding. Heat gradient describes cooling rate and direction of cooling in a specified point of a weld. Cooling rates in laser welding are high (1000-10000 °C/s) comparing to arc welding due to lower heat input of laser welding (Kujanpää, 2014, p. 631). Cooling time extends due to increase in the size of heat gradient, which depends on heat conductivity of the welded material and increases when laser power is being decreased and/or welding speed is being increased. Therefore magnitude of the heat gradient is defined by heat input of the welding. (Rai et al., 2008, p. 107.)

### 2.2.1 Heat conduction in the weld

Heat is generated at the boundary between molten metal and keyhole, where from it spreads in to the molten metal. Heat leaves the weld mainly by conduction trough boundaries between molten and solid metal. Heat is transferred from the boundary between

keyhole and molten metal to boundary between molten and solid metal due to flows of molten material in the molten weld pool. Conduction of heat from keyhole boundary to solid metal through weld pool does not occur due to high welding speeds of laser welding. (Piekarska & Kubiak, 2012, p. 163-165; Rai et al., 2008, p. 103; Steen & Mazumder, 2010, p. 203.)

### 2.3 Weld pool flows and keyhole behavior during laser welding

High fluid velocities and turbulent molten weld pool may occur during laser welding due to high surface tension and heat gradients on the weld pool surface caused by high energy density of the focused laser beam (Kumar & Debroy, 2005, p. 2726-2728). Keyhole and melt pool behaviour are mainly defined by used welding speed, but the amount of molten material in the weld pool is defined by used laser power. Welding speeds lower than 5 m/min usually produce relatively large molten pool comparing to size of the cylindrical keyhole. Molten pool behaviour is detailed by turbulent surface fluctuations, swellings and spattering. This type of melt pool and keyhole behaviour is called Rosenthal regime (figure 6). Full penetration welds usually have typical elongated and widened areas of molten pool formed by surface tension gradient driven Marangoni convection on the top and bottom regions of the weld. (Fabbro, 2010, p. 2; Ki, Mohanty & Mazumder, 2002, p. 1838-1839; Rai et al., 2008, p. 103.)

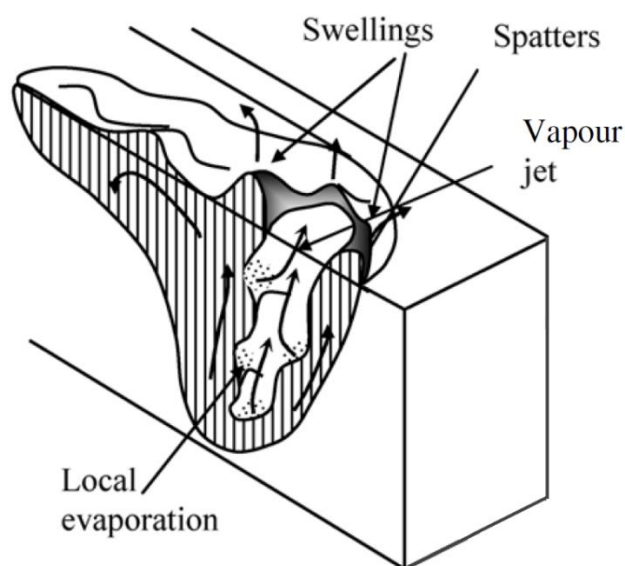


**Figure 6.** Rosenthal regime and melt pool flows in laser welding (modified from: Fabbro, 2010, p. 2).

### 3 WELDING METALLURGY OF AUSTENITIC STAINLESS STEELS

Stainless steels are divided to five groups based on room temperature microstructure of the metal. The five groups of stainless steels are austenitic stainless steels, ferritic stainless steels, martensitic stainless steels, austenitic-ferritic stainless steels (duplex) and precipitation hardening stainless steels. Majority of the stainless steels belong to the group of austenitic stainless steels. (Outokumpu, 2013, p. 11-13; SFS-EN 10088-1, 2014, p. 43-44.)

#### 3.1 Chemical composition and alloying elements of austenitic stainless steels

Alloying elements of austenitic stainless steels are divided to two main groups: austenite-promoting alloying elements and ferrite-promoting alloying elements. Corrosion resistance of stainless steels is mainly provided by chromium. Chromium is a strong ferrite promoter and also associated with formation of carbides (chromium-carbide precipitates) in stainless steels. Molybdenum improves strength in elevated temperatures, increases corrosion resistance and promotes ferritic microstructure. Silicon promotes ferritic microstructure, and is added to stainless steel alloys to prevent oxidation during melting and increase fluidity of molten metal. Titanium and niobium act as carbide formers, improve corrosion resistance and stabilize carbon, therefore promoting ferritic microstructure. (Lippold & Kotecki, 2005, p. 20-25; McGuire, 2008, p. 70-72; Outokumpu, 2013, p. 14-15; SFS-EN 10088-1, 2014, p. 45.)

Nickel is a strong promoter of austenitic microstructure. It is primary used for stabilizing austenite and enable austenitic microstructure in chromium alloyed stainless steels. Manganese is typical alloying element in all stainless steels, and it stabilizes austenite effectively in low temperatures. Carbon increases ductility of stainless steel and it promotes austenitic microstructure. Designated L-grades have lowered carbon content to prevent intergranular corrosion caused by precipitation of carbides. Nitrogen is added to some austenitic stainless steels to improve strength but it is commonly found from most alloys as an impurity. Nitrogen promotes austenitic microstructure. Typical composition of austenitic stainless steels is presented in table 1. (Lippold & Kotecki, 2005, p. 20-25; McGuire, 2008, p. 70-72; Outokumpu, 2013, p. 14-15; SFS-EN 10088-1, 2014, p. 45.)

Table 1. Typical composition of alloying elements in austenitic stainless steels (Lippold & Kotecki, 2005, p. 142).

Cr	16 to 25 wt%
Ni	8 to 20 wt%
Mo	0 to 2 wt%
Mn	1 to 2 wt%
C	0.02 to 0.08 wt%
N	0 to 0.15 wt%
Si	0.5 to 3 wt%
Ti and Nb	0 to 0.2 wt%

### 3.2 Weld zones

The basic principle of welding is to introduce welded materials to local heating (focused laser beam, electron beam, electric arc or friction and pressure) which rapidly melts material. Moving heat source leads to rapid cooling of the material and solidification of the molten metal. Heat is only introduced to region of weld (weld, fusion zone and heat affected zone) where it spreads to surrounding metal causing local rise in the temperature and therefore microstructural changes. Microstructures of weld, fusion zone and heat affected zone diverge from the base material. Illustration of weld zones is presented in figure 7.

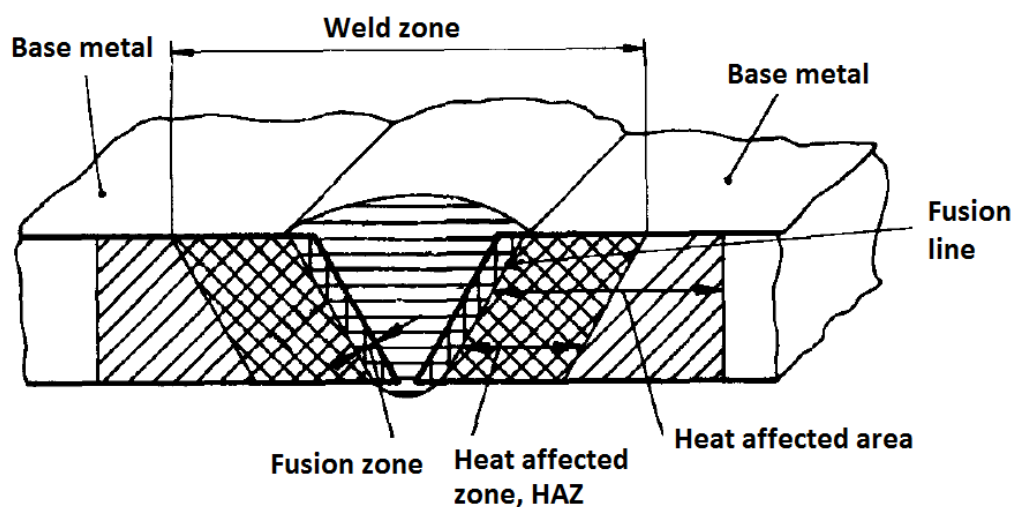
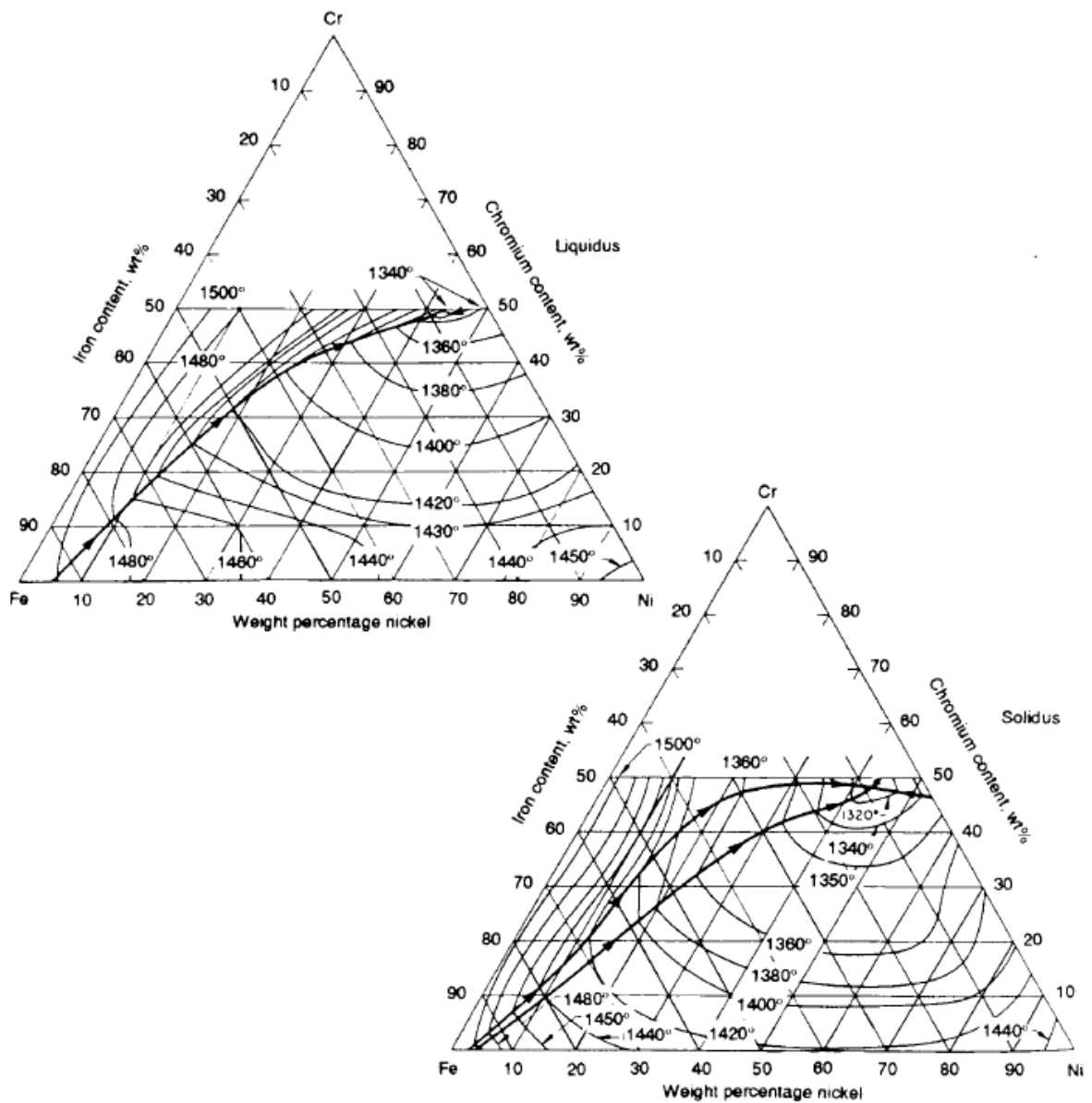


Figure 7. Weld zones (modified from: SFS 3052, 1995, p. 42-43).

### 3.3 Solidification of weld metal in austenitic stainless steels

Solidification of austenitic stainless steel begins at liquidus temperature, where first nucleuses start to form, and ends at solidus temperature. Liquidus and solidus temperatures depend on composition of the material. Each material has its own liquidus and solidus temperatures, and the liquidus and solidus can be defined for alloyed material based on the knowledge of composition of the alloying elements. Liquidus and solidus projections for austenitic stainless steels are presented in figure 8. (Kyröläinen & Lukkari, 2002, p. 65; Lippold & Kotecki, 2005, p. 12-15.)



**Figure 8.** Fe-Cr-Ni ternary system: liquidus and solidus projections (modified from: Lippold & Savage, 1979, p. 363s).

### 3.4 Nucleation and grain growth

Formation of grains in molten metal begins with formation of first nucleuses when temperature of the molten material cools down below liquidus temperature at solid-liquid interface. Material around nucleuses begins to solidify initiating grain growth that continues perpendicularly against solid-liquid interface. Growth of grains during weld solidification happens maintaining crystallographic orientation of the original grain due to epitaxial nucleation and competitive grain growth mechanism. Competitive grain growth is a result from grains aspiration to grow in the direction of original grain (direction  $\langle 100 \rangle$ ) due to minimal energy requirement of this direction. Grains growing in this direction outcome the grains growing in other directions causing the uniform grain growth. Orientation of solid-liquid interface and grain growth depend on melt pool shape, which is defined by heat flow in the material, heat input of the welding, and welding speed. Grain growth and movement of solid-liquid interface happens from edge of the weld towards centerline of the weld. Grain growth during solidification is illustrated in figure 9. (Elmer, Allen & Eagar, 1989, p. 2124-2125; Lippold, 2014, p. 24-25; Nelson & Lippold & Mills, 1999, p. 330s-331s.)

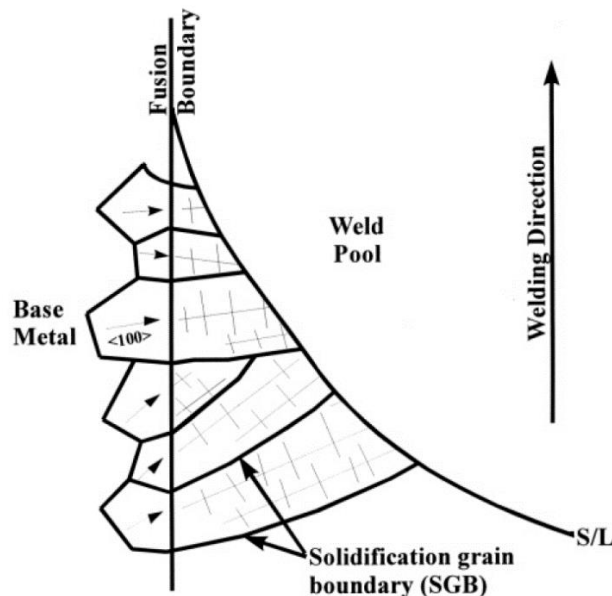


**Figure 9.** Epitaxial nucleation and competitive growth in weld fusion zone (Nelson & Lippold & Mills, 1999, p. 330s).

### 3.4.1 Supercooling and constitutional supercooling

Continuous solidification of weld requires temperature of liquid metal in front of solid-liquid interface to be under liquidus temperature. Supercooling of solid-liquid interface can happen two different ways: heat removal by conduction through solidified grains or heat removal by both conduction through solidified grains and conduction to liquid metal. Heat removal only by conduction through solidified grains is possible when temperature of liquid metal is above liquidus temperature. Heat removal from solid-liquid interface by both ways can happen only when both grains and liquid metal are cooled below liquidus temperature. This type of supercooling is related with dendritic grain growth. (Miekk-oja, 1986, p. 229 and 230.)

Constitutional supercooling is related with growth of grains in alloyed weld metal during solidification. Growing grain consumes certain alloying elements from liquid metal causing the concentrations of alloying elements to change in liquid metal near solid-liquid interface (microsegregation). Melting point of the liquid metal next to solid-liquid interface is lower than melting point of the liquid further away in weld pool, because solidus and liquidus temperatures of the alloy depend on concentration of alloying elements. Temperature of liquid metal ( $T_l$ ) is lower than melting point of liquid metal ( $T_m$ ) enabling grain growth in liquid metal higher temperature comparing to solid-liquid interphase. Constitutional supercooling is presented in figure 10. (Glicksman, 2011, p. 225-226 and 234; Miekk-oja, 1986, p. 233-234.)

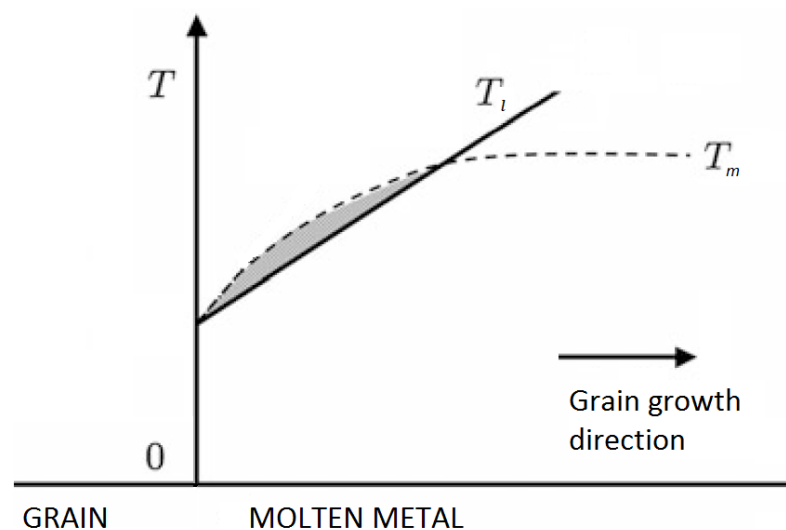


**Figure 10.** Constitutional supercooling (modified from: Glicksman, 2011, p. 226).

### 3.4.2 Microsegregation in austenitic stainless steels

Concentrations of alloying elements and impurities vary between solidified and liquid phases of the material during weld solidification. Cooling rates in the welding are too high to support homogeneous solidification of the weld causing the segregation of the elements during solidification process. Differences in concentrations of alloying elements between liquid and solid phases begin to increase when solidification of grains (austenite or ferrite) begins to consume promoting elements from surrounding molten material. Segregation of different alloying elements diverges depending on solidification mode as it appears from figure 11: austenite consumes austenite promoting elements, and ferrite consumes ferrite promoting elements. Consumption of certain elements from the liquid phase causes the concentration of the liquid material to change. (Brooks, 1990, p. 41-47; Kyröläinen & Lukkari, 2002, p. 70.)

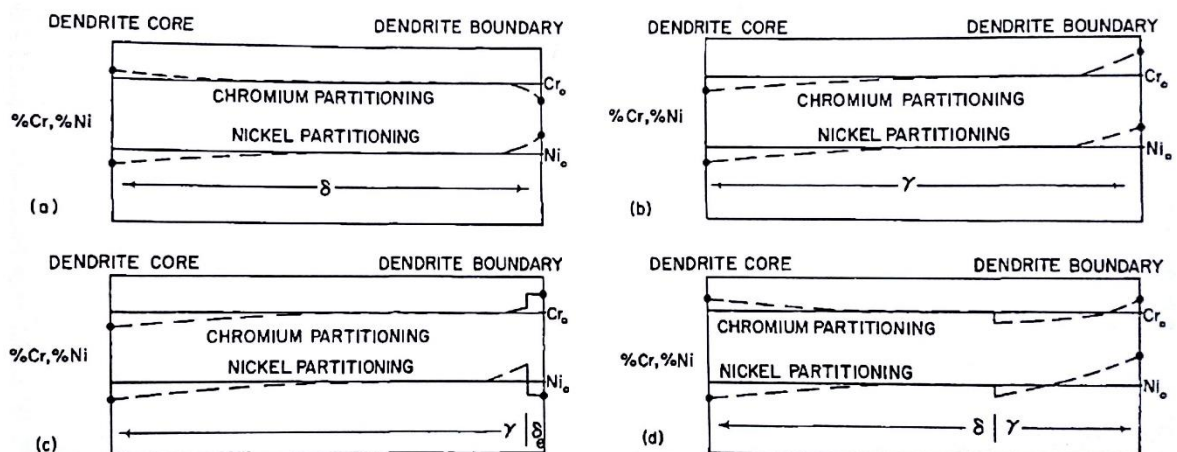


**Figure 11.** Microsegregation of chromium and nickel during different solidification modes. a) Fully ferritic solidification, b) Fully austenitic solidification, c) Austenitic-ferritic solidification, and d) Ferritic-austenitic solidification. (Cieslak & Ritter & Savage, 1982, p. 8s.)

### 3.4.3 Grain boundaries

Weld solidification leads to existence of various grain boundaries in room temperature microstructure (figure 12). Solidification grain boundaries (SGB) are located between individual dendrites created by grain growth. Solidification subgrain boundaries (SSB) are located between single dendrite arms, and are visible especially when solidification is primary austenitic. Migrated grain boundaries (MGB) form at the end of solidification and

are misoriented comparing to direction of grain growth. (Lippold & Kotecki, 2005, p. 162-163.)

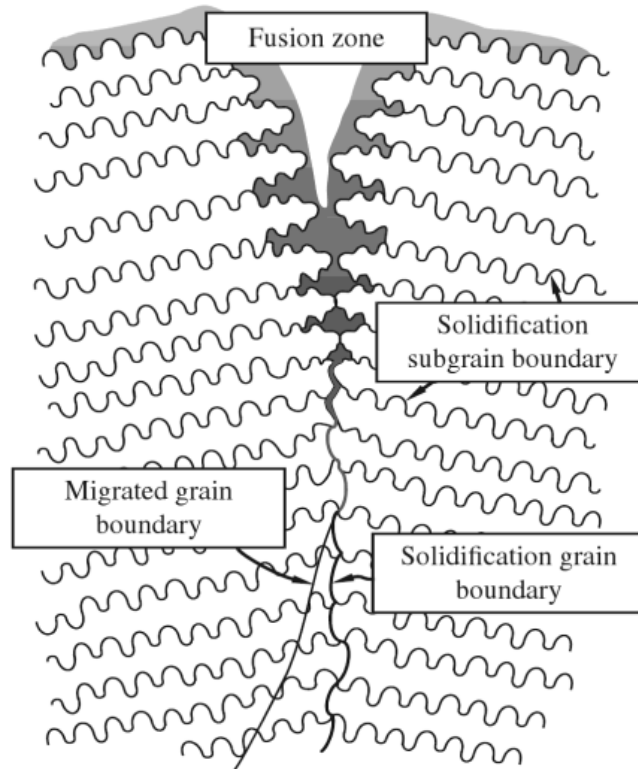


**Figure 12.** Grain boundaries formed by primary austenitic solidification (Lippold, 2014, p. 33).

### 3.5 Solidification modes

Austenitic stainless steel welds are typically mixture of an austenite matrix and  $\delta$ -ferrite. The amount of  $\delta$ -ferrite varies and has an impact on the mechanical properties of the material. The optimal amount of  $\delta$ -ferrite is between 5 and 10 % of the total amount of the material because lower than 5 %  $\delta$ -ferrite contents can predispose the material to solidification cracking and more than 10% of  $\delta$ -ferrite has a reductive effect on the toughness, ductility and corrosion resistance. Solidification of austenitic stainless steel welds can be primary austenitic or primary ferritic as it appears from figure 13. (Gooch, 1990, p. 32-33; Kou, 2013, p. 216; Lippold & Kotecki, 2005, p. 153.)

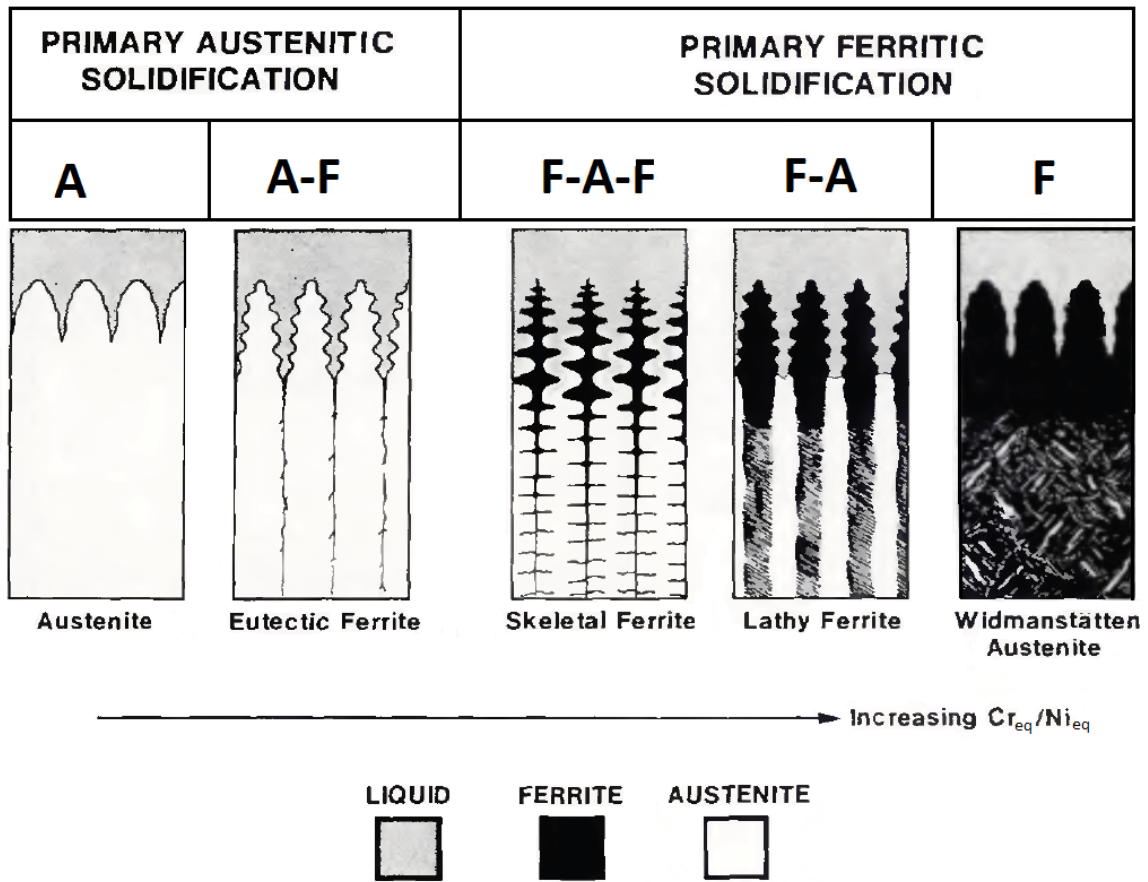


**Figure 13.** Solidification modes of austenitic stainless steels. Fully austenitic solidification (A), primary austenitic solidification with austenite to ferrite formation (A-F), primary ferritic solidification with ferrite to austenite formation and creation of eutectic ferrite (F-A-F), primary ferritic solidification with ferrite to austenite formation (F-A), and fully ferritic solidification (F). (Modified from: Brooks & Thompson & Williams, 1984, p. 72s.)

### 3.5.1 Primary austenitic solidification

Ni-rich alloys prefer austenite as a primary solidification phase. Solidification can result in fully austenitic microstructure (solidification mode A) when low diffusivity of alloying elements and impurities at elevated temperature preserves the segregation profile created by segregation of these elements during solidification. Preservation of the formed segregation profile ensures the clear visibility of austenitic dendrites in the microstructure of the weld metal. (Kou, 2013, p. 218-219; Lancaster, 1999, p. 316-318; Lippold & Kotecki, 2005, p. 154-155.)

Primary austenitic solidification can also result in austenitic-ferritic microstructure (solidification mode A-F) as  $\delta$ -ferrite forms through eutectic reaction along the solidification subgrain boundaries at the end of primary austenitic solidification. The formation of the  $\delta$ -ferrite is caused by the concentration of ferrite-promoting alloying elements (such as chromium and molybdenum) to subgrain boundaries during solidification. Ferrite formed by this mechanism is called interdendritic ferrite, because the  $\delta$ -ferrite forms between the light austenite dendrites and long secondary arms of austenite dendrites. (Kou, 2013, p. 218-219; Lancaster, 1999, p. 316-318; Lippold & Kotecki, 2005, p. 154-155.)

### 3.5.2 Primary ferritic solidification

Ferrite is the dominating phase during the solidification process in primary ferritic solidification. Ferrite ( $\delta$ -ferrite) is the typical primary solidification phase for Cr-rich alloys. Solidification starts as ferrite, and austenite is created between ferrite dendrites through peritectic-eutectic reaction at the end of solidification in ferritic-austenitic solidification (solidification mode F-A). The form of  $\delta$ -ferrite dendrites can be vermicular or lathy depending on  $Cr_{eq}/Ni_{eq}$  and the cooling rate of the weld. Moderate cooling rates and low  $Cr_{eq}/Ni_{eq}$  results ferrite-austenite transformation in the weld metal and vermicular morphology of the ferrite. Austenite consumes the ferrite through diffusion to the point when remaining ferrite is enriched with ferrite-promoting elements and consists only few austenite-promoting elements causing the structure to be stable in lower temperatures. High cooling rates and increased  $Cr_{eq}/Ni_{eq}$  result limited diffusion during the ferrite-austenite transformation creating tightly spaced laths that can be seen in room temperature microstructure as residual pattern of the ferrite cutting across the original growth direction of the dendrites or cells. The amount of  $\delta$ -ferrite in the room temperature microstructure is approximately from 2 to 15 % after ferritic-austenitic solidification (Kyröläinen & Lukkari, 2002, p. 67). Ferritic-austenitic solidification can transform into ferritic-austenitic-ferritic solidification (solidification mode F-A-F) if formation of austenite leads to strong segregation in remaining liquid phase. Strong segregation increases concentration of ferrite promoting alloying elements in remaining liquid phase leading to formation of minor amount of  $\delta$ -ferrite at the end of solidification. (Kou, 2013, p. 219 and 221; Lancaster, 1999, p. 316-318; Lippold & Kotecki, 2005, p. 155-161.)

Solidification of austenitic stainless steel weld metal can also happen as fully ferritic solidification (solidification mode F). Solidification begins and ends as  $\delta$ -ferrite in fully ferritic solidification. Formation austenite in the microstructure happens by diffusion after solidification of ferrite in the solid phase of the metal. High  $Cr_{eq}/Ni_{eq}$  results ferritic microstructure with grain boundary austenite and Widmanstätten austenite plates. Lower  $Cr_{eq}/Ni_{eq}$  results microstructure of acicular ferrite with continuous austenitic network. Fully ferritic solidification is rare in austenitic stainless steels. (Kou, 2013, p. 221; Lancaster, 1999, p. 316-318; Leone & Kerr, 1982, p. 21s; Lippold & Kotecki, 2005, p. 155-161.)

### 3.6 Prediction of weld metal microstructure

Chemical composition of welded material affects the end microstructure of stainless steel weld metal. Prediction of microstructure is based on knowledge of composition of welded materials and filler materials. First diagram for prediction of weld metal microstructure was formed by Schaeffler in 1949. Constitution diagram predicts solid state microstructure based on chromium and nickel equivalents. These equivalents take account the effects of various austenite and ferrite promoting alloying elements in weld metal. Many other constitution diagrams have been formed after Schaeffler-diagram. One of these diagrams is WRC-1992 constitution diagram (figure 14), which predicts solidification mode and amount of ferrite in microstructure. Prediction of weld metal microstructure with assist of WRC-1992 diagram is based on definition of nickel- and chromium-equivalents ( $Ni_{eq}$  and  $Cr_{eq}$ ). These equivalents take account effects of different alloying elements in the metal by grouping them into austenite formers and ferrite formers. Amount of ferrite in weld metal microstructure is presented as ferrite number. WRC-1992 diagram takes account austenite stabilizing property of nitrogen, which may be used as a shielding gas during welding. (Kotecki & Siewert, 1992, p. 171s-172s and 176s; Kyröläinen & Lukkari, 2002, p. 79-81).

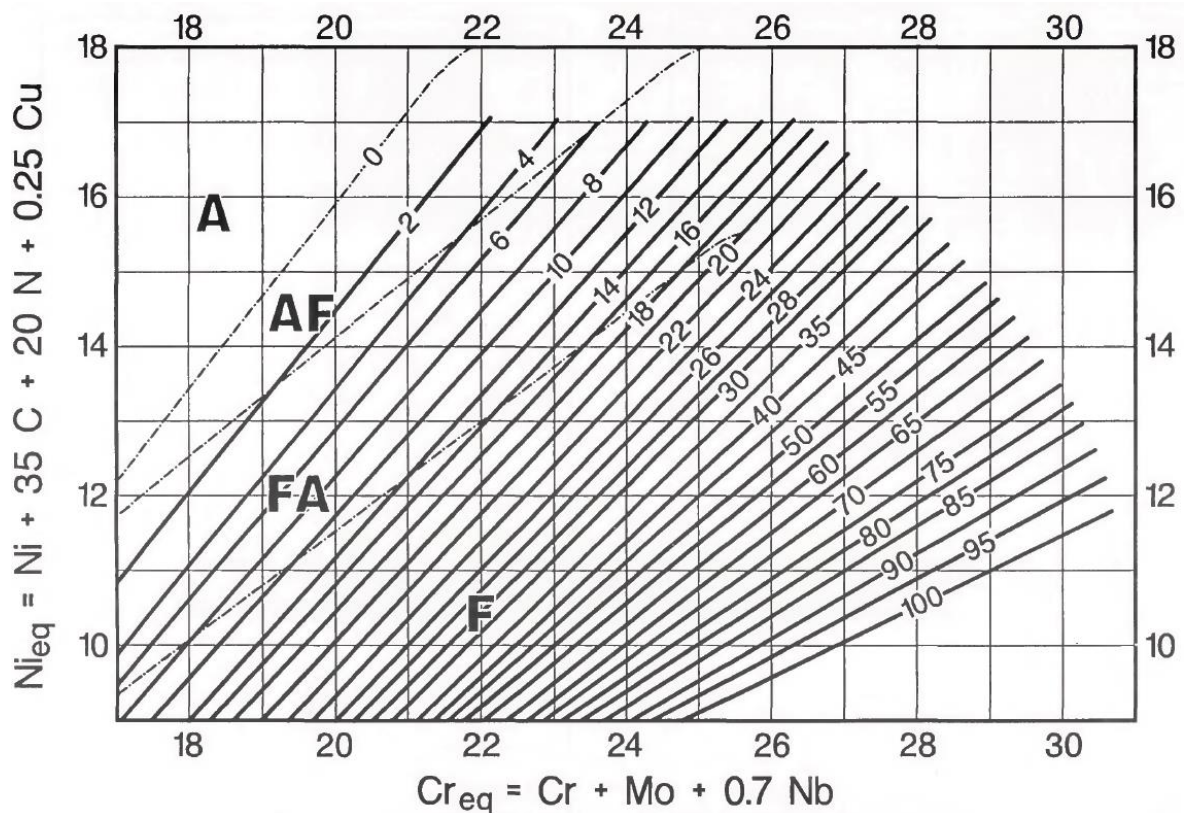


**Figure 14.** WRC-1992 constitution diagram for stainless steel weld metals (Kotecki & Siewert, 1992, p. 176s).

### 3.6.1 Effect of welding parameters on solidification

Welding speed affects the size and shape of the melt pool that shape and size of grains growing from the edges of the weld. Lower heat input limits dendrite growth in fusion zone and produces smaller HAZ, and higher heat input produces coarser grains. Dendritic grain growth becomes more frequent when heat input of the welding is increased. Since cooling and solidification rates may vary in different parts of the weld, it is possible to have multiple solidification modes and morphologies present in the same weld. Cooling rate has been noticed to have an effect on ferrite morphology (Lippold & Savage, 1980, p. 57s). Austenitic stainless steels begin to prefer fully austenitic or fully ferritic solidification under high cooling rates depending on chemical composition of the alloy (David & Vitek & Hebble, 1987, p.229s-300s). Effect of solidification rate on solidification mode in austenitic stainless steels is represented in figure 15. (Arivarasu et al., 2014, p. 901; Elmer et al., 1989, p. 2125-2126; Kumar & Shahi, 2011, p. 3623; Kyröläinen & Lukkari, 2002, p. 61-62; Lippold, 1994, p. 137s-138s; Lippold & Kotecki, 2005, p. 182-184.)

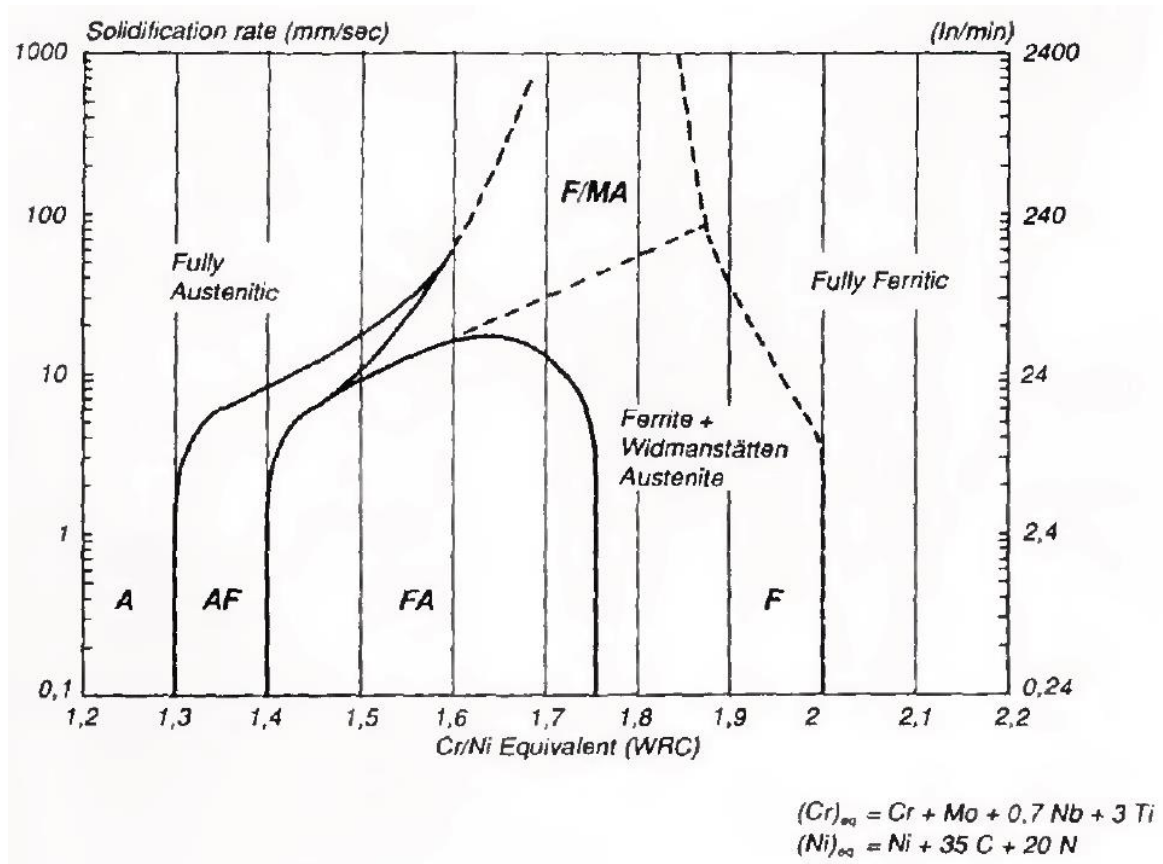


**Figure 15.** Effect of solidification rate and  $Cr_{eq}/Ni_{eq}$  on solidification mode of austenitic stainless steels (Lippold, 1994, p. 138s).

### 3.7 Solidification cracking in austenitic stainless steel welds

Solidification cracking (also known as hot-cracking) occurs during solidification of austenitic stainless steel weld. Concentration of impurities and other substances in the molten material between dendrites subject the weld material to solidification cracking. Impurities concentrate to the centerline of the weld, because of austenite's limited capacity for binding these impurities and direction of weld solidification from the edges of the weld to the centerline of the weld. These impurities and other substances have lower melting temperature comparing to base material. Cooling of the weld material creates stretching forces to the weld material causing the partially molten concentration impurities to rip open along cell boundaries. Chemical composition of welded material (especially sulfur and phosphorus form compounds with melting temperature lower than base material), solidification mode (ferrite prevents solidification cracking), dimensions and shape of the weld together with welding parameters and conditions affect the possibility of

solidification cracking. (Cieslak et al., 1982, p. 7s-8s ; Cooch & Honeycombe, 1980, p. 240s ; Brooks & Thompson & Williams, 1984, p. 76s.)

### 3.8 Effect of welding on alloying elements

Welding does not only have an effect on stainless steel itself, but it also may change chemistry and composition of alloying elements in the welded material. Precipitation of nitrides, carbides and intermetallic compounds takes place during welding. Sensitization by precipitation of chromium carbides on austenite grain boundaries predisposes austenitic stainless steels to intergranular corrosion. Segregation of certain ferrite-promoting alloying elements (Cr, Mo, Si and Ti) creates significant differences in concentrations causing the formation of sigma-phases on austenite grain boundaries. Sigma phases have complex molecular structure, which makes the hard but fragile lowering the ductility of solidified weld metal. Formation of sigma-phase is faster in ferrite due to higher diffusion rates comparing to austenite. Some loss of alloying elements may occur during laser keyhole welding due to vaporization of welded material by high energy density of focused laser beam. (Castro & Cadenet, 1975, p. 126; Kyröläinen & Lukkari, 2002, p. 115-116; Pinnow & Moskowitz, 1970, p. 280; Vitek & David, 1986, p. 109s-110s.)

## **4 MICROSTRUCTURAL CHARACTERISTICS OF COMPONENTS FABRICATED WITH POWDER BED FUSION PROCESS**

It is possible to fabricate components layer by layer with powder bed fusion (PBF) from fine powder (polymers, metals, composites and ceramics) using one or multiple heat sources. Focused laser or electron beam is primary heat source in PBF processes for metallic materials.

### **4.1 Microstructural characteristics of additively manufactured parts**

Connections between individual molten particles in PBF are formed by phenomena called full melting. Connections between closely packed powder particles are formed due to agglomeration and decreasing of surface area driven by minimization of total free energy. High temperatures or long manufacturing times are required in fabrication of high density (no pores) components due to decreasing of total surface area in powder bed caused by this phenomenon. (Gibson, Rosen & Stucker, 2010, p. 106.) Components manufactured with PBF may contain some pores and other structural discontinuities.

#### **4.1.1 Density of components fabricated with PBF**

Decreasing laser power, increasing scan speed or hatch spacing and decreasing layer thickness have been noticed to increase porosity in PBF of metallic materials. Decreasing laser power causes incomplete penetration and poor bonding of molten track to the substrate, and increasing scan speed shortens the laser interaction time leading to inferior melting of the substrate. Some of the process imperfections related with PBF have been noticed to be result from volumetric energy input during the process (Islam et al., 2013, p. 841). Effect of different scan speeds on amount of pores is illustrated in figure 16. (Kamath et al., 2014, p. 75-77; Li et al., 2010, p. 4351-4356; Simchi, 2006, p. 157.)

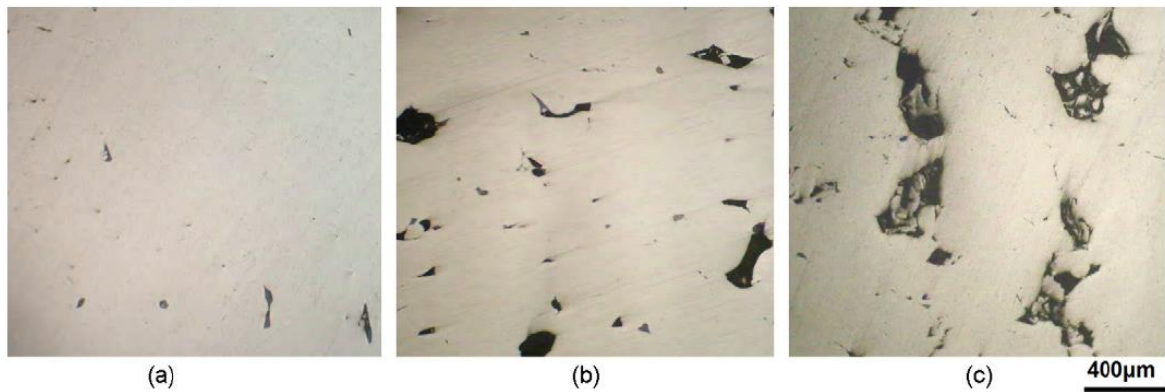


**Figure 16.** Metallographic images of stainless steel 316L manufactured with PBF using constant fiber laser power 190 W, focal point diameter 0.05 mm and hatch spacing 0.15 mm. Scan speed was varied. (a) 100 mm/s, (b) 200 mm/s and (c) 300 mm/s. (Li et al., 2010, p. 4354.)

Increasing hatch spacing makes the distance between individual tracks to grow increasing the probability of emerge of pores. Pores caused by too big hatch spacing have typically regular size and symmetric shape. (Kruth et al., 2010, p. 8.) Hatch spacing also affects surface roughness and uniformity of PBF fabricated surface, as it appears from figure 17. Smooth surfaces are possible to fabricate only by using hatch spacing that is less than average width of the single track. (Yadroitsev & Smurov, 2011, p. 266-268.)

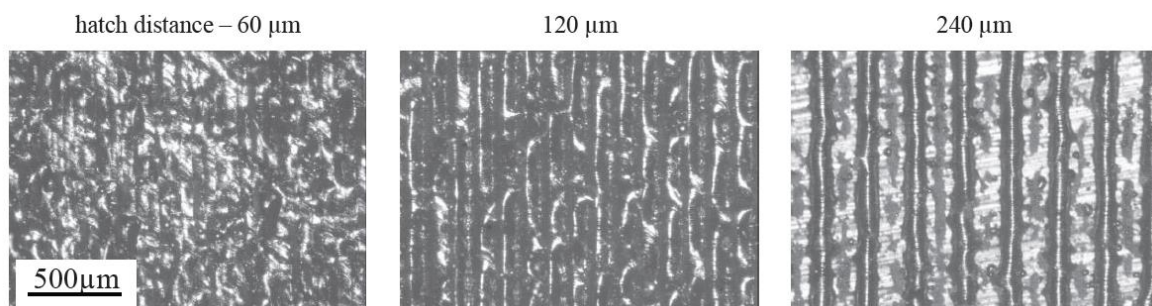


**Figure 17.** Effect of hatch spacing to surface morphology of PBF fabricated component (Yadroitsev & Smurov, 2011, p. 266).

Matilainen et al. (2014) studied process efficiency of PBF and effects of various process parameters to single track formation in PBF. Process efficiency of PBF can be increased by increasing building speed with use of skin-core scanning strategy, where skin and core of the fabricated component are manufactured using different laser powers and layer

thicknesses. Skin of the component is fabricated using lower laser power and thinner layer thickness comparing to the core, which is fabricated using higher laser power and thicker layer thickness. Adaptation of this type of process efficiency improvement requires understanding and control of penetration and width of the single track. Increasing laser energy density or laser beam interaction time was found to increase penetration depth and width-depth area (WDA) of the single track. However width-depth ratio (WDR) of the single track was found to decrease due to increase in laser energy density or laser beam interaction time, as it appears from figure 18. (Matilainen, 2014, p. 322-324; Schleifenbaum et al., 2010, p. 168.)

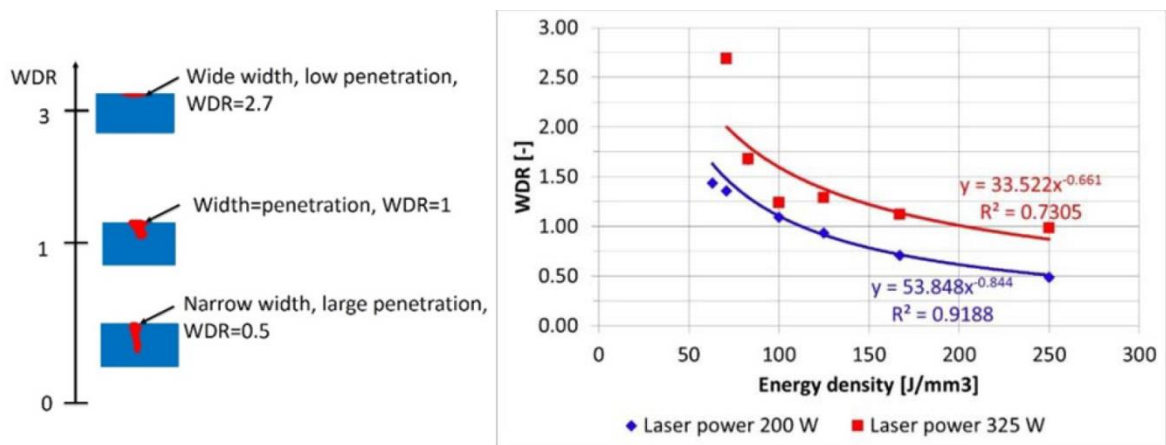


**Figure 18.** Effect of laser energy density to WDR of the single track (modified from: Matilainen, 2014, p. 322 and 324).

Recognition of balling phenomena in case of PBF processes is necessary for fabrication of fully dense parts. Two main types of balling phenomena have occurred during PBF. First driver of emerge of balling is insufficient liquid formation. Liquefied material tries to form droplets due to effect of the surface tension causing inadequate necking. Balling phenomena caused by insufficient liquid formation can be fixed by increasing used laser power and reducing amount of oxygen in atmosphere of the building chamber. Second type of balling phenomena is caused by splashing of small droplets under high scan speeds. Cracking of solidifying liquid track has been noticed to take place simultaneously with emerge of small droplets. Type 2 balling phenomena can be reduced by decrease of scan speed. (Gu & Shen, 2009, p. 2908-2909; Li et al., 2012, p. 1026-1031.)

Behaviors of water atomized powder and gas atomized powder in PBF have been studied. Usage of gas atomized powder in PBF leads to denser structure comparing to usage of water atomized powder. Cooling rates of gas atomized powder result spherical powder particles. Spherical particles have higher packing density comparing to irregularly shaped powder particles produced by rapid cooling rates of water atomization. Higher oxygen content and higher packing density of gas atomized powder ensures higher density of end-product. Usage of preheating of powder bed (over 150 C°) increases density of fabricated parts (Zhang & Dembinski & Coddet, 2013, p. 27-28). However, the effect of preheated powder bed decreases when distance between the building platform and build layer increases. Chemical composition of the material, average powder particle size and particle distribution affect the densification kinetics during PBF process (Simchi, 2006, p. 157). Also thickness of the layer spread by the coater affects the relative density of the fabricated parts as it appears from figure 19. (Kruth et al., 2010, p. 2; Li et al., 2010, p. 4356; Zhang, Dembinski & Coddet, 2013, p. 30.)

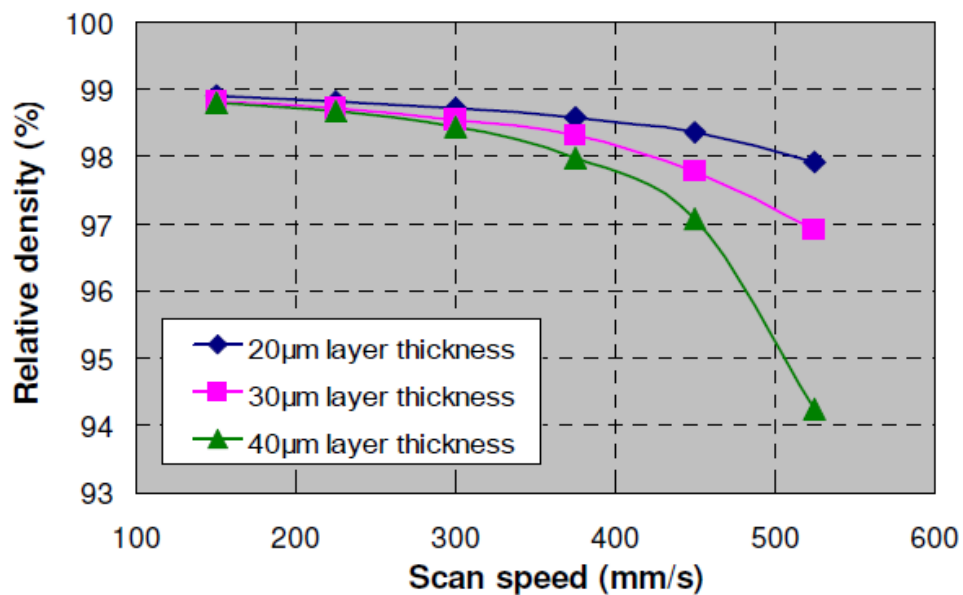


**Figure 19.** Effect of scan speed and layer thickness on relative density of Stainless Steel 316L (Kruth et al., 2010, p. 2).

#### 4.1.2 Microstructure of austenitic stainless steel parts fabricated with PBF

PBF process of austenitic stainless steel has similar behavior as phenomena occurring during laser welding but scale is much smaller: Cooling rates of melted material during are

high fabrication process due to fast scan speeds and high energy density. According to simulations in the study of Van Belle, Vansteenkiste & Boyer (2012, p. 1070), cooling rates in PBF may be even 5000 °C/s, which are similar to weld metal cooling rates (from 1000 to 10000 °C/s) in laser welding (Kujanpää, 2014, p. 631). High cooling rates cause fast solidification of melted material leading to appearance of fully austenitic solidification mode and fine grain structure. Also cellular-dendritic structure can be observed from room temperature microstructure of PBF fabricated stainless steel 316L. As it appears from figure 20, the end microstructure of stainless steel 316L component fabricated with PBF has a fully austenitic microstructure with average cell size of 5 µm and 10 µm. It is characteristic for PBF fabricated component to have layered structure in the build direction, and singular tracks can be observed from the microstructure. Heat leaves the individual track by conducting through the substrate and cumulates easily to the top part of the component causing variations in cooling rate. Heat leaves the manufactured component mainly by conduction through building platform due to low heat conductivity of the atomized powder (Islam et al., 2013, p. 840). Grain size has been noticed to be finer at the bottom of PBF fabricated component comparing to top. (Gu et al., 2012, p. 155-156; Kruth et al., 2010, p. 7-8; Riemer et al., 2014, p. 21-22; Zhang et al., 2013, p. 25-26.)

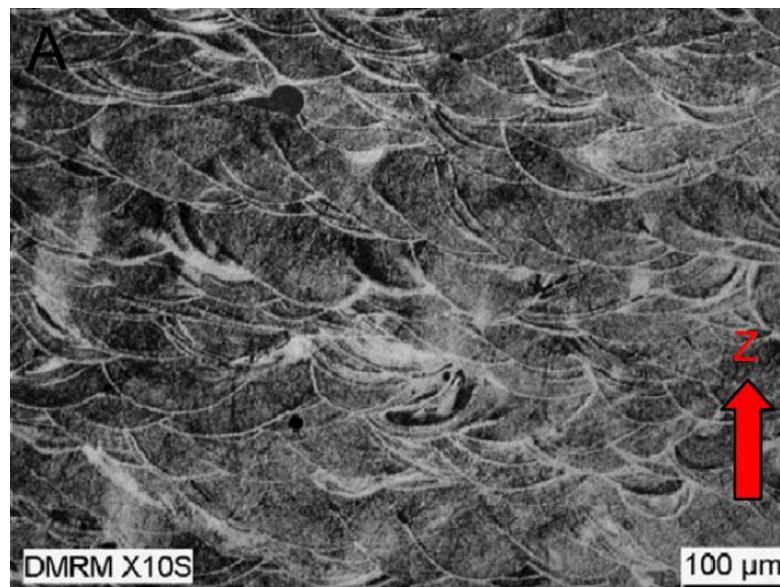


**Figure 20.** Microstructure of the cross-section of stainless steel 316L powder processed with PBF (Nd:YAG laser source). Used laser power was 100 W and scan speed 300 mm/min. Build direction marked as z. (modified from: Zhang et al., 2013, p. 26.)

#### 4.2 Mechanical properties of components manufactured with PBF

Tensile properties of stainless steel 316L components fabricated with PBF has been studied by Yadroitsev et al. (2009) and Zhang et al. (2013). Yadroitsev et al. (2009) studied tensile properties of stainless steel 316L fabricated with PBF. Mechanical properties of PBF components depend on relative density of the component and chemical composition of the material. Uneven spreading of powder and pores caused by inappropriate process parameters was detected to have decreasing effect on the tensile strength of PBF components. Zhang et al. (2013) detected that tensile strength and elongation of stainless steel 316L component fabricated with PBF can be increased by preheating of building platform, as it appears from figure 21. Tensile properties of these parts are different depending on building direction. Ultimate tensile strength of the 316L PBF components were similar (between 500 and 600 MPa) in both of the studies. Elongation was relatively short (10-20 %) comparing to cold rolled sheet metal (40%). (Yadroitsev et al., 2009, p. 4-5; Zhang et al., 2013, p. 28.)

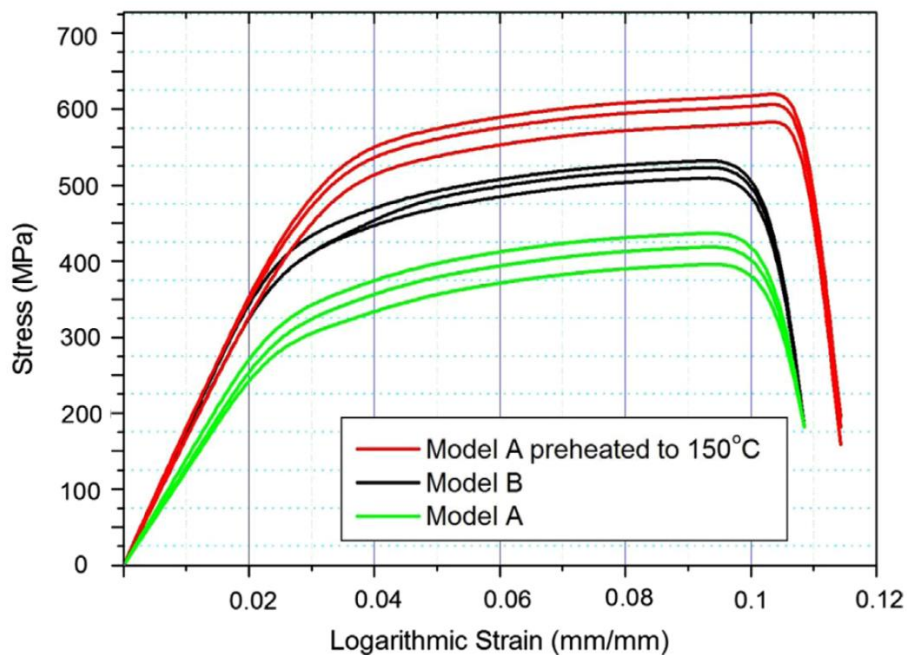


**Figure 21.** Tensile properties and effect of preheated building platform on tensile strength of PBF component. Model A: Test piece placed perpendicularly against the building direction. Model B: Test piece placed parallel to the building direction. (Zhang et al., 2013, p. 28.)

Riemer et al. (2014) studied fracturing behavior and effect of heat treatment on mechanical properties stainless steel 316L components fabricated with PBF. Ultimate tensile strengths and elongations at break in the study of Riemer et al. (2014) were in the same range comparing to the studies of Yadroitsev et al. (2009) and Zang et al. (2013). Stress relieving heat treatment was noticed to not to have significant effect on monotonic properties of PBF fabricated 316L components, and fatigue behaviour in the high cycle fatigue (HCF) regime and crack growth were similar in the heat treated components comparing to components that were not heat treated. Therefore imperfections caused by PBF process have only negligible effect on ductility and fatigue behaviour of PBF fabricated 316L components. Cracking of PBF fabricated component during HCF testing occurred along closely spaced grain boundaries (figure 22). Path of the cracking depends on building direction of the PBF fabricated components. Grain boundaries form crack arresting barriers causing tortuous crack path when cracking happens perpendicularly against the building direction. Crack growth parallel to build direction is more direct comparing to crack growth perpendicularly against the building direction. (Riemer et al., 2014, p. 18-23.)

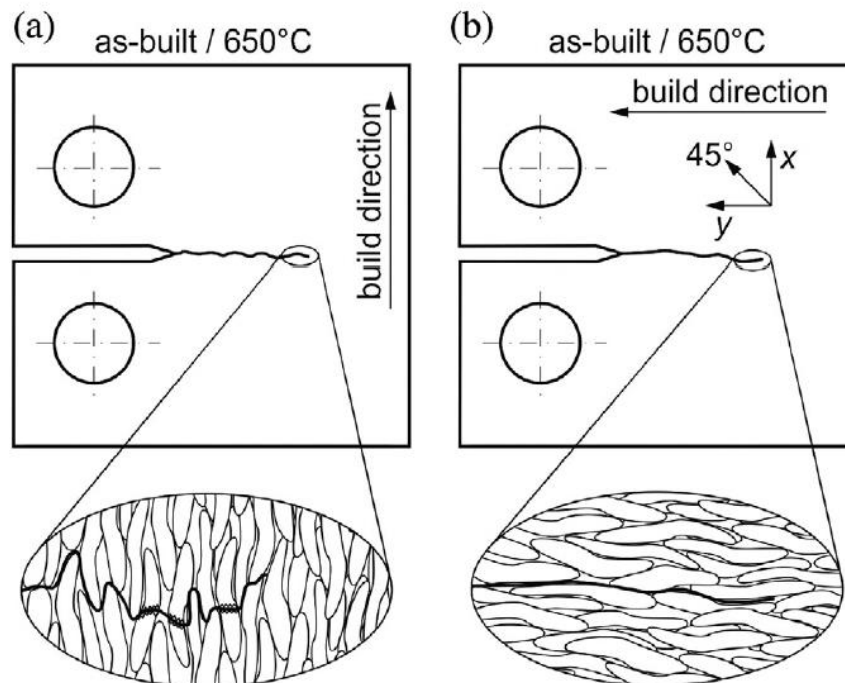


**Figure 22.** Path of the crack growth in PBF fabricated components: a) perpendicularly against the building direction, and b) parallel to the building direction. (modified from: Riemer et al., 2014, p. 23.)

Fine substructures present in the microstructure of PBF fabricated component were suspected to be the cause behind higher yield strengths (approximately 440-465 MPa) and elongations at break (48-53 %) comparing to conventionally manufactured components of the same composition (yield strength 220 MPa and elongation at break 40 % or more). Elongations at break differ from the values in the studies of Yadroitsev et al. (2009) and Zang et al. (2013). (Riemer et al., 2014, p. 18-19.)

#### 4.3 Welding of PBF fabricated components

There are only few studies about weldability of PBF fabricated components. Weldability of PBF fabricated stainless steel 316L sheets to wrought material of same composition was studied by Casalino et al. (2013). Test pieces were welded using laser-TIG hybrid welding, and tensile test we executed for defect free and full penetration samples. Tensile tests showed that tested welds had higher tensile strength and low elongation comparing to similar welds in wrought material of same composition (figure 23). Fracturing of welded test pieces happened on the side fabricated with PBF. Suspected reason for fracturing behavior was higher microhardness of PBF fabricated sheet. (Casalino et al., 2013, p. 210-216.)

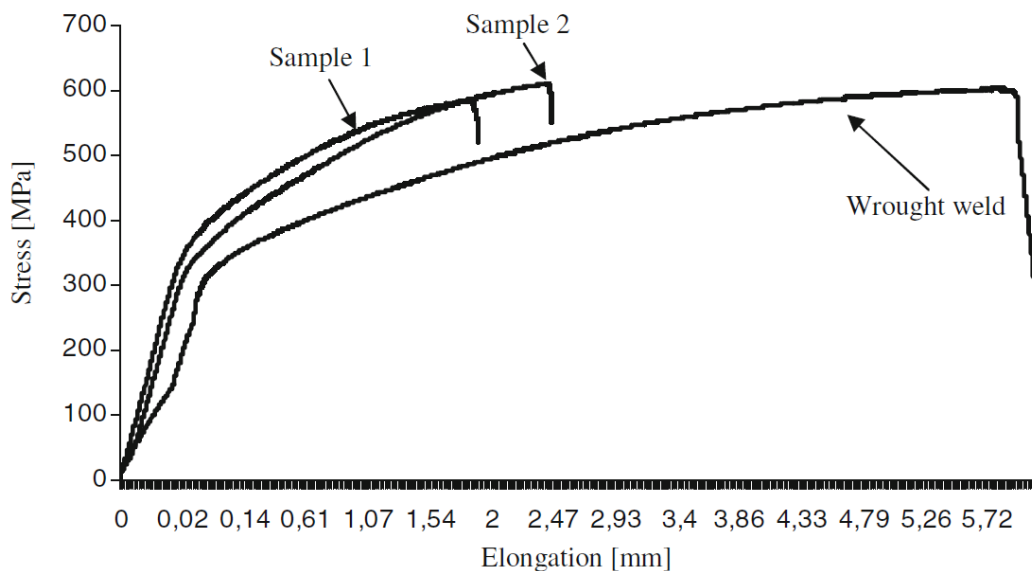


**Figure 23.** Tensile test results of welds between PBF fabricated sheets (sample 1 and sample 2) and wrought metal. (Casalino et al., 2013, p. 214).

Effect of build orientation on tensile strengths of welded PBF fabricated sheets was studied by Järvinen (2014). Test pieces were welded using TIG welding process, and tensile tests, bend tests and weld hardness tests were executed for welded specimens. Results of the tensile test are similar to results of Casalino et al. (2013). Welded PBF fabricated sheets appear to have higher tensile strength and lower elongation comparing to welded wrought metal of same composition. PBF fabricated components welded in the build direction have higher tensile strength comparing to components welded perpendicularly against the build direction. This is called weld-build orientation. Effect of weld-build orientation on tensile strength and elongation can be seen in figure 24. Fracturing of most of welded test pieces happened next to fusion zone, and two of the specimens broke from fusion zone. (Järvinen, 2014, p. 53-56.)

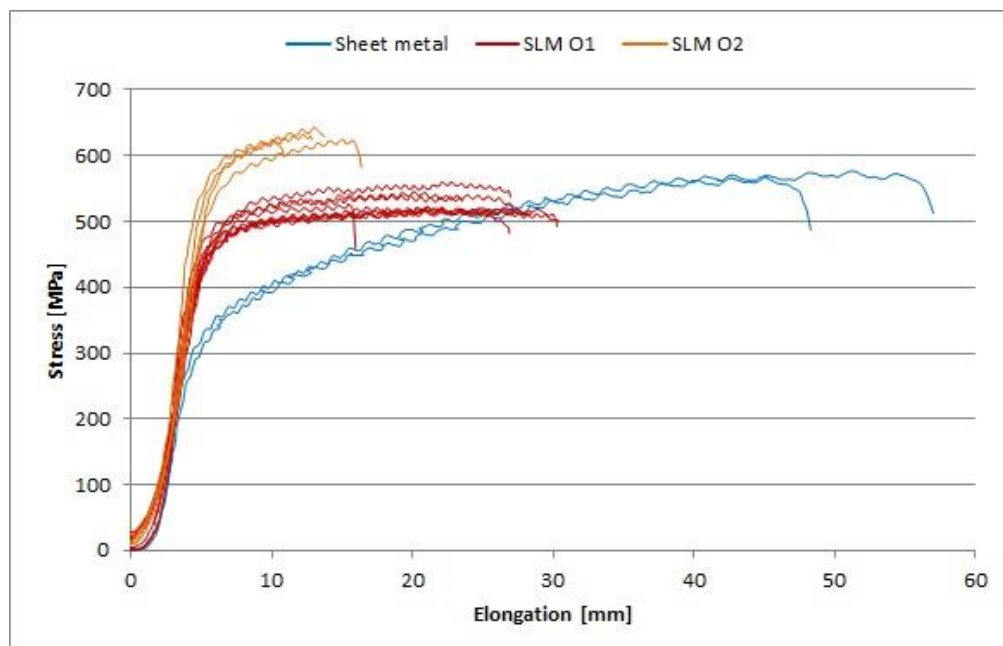


**Figure 24.** Tensile test results of welds between PBF fabricated sheets. PBF sheets are marked as ‘SLM’ after commercial PBF-process called Selective Laser Melting. O1: Weld oriented perpendicularly against build direction. O2: Weld oriented to the build direction. (Järvinen, 2014, p. 54.)

PBF fabricated side of the welds showed cellular solidification and ferrite precipitation at the grain boundaries. Multioriented growth of columnar grains and dendrites is visible in fusion zone microstructure of the PBF fabricated side of the weld, as it appears from figure

25. Casalino et al. (2013) proposed that random grain orientation resulted from small grain size and precipitation of alloying elements to grain boundaries during PBF process. Fusion zone on the side of wrought metal had larger grains oriented regularly towards centerline. (Casalino et al., 2013, p. 214).

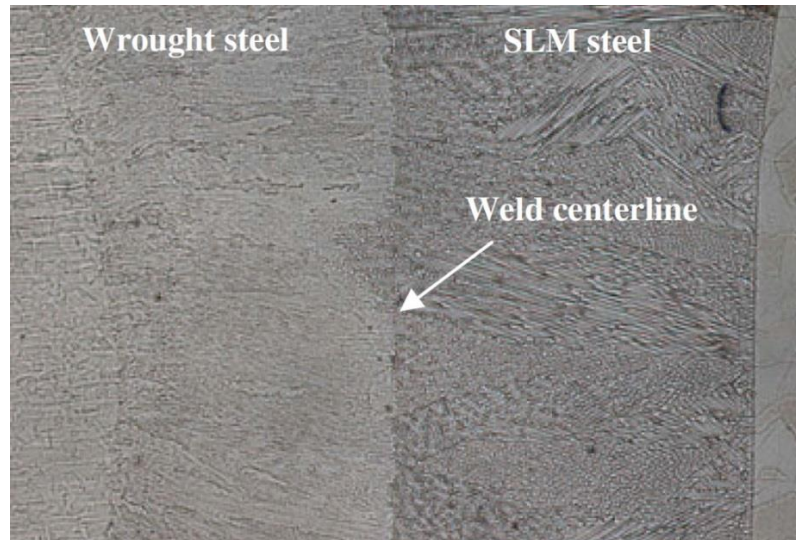


**Figure 25.** Weld microstructure showing sharp fusion boundary between fusion zone and PBF base material. PBF side of the weld is marked as ‘SLM steel’. Columnar grain growth and random grain orientation. (Casalino et al., 2013, p. 213).

## 5 EXPERIMENTAL SETUPS AND EXPERIMENTAL PROCEDURE

Weldability of stainless steel 316L PBF sheets to cold rolled sheet metal of same composition and the effect of energy input on the microstructure of the welds was studied in the experimental part of this study. The welding was carried out using laser keyhole welding, and laser power, diameter of the optical fiber and welding speed were varied. Mechanical properties of the welds were studied using tensile testing and bend testing. Dimensions of the cold rolled sheet metal pieces were identical comparing to the additively manufactured test pieces. Weaker weld-build orientation was selected based on the study of Järvinen (2014). Dimensions of the singular test pieces and build direction of the additively manufactured piece comparing to the weld are illustrated in figure 26.

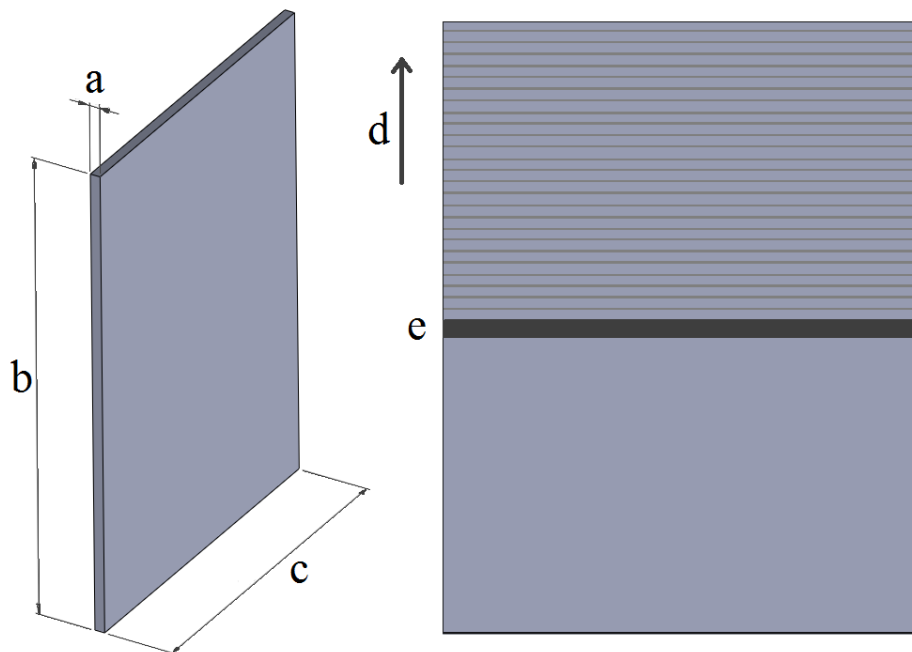


**Figure 26.** Dimensions and orientation of the additively manufactured test pieces. a) Thickness 3 mm, b) length 139 mm, c) width 100 mm, d) build direction of the additively manufactured test piece, and e) weld.

### 5.1 Materials used in the study

Two different types of stainless steel 316L was used in the study. PBF sheets were manufactured from EOS 316L powder. Chemical composition of EOS 316L powder is presented in the table 2.

*Table 2. Chemical composition of EOS 316L powder.*

Alloying element	Cr	Ni	Mo	Mn	Si	Cu	C	P	S	N
Max	19.00	15.00	3.00	2.00	0.75	0.50	0.030	0.025	0.010	0.10
Min	17.00	13.00	2.25	-	-	-	-	-	-	-

Used cold rolled sheet metal was Outokumpu 316L. Chemical composition of Outokumpu 316L is presented in the table 3. Gold rolled test pieces were cut to the right dimensions using laser cutting unit of the punching machine in the laboratory of laser materials processing of Lappeenranta University of Technology.

*Table 3. Chemical composition of Outokumpu 316L cold rolled sheet metal.*

Alloying element	Cr	Ni	Mo	Mn	Si	Cu	C	P	S	N
Max	18.00	14.00	3.00	2.00	0.75	-	0.030	0.045	0.030	0.10
Min	16.00	10.00	2.00	-	-	-	-	-	-	-

### 5.2 Fabrication of PBF sheets

PBF sheets were fabricated using EOSINT M 280 system of Electro Optical Systems Finland Oy in Turku. M 280 has a 400 W Yb-fiber laser, integrated nitrogen generator and high speed scanner (up to 7.0 m/s scan speeds). Focus diameter can be varied between 100  $\mu\text{m}$  and 500  $\mu\text{m}$ . Building volume of the machine is 250 mm x 250 mm x 325 mm. M 280 fabricates parts using Direct Metal Laser Sintering (DMLS) process, which is a trademarked name of the PBF process used by Electro Optical Systems. Used EOSINT M 280 machine is presented in figure 27.

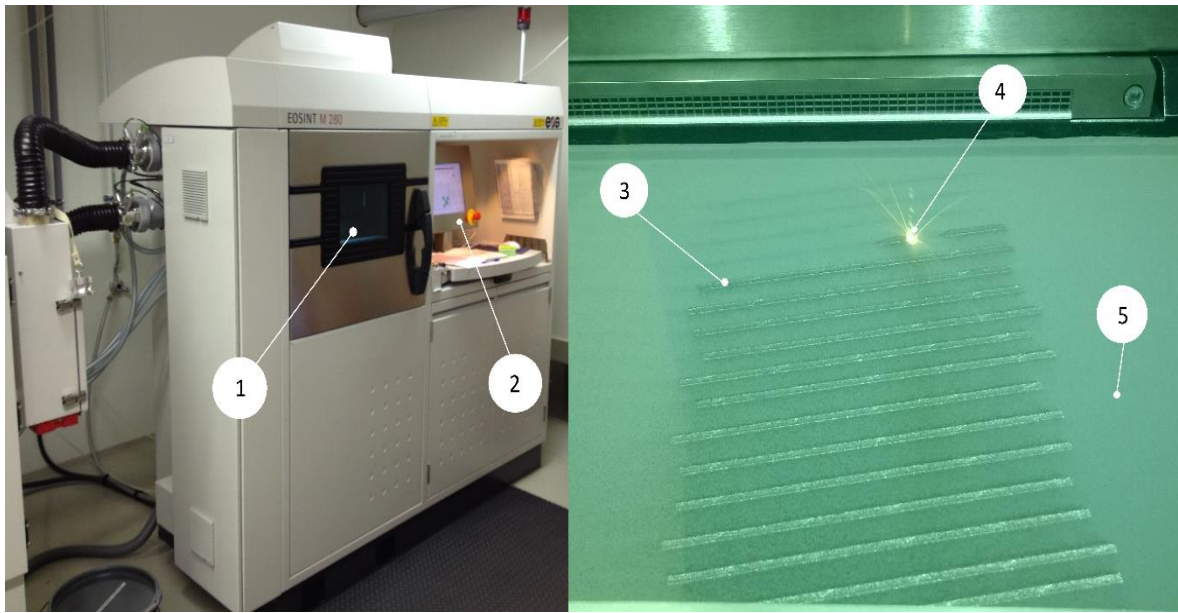


**Figure 27.** EOSINT M 280. 1) Building chamber, 2) control unit, 3) manufactured work piece, 4) laser beam interacting with powder, and 5) powder bed.

Fabrication of PBF sheets was executed in two patches. Each of the patches contained 18 work pieces. Fabricated sheets were positioned on building platform so that the risk of recoater colliding to work pieces during fabrication was minimal. Atmosphere of the building chamber consisted of nitrogen during fabrication. Parameters used in the fabrication of PBF sheets were set to be confidential by EOS Finland.

Heat cycle during the fabrication process causes stresses into fabricated pieces and building platform leading to visible bending of the building platform after extraction from PBF machine. Both of the fabricated patches were heat treated for stress relieving before sawing off the building platforms. Graph of the executed heat treating is presented in appendix I. Both of the fabricated patches were heat treated the same way. Bending of the building platform disrupts the removal of fabricated sheets by obstructing the access of saw to base of the fabricated sheets. Possible bending of the building platforms was taken into account during selection of the used dimensions. Second of the fabricated batches is presented in figure 28.

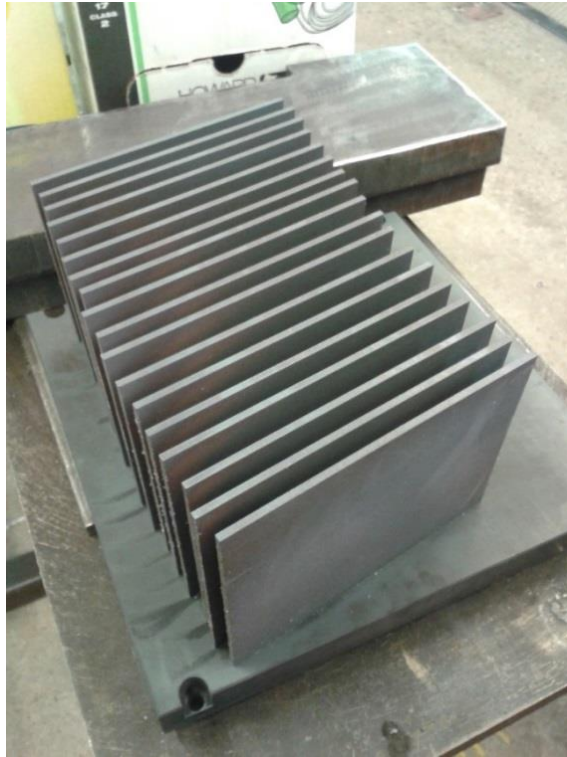


**Figure 28.** Batch of 18 fabricated PBF sheets.

### 5.3 Laser welding of test pieces

Laser welding experiments were executed in laboratory of laser materials processing of Lappeenranta University of Technology. Used laser was IPG YLS-10000-S4 fiber laser (Maximum laser power 10 kW) with 120 mm Kugler collimator. Focal length was 300 mm. Optical fibers of 300  $\mu\text{m}$  and 600  $\mu\text{m}$  were used in the experiments. Shielding gas pipe (diameter 12 mm) was set in 45° angle against work piece surface and behind laser beam in the direction of the welding. Used laser welding equipment is presented in figure 29.

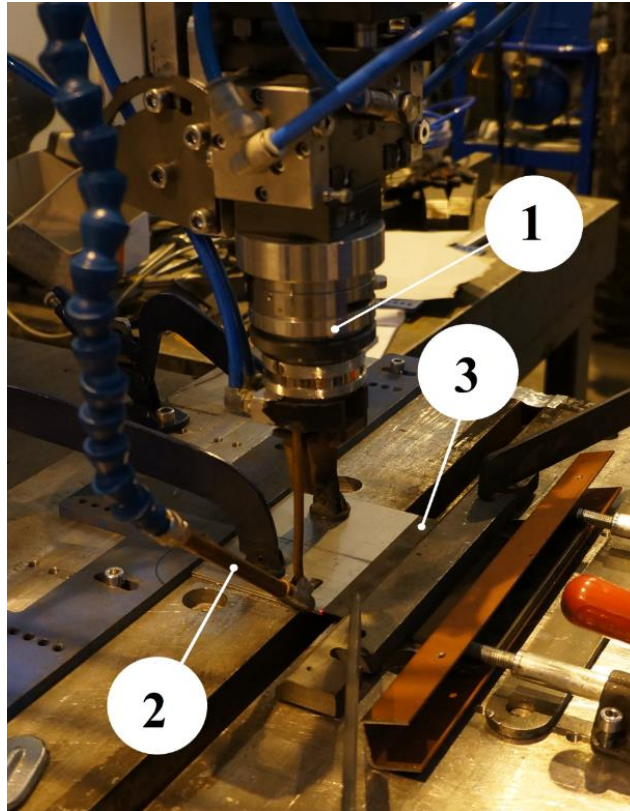


**Figure 29.** Laser equipment. 1) Kugler 120 mm collimator, 2) shielding gas pipe, and 3) work pieces.

### 5.3.1 Laser welding parameters

Focal point position was on the top surface of work piece during all laser welding experiments. Argon was used as a shielding gas, and it was brought to the weld pool 15 l/min. Used welding position was PA, and weld type was butt weld with I groove. Weld grooves were milled and cleaned with acetone. Laser welding experiments were executed in room temperature (measured 23 °C), and test pieces were not preheated. Varied laser welding parameters were optical fiber diameter, laser power and welding speed (appendix II). One test piece (cold rolled sheet metal to cold rolled sheet metal) was welded for comparison of values in pendulum impact tests. Used welding parameters for comparison sheet were: 300  $\mu\text{m}$  optical fiber, 4.5 kW laser power and 3000 mm/min welding speed. Energy input was used instead of heat input due to difficult determination of laser beam absorption for the welded material. Energy inputs were calculated using equation 1.

#### 5.4 Destructive testing and microscopic examination

Preparation of test pieces for destructive testing and microscopic examination was executed in laboratory of welding and laboratory of production technology of Lappeenranta University of Technology. Welded test pieces were cut to pieces for destructive testing and microstructural analysis using band saw. Tensile test pieces and pendulum impact pieces were milled to correct dimensions. Dimensions of the welded test pieces were designed so that one tensile test piece, one bend test piece and one micrographic section could be obtained from a single welded test piece. Figure 30 presents the location of samples in welded test piece.

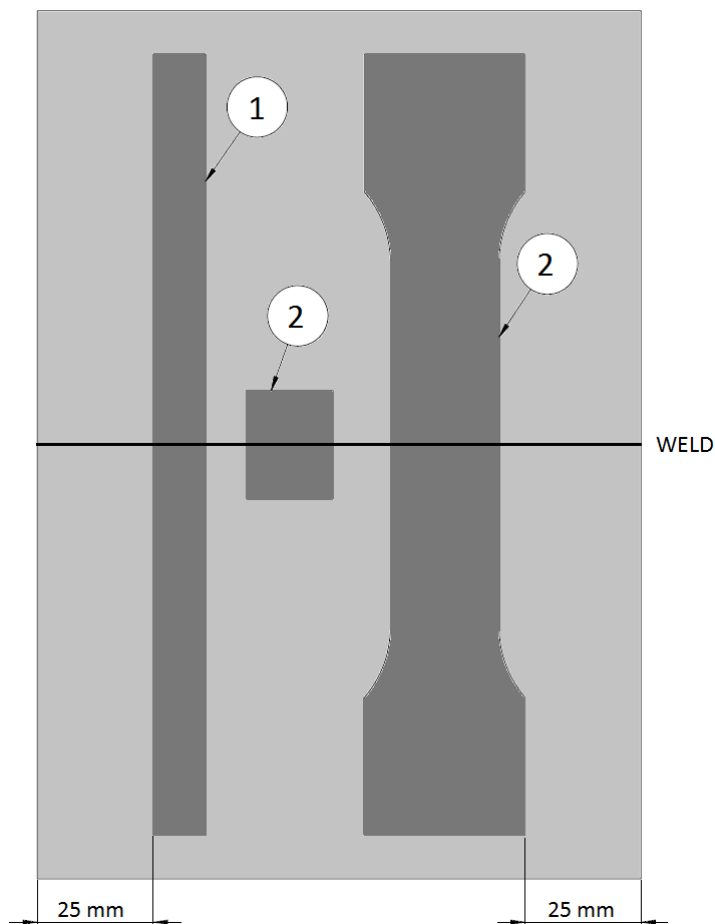


**Figure 30.** Samples obtained from a single work piece. 1) Bend test piece, 2) micrographic section, and 3) tensile test piece.

##### 5.4.1 Tensile and bend test pieces and equipment

Tensile and bend test were executed according to specifications of standards ISO 4136 and ISO 5173 + A1. Dimensions of tensile test pieces and bend test pieces are presented in

tables 4 and 5. Some variation was observed in the lengths and widths of the test pieces after sawing. Tensile test pieces were milled to correct dimensions so, that important dimensions (parallel length and width of parallel length) were accurate. Some variation was allowed in the width of the bend test pieces since it does not have a significant effect on the result of the experiment. Every parameter set pair had one face side (FBB) and one root side (RBB) bend test specimen. Surfaces on the side of the pressing tool were milled smooth.

*Table 4. Dimensions of the tensile test pieces (according to SFS-EN ISO 4136).*

Dimension	Value
Length of the test specimen	180 mm
Thickness of the specimen	3 mm
Width of the shoulder	37 mm
Parallel length	84 mm
Width of the parallel length	25 mm
Radius at the shoulder	25 mm

*Table 5. Dimensions of the bend test pieces (according to SFS-EN ISO 5173 + A1).*

Dimension	Value
Length of the test specimen	180 mm
Thickness of the specimen	3 mm
Width of the specimen	12 mm

Both tensile test and bend test were executed using the same machine (figure 31) in the laboratory of heat treating of Lappeenranta University of Technology. Sections for tensile testing and bend testing are located on each other in the machine. Tensile testing section of the machine measures stretching force and displacement of the stretching tool. Computer attached to tensile testing machine plots the measured values in excel file every 0.1 second. Measurements of elongations at break based on determination of initial gauge lengths and final lengths of the specimens after breaking. Used bend testing pressing tool radius was 10 mm. Destructive test were executed in room temperature. Gap between supporting rollers was 19 mm.

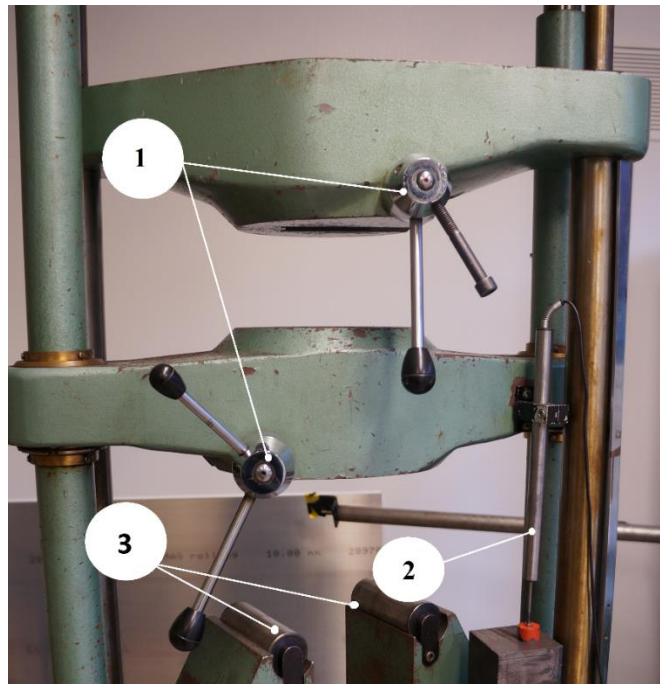


**Figure 31.** Machine used for tensile testing and bend testing. 1) Locking tools for tensile test piece, 2) displacement sensor, and 3) supporting rollers for bend testing.

#### 5.4.2 Microscopic examination

Microscopic examination of welds was executed in the Laboratory of Metallurgy of Lappeenranta University of Technology. Size of the sawed micrographic sections was 3 x 20 x 25 mm. Specimens were smoothed before sanding due to rough surface quality after sawing. Preparation of the specimens for etching was executed using Struers Tegra. Six specimens could be prepared simultaneously in revolver of the machine. Specimens were first rough sanded for two minutes following one minute of fine sanding. Sanded surfaces were washed with water between rough and fine sanding and after sanding processes. Surfaces of the specimens were polished for five minutes in the same machine. Polished surfaces were washed with water and ethanol before drying. Specimens were etched using oxalic acid (10 %, mixed with water) and electric current (voltage 20 V, current 2 A) for 45 seconds before washing the etched surfaces with ethanol. Microscopic pictures of the specimens were taken using Olympus PME microscope. Struers Tegra and Olympus PME are presented in figure 32.

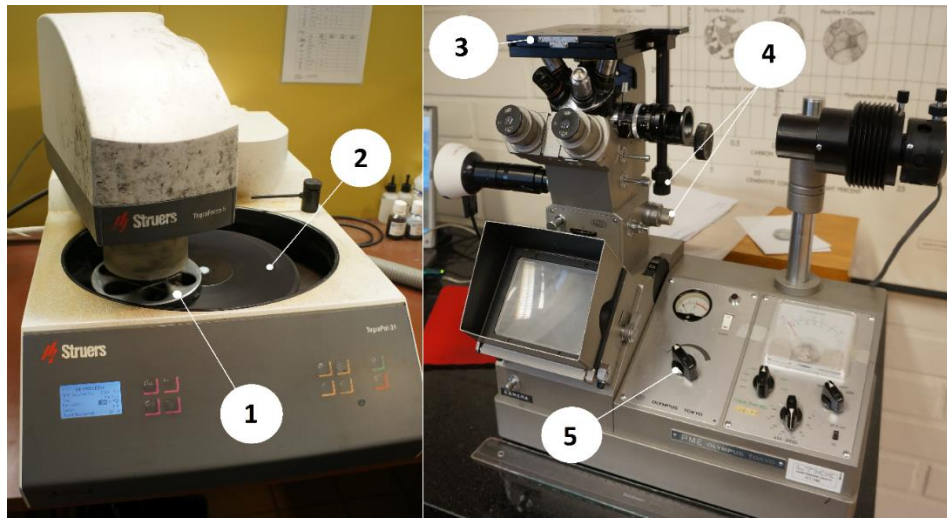


**Figure 32.** Struers Tegra and Olympus PME. 1) Rotating revolver for preparation of specimens, 2) sand paper on a rotating platform, 3) platform for micrographic specimens, 4) adjustment buttons for focusing and accurate placement of analyzed specimen, and 5) adjustment for lighting.

Ferrite measurements were executed using Feritscope MP3 in the Laboratory of Metallurgy of Lappeenranta University of Technology. Measurements of ferrite content of the weld metals using this device base on magnetic induction. Ferrite is magnetic, and therefore detectable among non-magnetic austenite. Ferrite contents were measured using automatic function of Feritscope MP3, which calculates average value of ten measurements. Ferrite measurements were also executed for cold rolled sheets metal and PBF fabricated sheets.

SEM analysis of the specimens was executed in the Laboratory of Chemistry of Lappeenranta University of Technology. Energy-Dispersive Analysis (EDA) was used in the experiments. A line was drawn across the examined specimen, and program of the SEM machine selected ten points inside the line where the measurements were executed. Measurements were gathered together to form concentration profile of the scanned line. Segregation of the alloying elements can be studied based on the information gained from the profile. Results were used for supporting the analysis of the solidification modes in the welds.

## 6 RESULTS AND DISCUSSION

Overall quality of the welds produced in this study is high. Any weld defects were not found during visual inspection or post processing. It was noted that the welds produced using 600  $\mu\text{m}$  optical fiber diameter were significantly wider comparing to welds produced using 300  $\mu\text{m}$  optical fiber diameter. Wight of the welds was detected to grow as a result of growth of energy input, as it appears from figure 33. Weld surface quality of the welds produced using 1000 mm/min welding speed was rougher comparing to welds produced with higher welding speed. This was presumed to be caused by changes in keyhole behavior and increase of energy input due to decrease of welding speed. Some spattering was detected with 2000 mm/min welding speed when using 300  $\mu\text{m}$  optical fiber diameter. Colorization of the base metal increases due to increase in energy input.

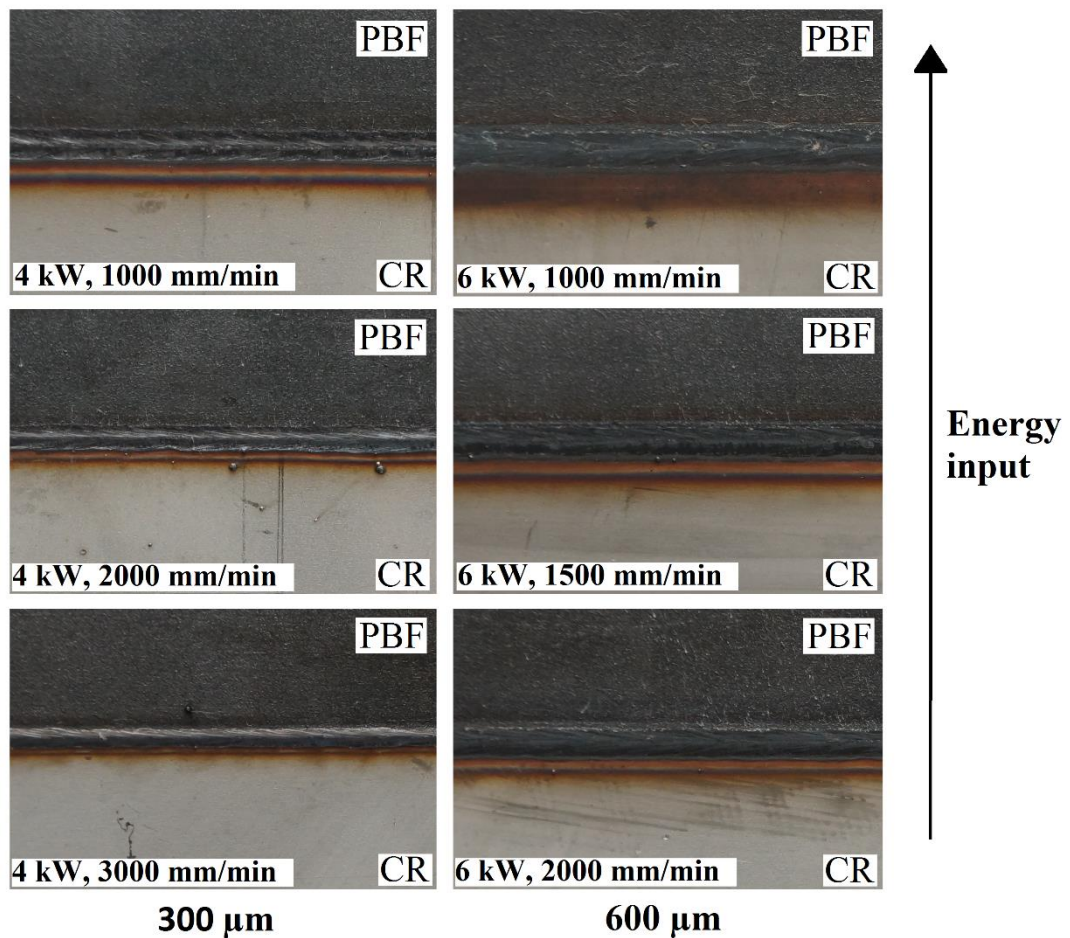


**Figure 33.** Effect of energy input of the welding on shape and size of the weld surfaces with used optical fibers.

Growth of width of the welds due to increase in energy input is also visible in macrographs of the welds (presented in figure 34). Weld centerline and fusion boundaries are sharp and clearly visible in every weld. Formation of slight shape imperfections on top and bottom surfaces of the welds are visible in all welds produced using 300  $\mu\text{m}$  optical fiber diameter and welding speed of 1000 mm/min or 2000 mm/min. More weld macrographs are presented in appendix III.

Shape of the welds produced using 600  $\mu\text{m}$  optical fiber diameter is relatively constant comparing to shapes of the welds produced using 300  $\mu\text{m}$  optical fiber diameter. Neck shaped form of the fusion boundary is visible on the side of the cold rolled sheet metal in every weld produced using 300  $\mu\text{m}$  optical fiber diameter. Size of the neck appears to grow when welding speed is being increased (decrease in energy input). Shape of the fusion boundary on the side of the PBF sheet is fairly straight in every weld comparing to fusion boundary on the cold rolled side of the weld.

Differences in the shapes of the fusion zone boundaries could be result from differences in melt pool behavior between CR and PBF side of the welds. PBF fabricated sheets were suspected (based on the visual analysis of the welding) to have initially lower molten pool viscosity comparing to cold rolled sheet metal in the study of Järvinen (2014). These differences in weld pool viscosities and material flows in molten weld pool might have resulted from slight differences in chemical compositions of the welded materials, material differences caused by segregation during PBF process or differences in heat conductivities of PBF and CR base materials.

Flows of the molten metal during laser welding depend on chemical compositions of the welded materials and process parameters such as laser power and welding speed. Laser power might affect the behaviour of the melt pool by increasing energy input and creation of heat in the weld pool. Increasing energy increases cooling time and volume of molten material, which might explain differences in formation of the neck between 300  $\mu\text{m}$  and 600  $\mu\text{m}$  optical fibers. 300  $\mu\text{m}$  optical fiber produces narrower weld comparing to 600  $\mu\text{m}$  optical fiber, which makes small differences in weld shape clearly visible. Welding speed affects flow rates inside of the molten weld pool, and combined with the effect of the decreasing energy input explains growth of the neck when welding speed is being raised.

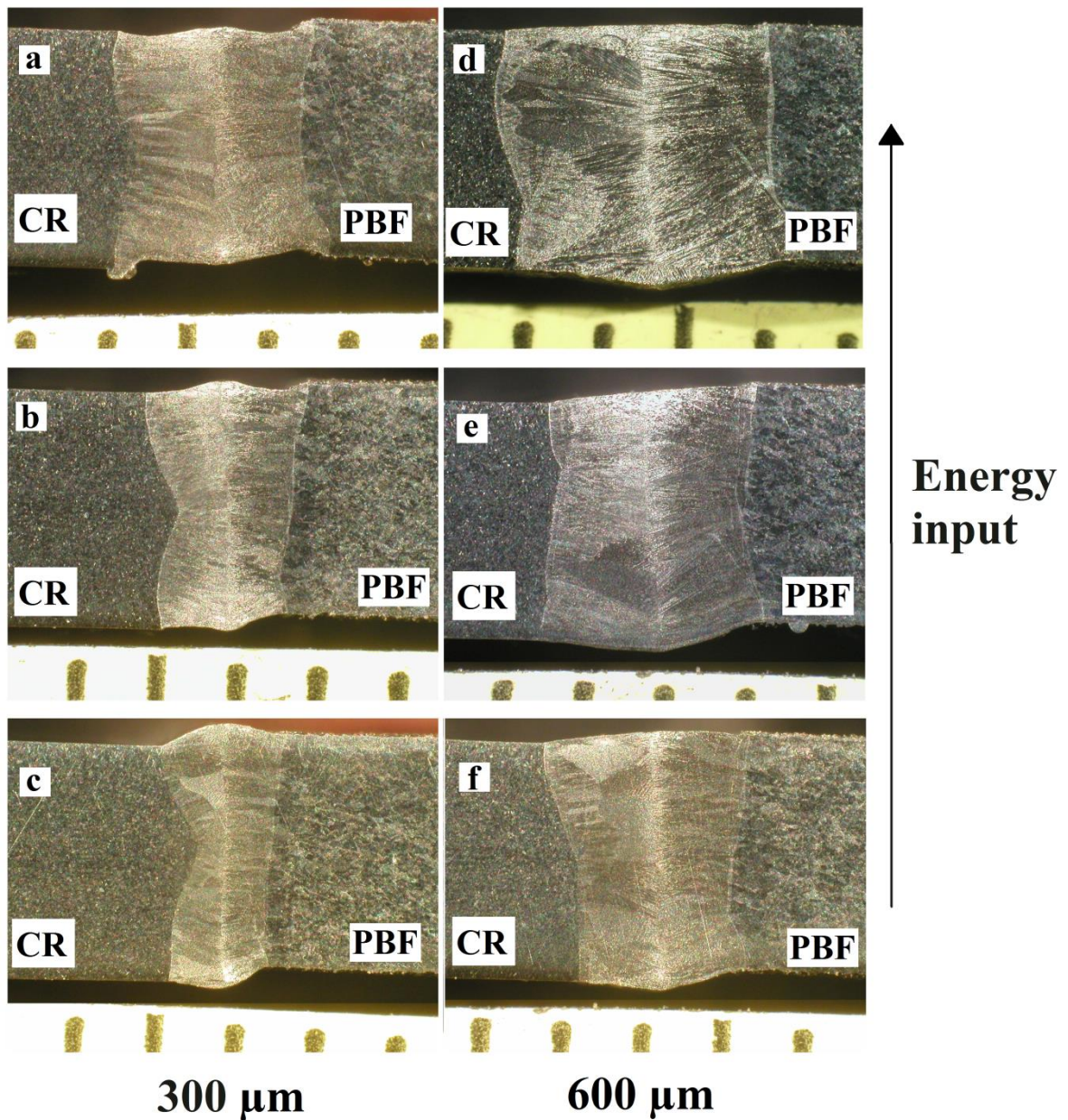


**Figure 34.** Effect of energy input on shape and size of the weld metal and fusion boundaries with used optical fibers. Welds produced using 300  $\mu\text{m}$  optical fiber diameter were welded using 4 kW laser power (a) 1000 mm/min, b) 2000 mm/min, and c) 3000 mm/min), and welds produced using 600  $\mu\text{m}$  optical fiber diameter were welded using 6 kW laser power (d) 1000 mm/min, e) 1500 mm/min, and f) 2000 mm/min).

### 6.1 Microstructural analysis of the welds

Microstructures of the base metals used in the study deviate from each other a lot when compared to similarity of chemical compositions of the materials, as it appears from figure 35. Cold rolled sheet metal has a typical cold rolled microstructure with direction of the

rolling clearly visible in the structure. Cold rolled material has a fine austenitic microstructure (measured ferrite content average 0.5 %). Microstructure of PBF sheets is fully austenitic, as measured ferrite content of the metal is 0 %. Typical microstructure of additively manufactured (layer by layer) microstructure is visible, and it visually corresponds to microstructures of PBF pieces in the studies of Casalino et al. (2013) and Zhang et al. (2013). Some pores can be detected in the microstructure.

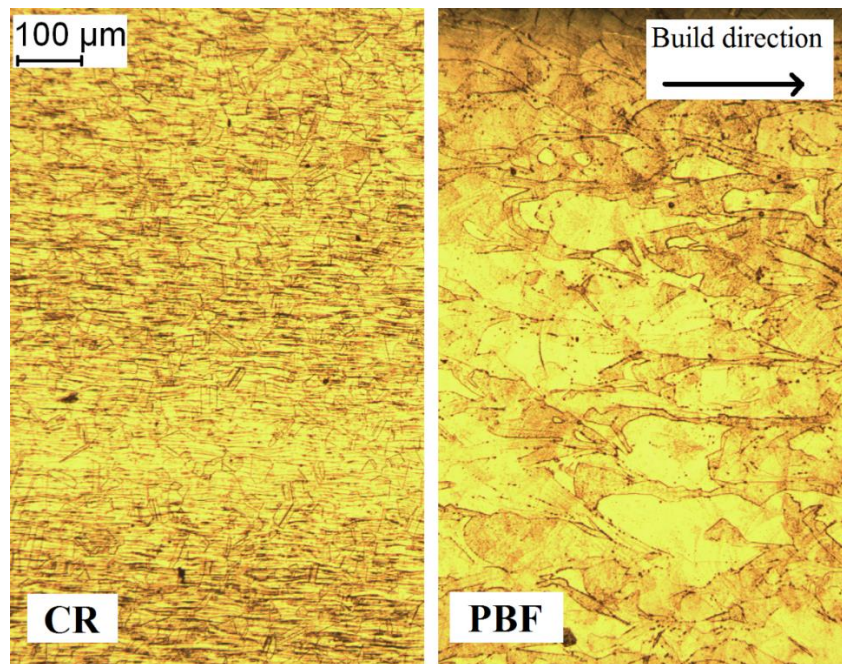


**Figure 35.** Microstructures of cold rolled sheet metal (CR) and PBF sheets used in the study.

#### 6.1.1 Predicted solidification of produced welds

Prediction of weld solidification based on use of WRC-1992 constitution diagram (presented in figure 36). Solidification of the welds in the study can be predicted to be primary austenitic (A-F) and/or primary ferritic (F-A or F-A-F) based on the information obtained from the diagram. Probability of primary austenitic solidification is elevated due to high welding speeds of laser welding. Ferrite content of produced welds can be expected to be from 0 to 6 %.

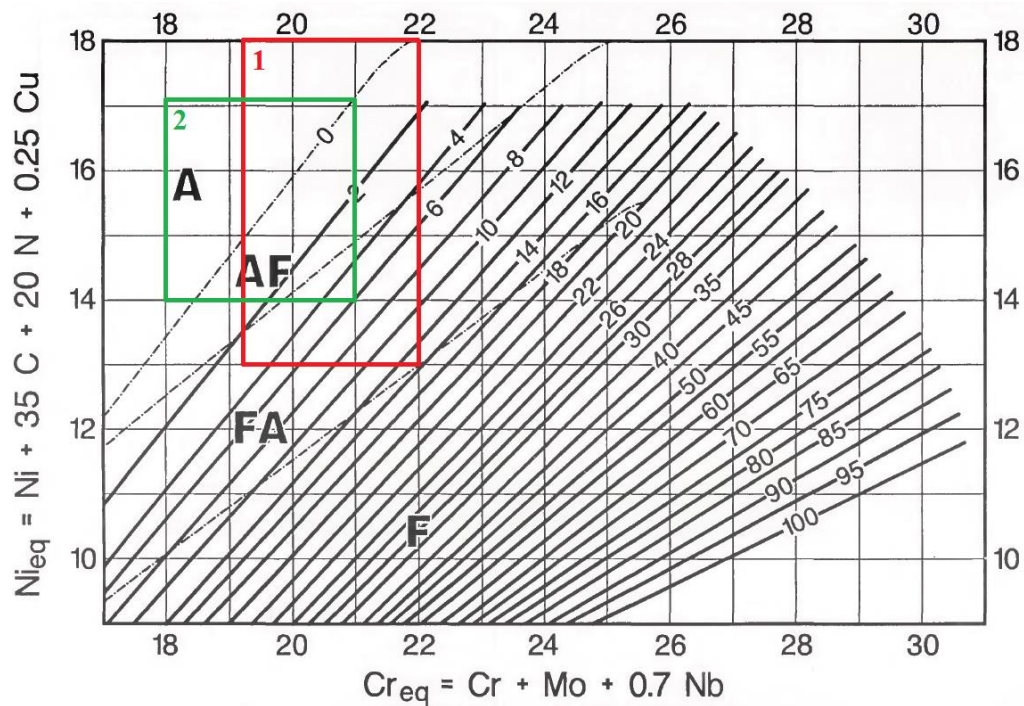


**Figure 36.** Predicted solidification of produced welds based on the chemical compositions of welded materials (presented in tables 2 and 3) using WRC-1992 diagram (modified from: Kotecki & Siewert, 1992, p. 176s). 1) EOS 316L powder and 2) Outokumpu 316L cold rolled sheet.

### 6.1.2 Detected weld solidification

All of the weld fusion zones in this study have similar multioriented microstructure of austenitic matrix mixed and fine reticulated ferrite mixed with long columnar austenite dendrites and interdendritic ferrite (figure 37) compared to weld microstructure in the study of Casalino et al. (2013). Detected structures of ferrite refer to primary austenitic solidification with formation eutectic ferrite (austenitic-ferritic solidification, A-F). All of the weld fusion zones also had areas next to fusion boundaries that had a fine and fuzzy structure of ferrite. This refers to primary ferritic solidification mode at the beginning of weld solidification. Some of the welds had similar structure growing from the cold rolled side of the fusion zone all away to weld centreline. Similar structure is not present in the same scale in the PBF side of the fusion zone. Detected primary ferritic solidification can be specified to be ferritic-austenitic solidification (F-A) based on the structure of the ferrite. However similar structure of ferrite could be formed by currents in molten weld pool during laser welding. SEM measurements are needed for specification of segregation

of alloying elements in the occurred structures of ferrite. More figures of weld microstructures are presented in appendix IV.

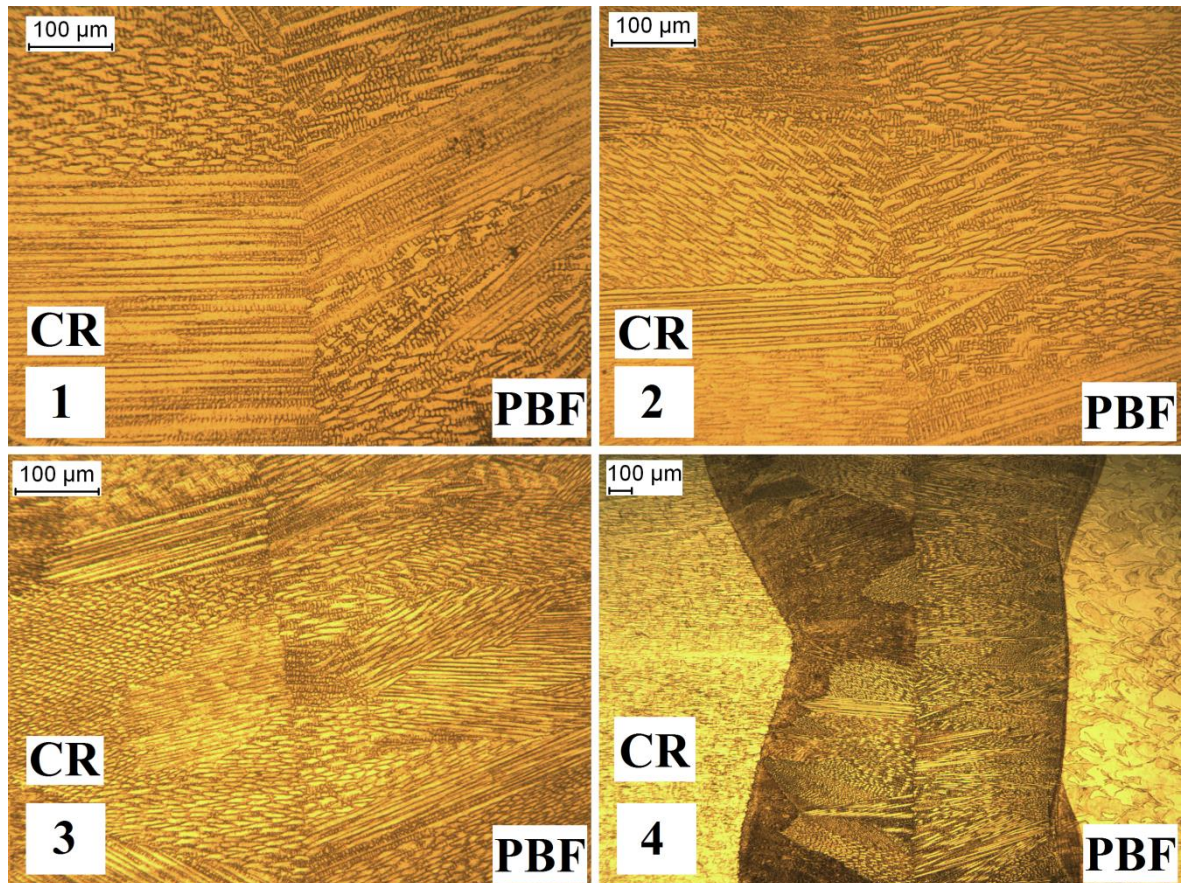


**Figure 37.** Microstructures of the welds produced using 300  $\mu\text{m}$  optical fiber diameter and 4.5 kW laser power. 1) Welding speed 1000 mm/min, 2) welding speed 2000 mm/min, and 3) welding speed 3000 mm/min. 4) Fine ferritic structure in austenitic matrix visible as a dark area starting from fusion boundary of CR side of the fusion zone.

### 6.1.3 SEM analysis

Multioriented grain growth in the weld fusion zone was suspected to result of segregation of alloying elements during PBF process based on the literature review (study of Casalino et al., 2013). Based on the results of Energy-Dispersive Analysis presented in appendix V/1-2, segregation in PBF fabricated sheets is significant. Measurements show stable concentrations of alloying elements between singular austenite cells. Only the pores visible in SEM pictures show variation in concentrations of nickel and chromium. Therefore segregation of alloying elements during PBF process is not expected to be cause behind multioriented grain growth. Occurred properties of the welds (multioriented grain growth

and occurred shapes of fusion zone boundaries) are suspected to be result from differences in melt pool behaviour between CR and PBF sides of the welds. These differences might have resulted from slight differences compositions or heat conductivities of materials used in this study.

SEM measurements of weld metals show both primary austenitic and primary ferritic solidification in the darker areas observed in the weld metal microstructures in this study. Energy-Dispersive Analysis (appendix V/3) shows typical segregation of primary ferritic solidification, where concentrations of nickel and chromium increase between dendrites, but concentration of nickel decreases and concentration of chromium increases towards ferritic dendrite core. Energy-Dispersive Analysis presented in appendix V/4 refers to primary austenitic solidification, where concentrations of nickel and chromium approach each towards boundary of austenitic dendrite. Solidification of the weld metals appears to have begun as primary ferritic and somewhere the solidification has turned into both primary austenitic and primary ferritic solidification mixed with each other. Weld solidification appears to have ended as primary austenitic.

#### 6.1.4 Ferrite contents of the welds

Ferrite content of the produced welds is approximately between 0.8 and 3 %. Amount of ferrite in the welds corresponds to the prediction based on WRC-1992 diagram. Amount of ferrite in the welds produced using 300  $\mu\text{m}$  optical fiber diameter is generally smaller (approximately from 0.8 to 2.6 % of ferrite) comparing to ferrite content of the welds produced using 600  $\mu\text{m}$  optical fiber diameter (approximately from 1.8 to 3 % of ferrite). Used ferrite measurement device might take disturbance from the surrounding material around the measurement point. Risk of error in the measurement is greatest in the narrow welds produced using 300  $\mu\text{m}$  optical fiber diameter. However ferrite contents of the welds are relatively close to ferrite contents of the base materials, consequently the amount of error in the measurements was estimated to be minimal. Increasing energy input increases the ferrite content of the weld, as it appears from figure 38.

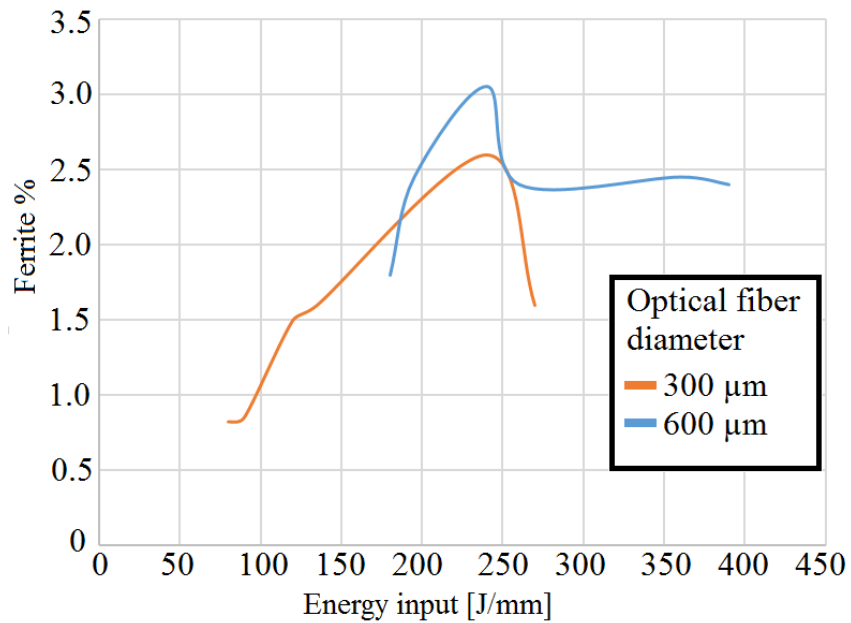


**Figure 38.** Effect of energy input on ferrite content of the welds with used optical fiber diameters.

## 6.2 Results of the bend tests

Bend tests were executed as it is described in experimental setup of this study. No defects or cracking was found during bend testing, and all of the welds passed the test. Smaller width of laser welds comparing to TIG welds promotes uniform behaviour of the weld metal and base metals, and generally lower heat input in laser welding prevent formation of critical changes in the HAZ. Laser welding was autogenous in this study, which reduces harmful effects (need of increasing heat input or microstructural effects caused by filler metal) of use of filler metal. Two of the bend tested specimens are presented in figure 39.



**Figure 39.** Bend tested FBB and RBB test pieces.

### 6.3 Results of the tensile tests

Measured ultimate tensile strengths of the welded samples were similar (between 500 and 600 MPa) comparing to studies of Casalino et al. (2013) and Järvinen (2014). All of samples welded using welding speed 1000 mm/min broke from the weld metal while samples welded using higher welding speeds broke from the base metal of PBF sheet. Ultimate tensile strengths of samples that broke from the base metal are just slightly higher (approximately from 5 to 10 MPa) comparing to the samples that broke from the weld metal, as it appears from appendix VI. Ultimate tensile strengths of the samples that broke from the base metals of the PBF sheets correspond to ultimate tensile strengths of the PBF sheets in the studies of Riemer et al. (2014), Yadroitsev et al. (2009) and Zhang et al. (2013) indicating that the ultimate tensile strength of PBF sheet metal was limiting factor for the ultimate tensile strength of samples welded with low energy input (welding speed above 1000 mm/min).

Welded work pieces that broke from the weld metal have significantly lower elongation at break comparing to samples that broke from the base metals of PBF sheets. Elongations of the samples that broke from the base metal of the PBF sheet have approximately 40-45 % elongation at break (except work pieces L9/10 that show decreased tensile strength due to high energy input and L11 that appears to have had defect in base metal of PBF sheet) which corresponds to elongations at break of PBF samples in the study of Riemer et al. (2014). Measured elongations at break correspond to the elongations at break of welded CR sheets in the study of Järvinen (2014). Increasing energy input appears to decrease elongations at break (with both 300  $\mu\text{m}$  and 600  $\mu\text{m}$  optical fiber diameters) in welds between PBF sheets and CR sheets, as it appears from figure 40.

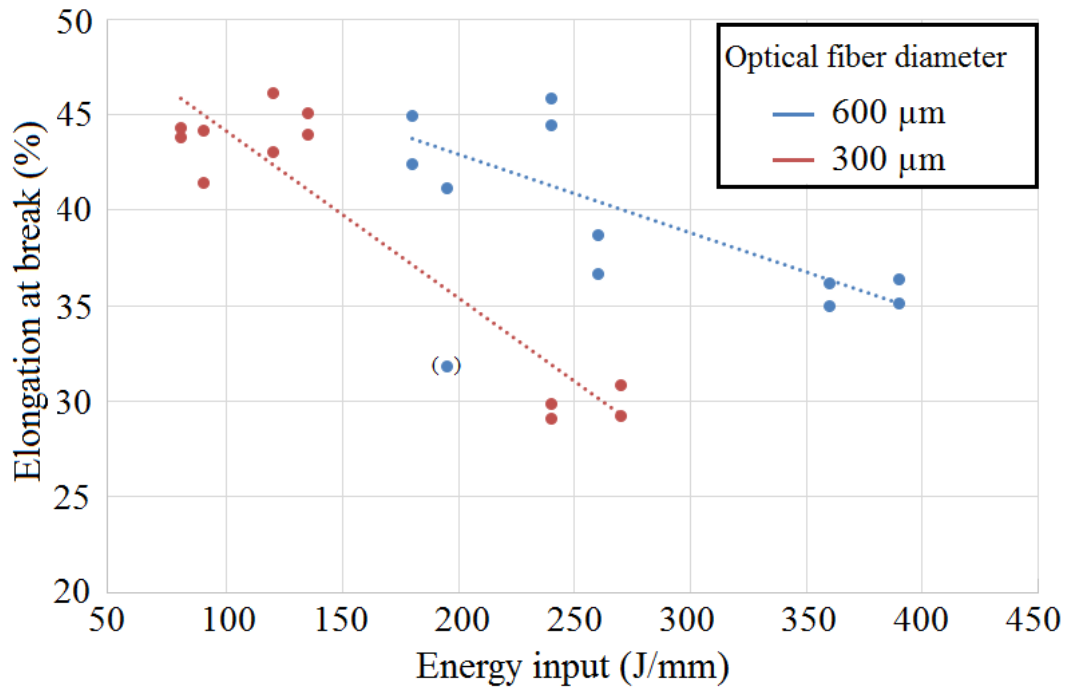


**Figure 40.** Effect of energy input on elongation at break.

### 6.3.1 Fracturing of the tensile test samples

Reduction of transverse cross-sectional area (necking) was significantly lower in the samples that broke from the weld metal comparing to the samples that broke from the PBF base metal, as it appears from figure 41. Differences in reduction of transverse cross-sectional areas are indication about low deformation properties of high energy input welds. Increasing energy input of the welding appears to have decreasing effect on deformation properties of the weld area, which also explains the lower elongations at break of high energy input samples comparing to those samples with lower energy input. Fracture surfaces in the high energy input samples were fairly straight comparing to the wavy fracture surfaces of low energy input samples. Higher reduction of transverse cross-sectional, higher elongations at break area and wavy fracture surfaces of low energy input samples indicate that fracturing of those samples was ductile. High energy input samples appear to have had more brittle fracturing based on straight fracture surfaces, low elongations at break and low reduction of reduction of transverse cross-sectional area. Fracturing of high energy input welds corresponds to fractures of the PBF welds observed by Casalino et al. (2013) and Järvinen (2014).



**Figure 41.** Tensile test samples: 1) fracturing from PBF base metal, and 2) fracturing from the weld.

## 7 CONCLUSIONS

Effect of energy input during autogenous laser keyhole welding on mechanical behaviour and microstructural characteristics of welds between PBF fabricated stainless steel 316L sheets and cold rolled sheet metal of same composition was studied. Optical fiber diameter, laser power and welding speed were varied during the experiments that were conducted according to OVAT-method. Based on literature review of the topic and executed experiments, following conclusions can be stated:

Previous studies indicated that welded PBF fabricated components may have same or higher ultimate tensile strength comparing to welded wrought material, but elongations at break are significantly lower. Orientation of building direction of PBF fabricated components comparing to weld direction affects elongations at break and the ultimate tensile strengths of the components. Based on the literature review, effect of heat treatment on ultimate tensile strength, elongation at break and fracturing of the PBF fabricated component is significant.

Laser welding of PBF fabricated stainless steel 316L sheets to cold rolled sheet metal of same composition is feasible and can produce good quality welds that have superior ultimate tensile strength comparing to PBF fabricated base metal. Use of 600  $\mu\text{m}$  optical fiber diameter appears to produce higher quality welds comparing to use of 300  $\mu\text{m}$  optical fiber diameter.

Multioriented grain growth in weld fusion zones occurs with both autogenous welding and welding with use of filler metal. Weld solidification mode and formation neck at fusion zone boundary on the cold rolled side of the weld fusion zone are dictated by weld pool flows, used material compositions and thermal conductive properties of the welded materials, since segregation during PBF process was not detected in the experiments. Both primary austenitic and primary ferritic solidification modes may occur during weld solidification of used materials.

Decreasing energy input affects fracturing of the welded samples and increases elongations at break of welded samples to same level (40-45%) with elongations at break of PBF fabricated and cold rolled base materials. Energy input of the welding was not detected to have significant effect on ultimate tensile strengths of the welded samples in this study. Lower elongations at break of high energy input samples comparing to lower energy input samples are explained by reducing effect of energy input of the welding on deformation properties of the welded samples. Energy input of the welding is to be considered as critical factor for welding of PBF fabricated stainless steel 316L components.

## **8 FURTHER STUDIES**

As it was stated earlier, weldability of powder bed fusion fabricated components has not been studied much, and a few ideas for topics of the further studies can be proposed based on the results of this study:

1. Weldability of powder bed fabricated components with other welding processes and effects of heat input on mechanical properties of the welds with these processes
2. Study about effect of different joint geometries on weldability of powder bed fabricated components, and restrictions of groove preparation to welding
3. Weldability of other metallic materials processed with PBF
4. Effect of post welding heat treatments on mechanical properties of welded PBF fabricated components
5. Effect of welding position on weldability of powder bed fabricated components
6. More specific analysis about fracturing behaviour of welded PBF fabricated components
7. Effect of other laser welding parameters on mechanical properties and microstructure of welded PBF fabricated components
8. Effect of PBF process parameters on weldability of the components

**REFERENCES**

Arivarasu, M., Vishnu, G., Hari, P. R., Vipin, V. P., Kaushik, K., Gokulkumar, K., Manikandan, M., Devendranath, R. K. & Arivazhagan, N. 2014. Micro-segregation studies on the Continuous Nd: YAG Laser Beam Welded AISI 316L. *Procedia Engineering* 97. P. 892-901.

ASM International. 1993. *ASM Handbook volume 6: Welding, Brazing and Soldering*. 10<sup>th</sup> Edition. 2873 P.

Brooks, J. A. 1990. Weld microsegregation: modeling and segregation effects on weld performance. P. 41-47. *Weldability of materials*. ASM International, Ohio. 351 P.

Brooks, J. A., Thompson, A. W. & Williams, J. C. 1984. A Fundamental Study of the Beneficial Effects of Delta Ferrite in Reducing Weld Cracking. *Welding Journal* (Issue 3/1984). P. 71s-83s.

Casalino, G., Campanelli, S. L. & Ludovico, A. D. 2013. Laser-arc hybrid welding of wrought to selective laser molten stainless steel. *International Journal of Advanced Manufacturing Technology* 68. P. 209-216.

Castro, R. J. & Cadenet, J. J. 1975. *Metallurgy of stainless and heat-resisting steels*. Syndics of Cambridge University Press. London. 190 P.

Chandel, R. S. & Bala, S. R. 1985. Cooling Time and Features of Submerged Arc Weld Beads. *Welding Journal* (Issue 7/1985). P. 201s-208s

Cieslak, M. J., Ritter, A. M. & Savage, W. F. 1982. Solidification Cracking and Analytical Electron Microscopy of Austenitic Stainless Steel Weld Metals. *Welding Journal* (Issue 1/1982). P. 1s-8s.

Cooch, T. G. & Honeycombe, J. 1980. Welding Variables and Microfissuring in Austenitic Stainless Steel Weld Metal. *Welding Journal* (Issue 8/1980). P. 225s-244s.

Dahotre, N. B. & Harimkar, S. P. 2008. *Laser Fabrication and Machining of Materials*. Springer Science + Business Media, LCC. New York. 558 P.

David, S. A., Vitek, J. M. & Hebble, T. L. 1987. Effect of Rapid Solidification on Stainless Steel Weld Metal Microstructures and Its Implications on the Schaeffler Diagram. *Welding Journal* (Issue 10/1987). P. 289s-300s.

Elmer, J. W., Allen, S. M. & Eagar, T. W. 1989. Microstructural Development during Solidification of Stainless Steel Alloys. *Metallurgical Transactions A* 20. P. 2117-2131.

Fabbro, R. 2010. Melt pool and keyhole behaviour analysis for deep penetration laser welding. *Journal of Physics D: Applied Physics* 43 (2010) issue 44. 9 P.

Gibson, I., Rosen, D. W. & Stucker, B. 2010. *Additive Manufacturing Technologies: Rapid Prototyping to Direct Digital Manufacturing*. Springer. New York. 459 P.

Glicksman, M. E. 2011. *Principles of Solidification*. Springer. New York. 520 P.

Gooch, T. G. 1990. Solidification cracking of austenitic stainless steels. P. 31-40. *Weldability of materials*. ASM International, Ohio. 351 P.

Gu, D., Meiners, W., Poprawe, R. & Wissenbach, K. 2012. Laser additive manufacturing of metallic components: materials, processes and mechanisms. *International materials reviews* 57. P. 133-164.

Gu, D. & Shen, Y. 2009. Balling phenomena in direct laser sintering of stainless steel powder: Metallurgical mechanisms and control methods. *Materials and Design* 30. P. 2903-2910.

Hafez, K.M. & Katayama, S. 2009. Fiber laser welding of AISI 304 stainless steel plates. Quarterly Journal of The Japan Welding Society 31. P. 69-73.

Ion, J. C. 2005. Laser processing of engineering materials: principles, procedure and industrial application. Elsevier Butterworth-Heinemann. 576 P.

Islam, M., Purtonen, T., Piili, H., Salminen, A. & Nyrhilä, O. Temperature profile and imaging analysis of laser additive manufacturing of stainless steel. Physics Procedia 41. P. 835-842.

Järvinen, J-P. 2014. Welding of additively manufactured stainless steel parts: comparative study between sheet metal and selective laser melted parts. Master's Thesis. Lappeenranta University of Technology. 68 P.

Kamath, C., El-dasher, B., Gallegos, G. F., King, W. E. & Sisto, A. 2014. Density of additively-manufactured, 316L SS parts using laser powder-bed fusion at powers up to 400W. International Journal of Advanced Manufacturing Technology 74. P. 65-78.

Kawahito, Y., Mizutani, M. & Katayama, S. 2007. Investigation of high-power welding phenomena of stainless steel. Transactions of JWRI 36 (No.2). P. 1-6.

Ki, Mohanty & Mazumder, 2002 Modeling of Laser Keyhole Welding: Part II. Simulation of Keyhole Evolution, Velocity, Temperature Profile, and Experimental Verification. Metallurgical and Materials Transactions A 33. P. 1831-1842.

Kotecki, D. J. & Siewert, T. A. 1992. WRC-1992 Constitution Diagram for Stainless Steel Weld Metals: A Modification of the WRC-1988 diagram. Welding Journal (Issue 5/1992). P. 171s-178s.

Kou, S. 2003. Welding Metallurgy, 2nd Edition. John Wiley & Sons, New Jersey. 461 P.

Kruth, J.-P., Badrossamay, M., Yasa, E., Deckers, J., Thijs, L. & Van Humbeeck, J. 2010. Part and material properties in selective laser melting of metals. 16th International Symposium on Electromachining. 12 P.

Kujanpää, V. 2014. Thick-section laser and hybrid welding of austenitic stainless steels. *Physics Procedia* 56. P. 630-636.

Kujanpää, V., Salminen, A. & Vihinen, J. 2005. Lasertyöstö. Teknologiainfo Teknova. Helsinki. 373 P.

Kumar, A. & Debroy, T. 2005. Tailoring complex weld geometry through reliable heat-transfer and fluid-flow calculations and a genetic algorithm. *Metallurgical and Materials Transactions A - Physical Metallurgy and Materials Science* 36. P. 2725-2735.

Kumar, S. & Shahi, A. S. 2011. Effect of heat input on the microstructure and mechanical properties of gas tungsten arc welded AISI 304 stainless steel joints. *Materials and Design* 32. P. 3617-3623.

Kyröläinen, A. & Lukkari, J. 2002. Ruostumattomat teräkset ja niiden hitsaus. *Metalliteollisuuden Keskusliitto, MET*. Volume 12/2002. 526 P.

Lancaster, J. F. 1999. *Metallurgy of Welding, Sixth Edition*. Abington Publishing, Cambridge. 464 P.

Leone, G. L. & Kerr, H. W. 1982. The Ferrite to Austenite Transformation in Stainless Steels. *Welding Journal* (Issue 1/1982). P. 13s-22s.

Li, R., Liu, J., Shi, Y., Wang, L. & Jiang, W. 2012. Balling behavior of stainless steel and nickel powder during selective laser melting process. *The International Journal of Advanced Manufacturing Technology* (59). P. 1025-1035.

Li, R., Shi, Y., Wang, Z., Wang, L., Liu, J. & Jiang, W. 2010. Densification behaviour of gas and water atomized 316L stainless steel powder during selective laser melting. *Applied Surface Science* 256. p. 4350-2356.

Lippold, J. C. 1994. Solidification Behaviour and Cracking Susceptibility of Pulsed-Laser Welds in Austenitic Stainless Steels. *Welding Journal* (Issue 6/1994). P. 129s-139s.

Lippold, J. C. 2014. *Welding Metallurgy and Weldability*. John Wiley & Sons, Inc., New Jersey. 408 P.

Lippold, J. C. & Kotecki, D. J. 2005. *Welding Metallurgy and Weldability of Stainless Steels*. John Wiley & Sons, Inc., New Jersey. 357 P.

Lippold, J. C. & Savage, W. F. 1979. Solidification of Austenitic Stainless Steel Weldments: Part I - A Proposed Mechanism. *Welding Journal* (Issue 12/1979). P. 225s-244s.

Lippold, J. C. & Savage, W. F. 1980. Solidification of Austenitic Stainless Steel Weldments: Part I - The Effect of Alloy Composition on Ferrite Morphology. *Welding Journal* (Issue 2/1980). P. 48s-58s.

Matilainen, V., Piili, H., Salminen, A., Syvänen, T. & Nyrhilä, O. 2014. Characterization of Process Efficiency Improvement in Laser Additive Manufacturing. *Physics Procedia* 56. P. 317-326.

Matsunawa, A. 2002. Science of laser welding - mechanisms of keyhole and pool dynamics. ICALEO 2002 proceedings, Phoenix, October 2002. LIA, Orlando, paper 101

McGuire, M. F. 2008. *Stainless Steels for Design Engineers*. ASM International, Ohio. 304 P.

Miekk-oja, H. M. 1986. *Uudistettu Miekk-ojan metallioppi*. Otava. Helsinki. 841P.

Nelson, T. W., Lippold, J. C. & Mills, M. J. 1999. Nature and Evolution of the Fusion Boundary in Ferritic-Austenitic Dissimilar Weld Metals, Part 1 — Nucleation and Growth. *Welding Journal* (Issue 10/1999). P. 329s-337s.

Piekarska, W. & Kubiak, M. 2012. Theoretical investigations into heat transfer in laser welded steel sheets. *Journal of Thermal Analysis and Calorimetry* 110. P. 159-166.

Pinnow, K. E. & Moskowiz, A. 1970. Corrosion Resistance of Stainless Steel Weldments. *Welding Journal* (Issue 6/1970). P. 278s-284s.

Rai, R., Kelly, S.M. Martukanitz, R.P. & DebRoy, T. 2008 A Convective Heat-Transfer Model for Partial and Full Penetration Keyhole Mode Laser Welding of a Structural Steel. *Metallurgical and Materials Transactions A* 39. P. 98–112.

Riemer, A., Leuders, S., Thone, M., Richard, H. A., Troster, T. & Niendorf, T. 2014. On the fatigue crack growth behavior in 316L stainless steel manufactured by selective laser melting. *Engineering Fracture Mechanics* 120. P. 15-25.

Schleifenbaum, H., Meiners, W., Wissenbach, K. & Hinke, C. 2010. Individualized production by means of high power Selective Laser Melting. *CIRP Journal of Manufacturing Science and Technology* 2. P. 161-169.

Scopus. 2015. Referred 7.3.2015. Available: [http://www-scopus-com.ezproxy.cc.lut.fi/term/analyzer.url?sid=E49AE0C514D458EE699B7FD650EFD1EF.zQKnzAySRvJOZYcdfIziQ%3a2530&origin=resultslist&src=s&s=TITLE-ABS-KEY%28"powder+bed+fusion"+OR+"additive+manufacturing"%29&sort=plf-f&sdt=b&sot=b&sl=62&count=2580&analyzeResults=Analyze+results&txGid=E49AE0C514D458EE699B7FD650EFD1EF.zQKnzAySRvJOZYcdfIziQ%3a259](http://www-scopus-com.ezproxy.cc.lut.fi/term/analyzer.url?sid=E49AE0C514D458EE699B7FD650EFD1EF.zQKnzAySRvJOZYcdfIziQ%3a2530&origin=resultslist&src=s&s=TITLE-ABS-KEY%28)

SFS 3052. 1995. Welding terminology. General terms. Finnish Standards Association, Helsinki. Approved: 25.9.1995. 122 P.

SFS-EN ISO 4136. 2012. Destructive tests on welds in metallic materials. Transverse tensile test. Finnish Standards Association, Helsinki. Approved: 10.12.2012. 21 P.

SFS-EN ISO 5173 + A1. 2011. Destructive tests on welds in metallic materials. Bend tests. Finnish Standards Association, Helsinki. Approved 12.12.2011. 35 P.

SFS-EN 10088-1. 2014. Stainless steels - Part 1: List of stainless steels. Finnish Standards Association, Helsinki. Approved: 24.11.2014. 67 P.

Signes, E. G. 1972. A Simplified Method for Calculating Cooling Rates in Mild and Low Alloy Steel Weld Metals. *Welding Journal* (Issue 10/1972). P. 473s-484s.

Simchi, A. 2006. Direct laser sintering of metal powders: Mechanism, kinetics and microstructural features. *Materials Science and Engineering A* 428. P. 148-158.

Steen, W.M & Mazumder, J. 2010. *Laser Material Processing*. Springer. 558 p.

Outokumpu. 2013. *Handbook of Stainless Steel*. Outokumpu Oyj, Espoo, Finland. 92 P.

Van Belle, L., Vansteenkiste, G. & Boyer, J.C. 2012. Comparisons of Numerical Modelling of the Selective Laser Melting. *Key Engineering Materials* 504-506. P. 1067-1072.

Vitek, J. M. & David, S. A. 1986. The Sigma Phase Transformation in Austenitic Stainless Steels. *Welding Journal* (Issue 4/1986). P. 106s-112s.

Vänskä, M., Abt, F., Weber, R., Salminen, A. & Graf, T. 2013. Effects of welding parameters onto keyhole geometry for partial penetration laser welding. *Physics Procedia* 41. P. 199-208.

Zhang, B., Dembinski, L. & Coddet, C. 2013. The study of the laser parameters and environment variables effect on mechanical properties of high compact parts elaborated by selective laser melting 316L powder. *Materials Science & Engineering A* 584. P. 21-31.

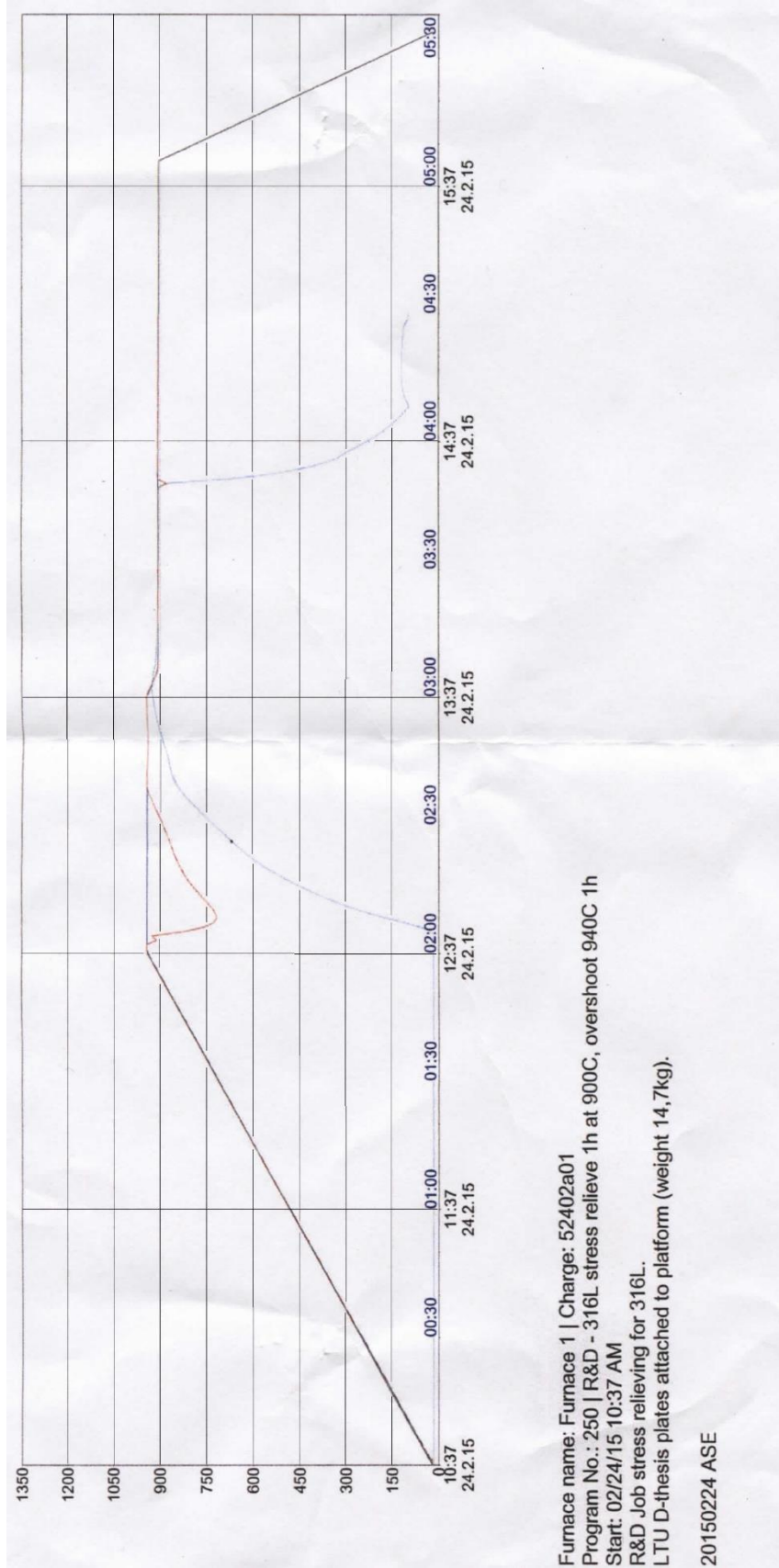
Yadroitsev, I., Pavlov, M., Bertrand, Ph. & Smurov, I. 2009. Mechanical properties of samples fabricated by selective laser melting. 14èmes Assises Européennes du Prototypage & Fabrication Rapide. June 2009, Paris. 6 P.

Yadroitsev, I. & Smurov, I. 2011. Surface Morphology in Selective Laser Melting of Metal Powders. Physics Procedia 12. P. 264-270.

You, D., Gao, X. & Katayama, S. 2014. Monitoring of high-power laser welding using high-speed photographing and image processing. Mechanical systems and signal processing 49. P. 39-52.

APPENDIX I  
Stress relieving heat treatment

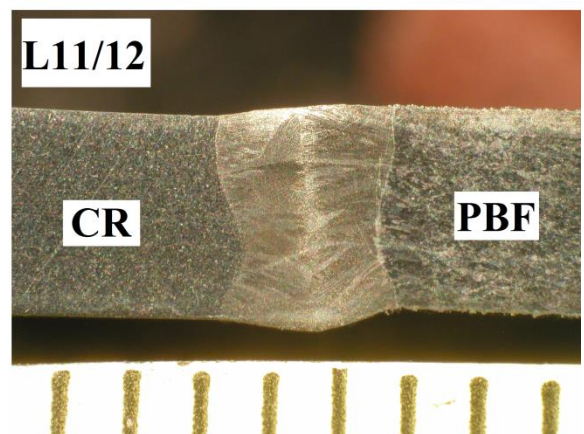
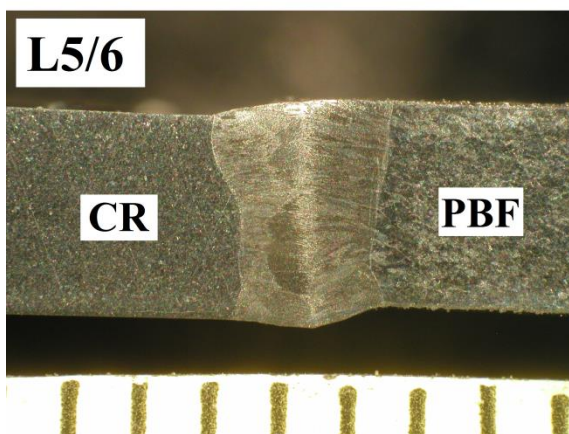
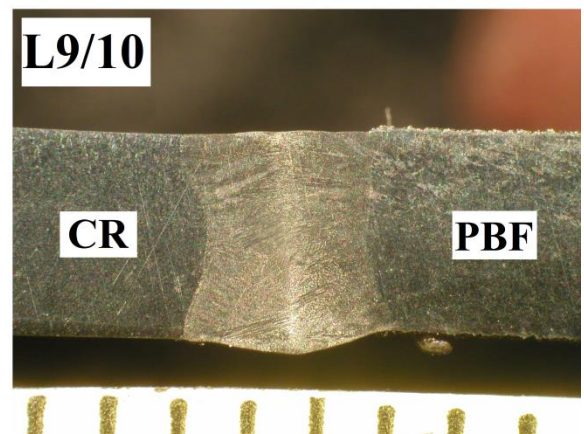
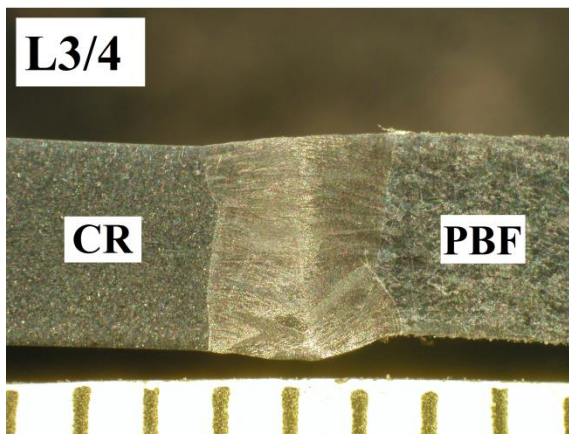
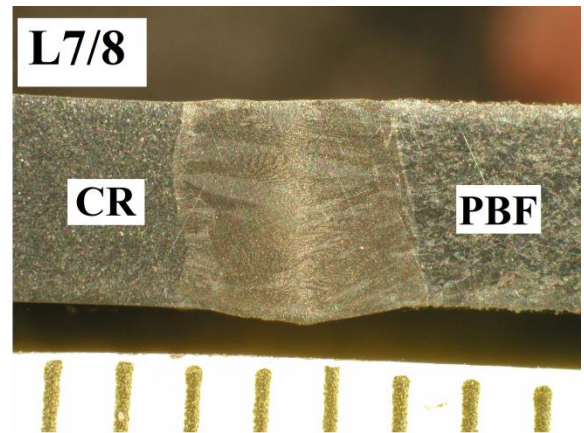
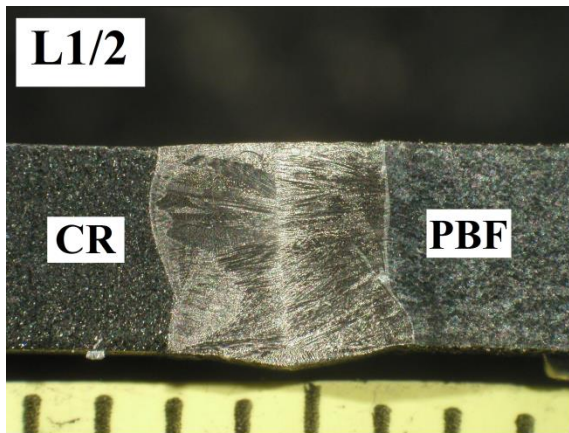
**STRESS RELIEVING HEAT TREATMENT OF PBF  
FABRICATED SHEETS**



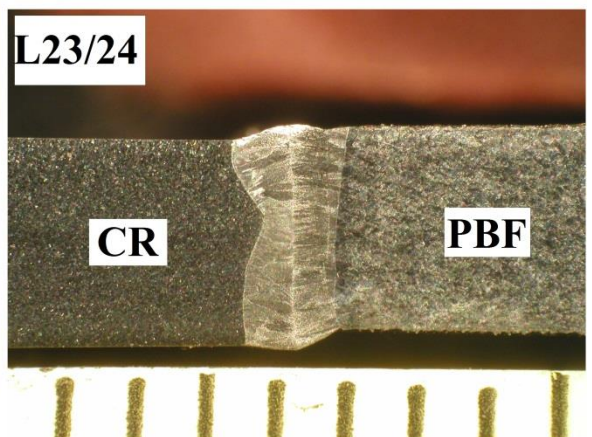
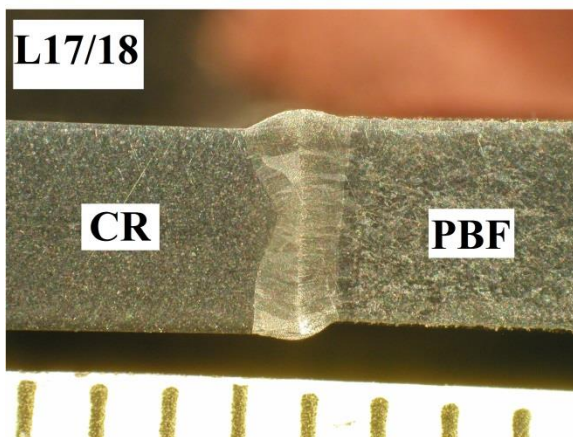
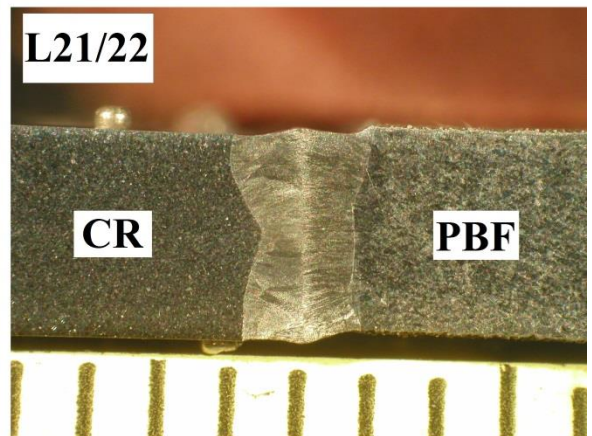
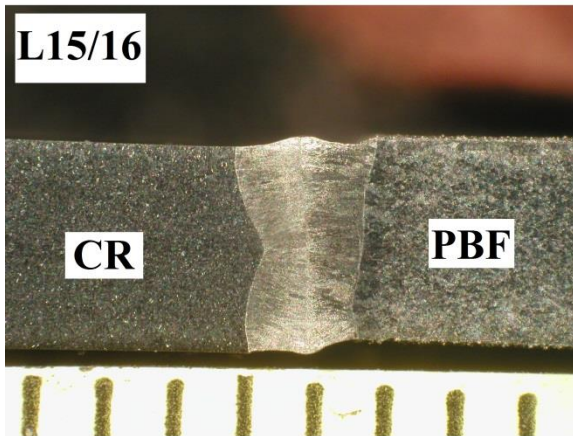
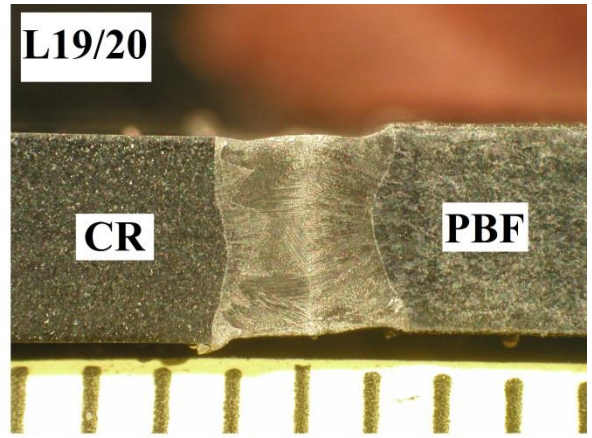
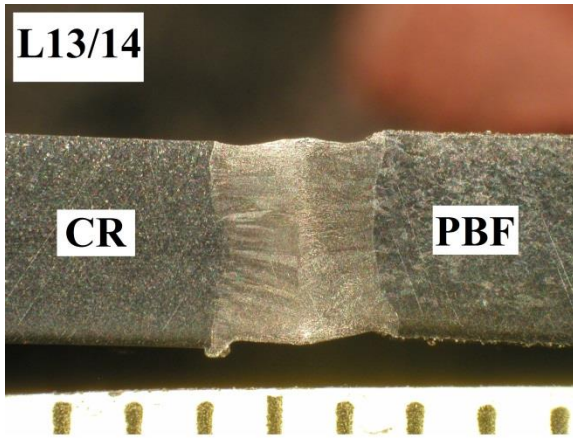
APPENDIX II  
Used laser welding parameter sets

Test number	Optical fiber diameter (μm)	Laser power (kW)	Welding speed (mm/min)	Energy input (J/mm)
L1	600	6.0	1000	360
L2	600	6.0	1000	360
L3	600	6.0	1500	240
L4	600	6.0	1500	240
L5	600	6.0	2000	180
L6	600	6.0	2000	180
L7	600	6.5	1000	390
L8	600	6.5	1000	390
L9	600	6.5	1500	260
L10	600	6.5	1500	260
L11	600	6.5	2000	195
L12	600	6.5	2000	195
L13	300	4.0	1000	240
L14	300	4.0	1000	240
L15	300	4.0	2000	120
L16	300	4.0	2000	120
L17	300	4.0	3000	80
L18	300	4.0	3000	80
L19	300	4.5	1000	270
L20	300	4.5	1000	270
L21	300	4.5	2000	135
L22	300	4.5	2000	135
L23	300	4.5	3000	90
L24	300	4.5	3000	90

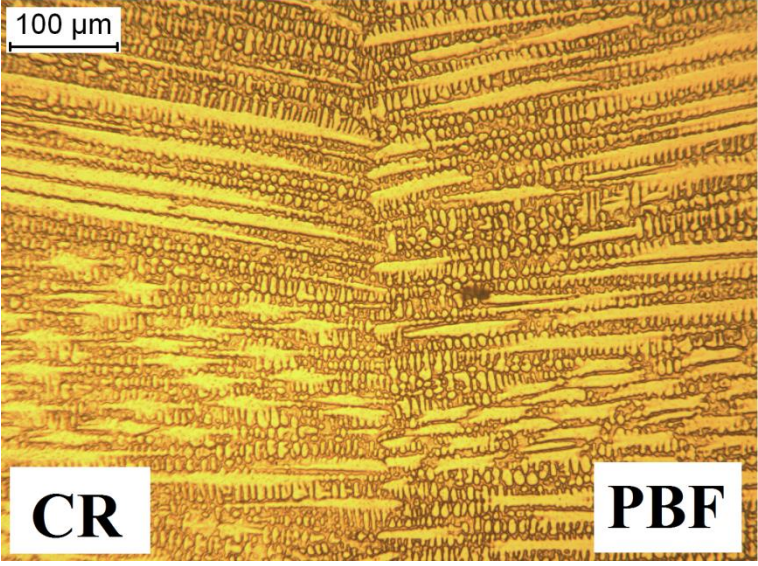
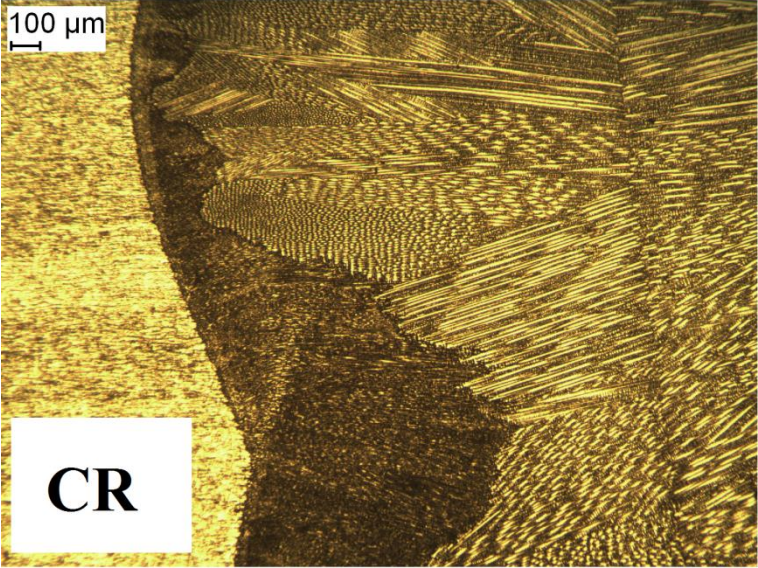
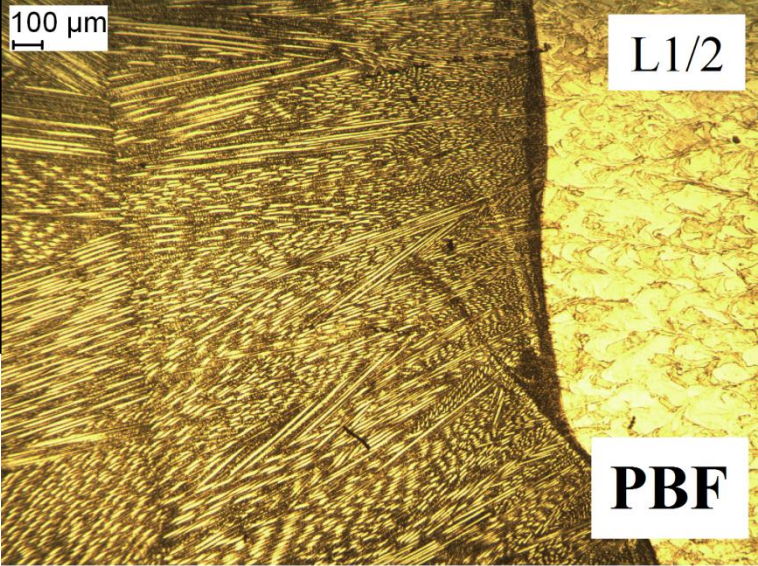
APPENDIX III, 1  
Weld macrographs



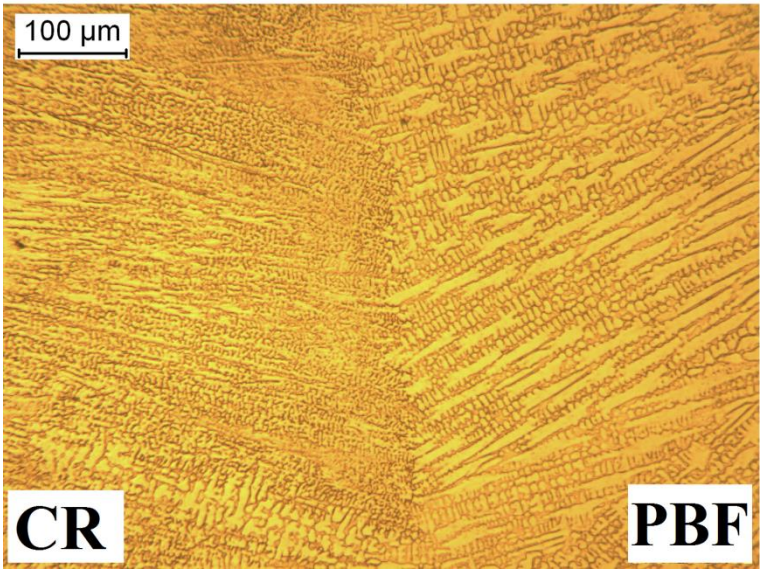
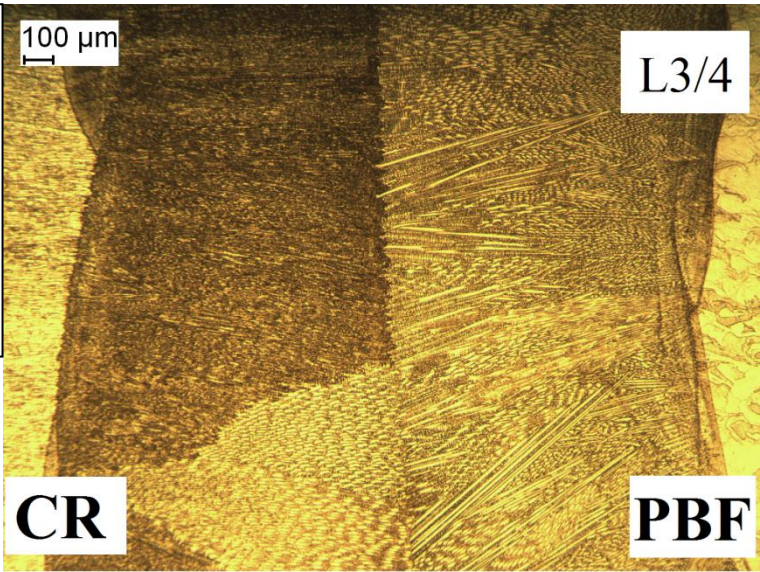
APPENDIX III, 2  
Weld macrographs



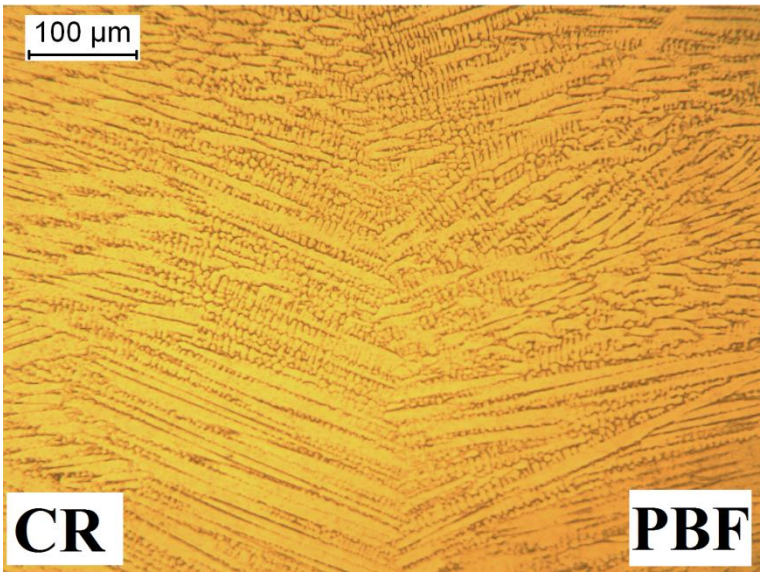
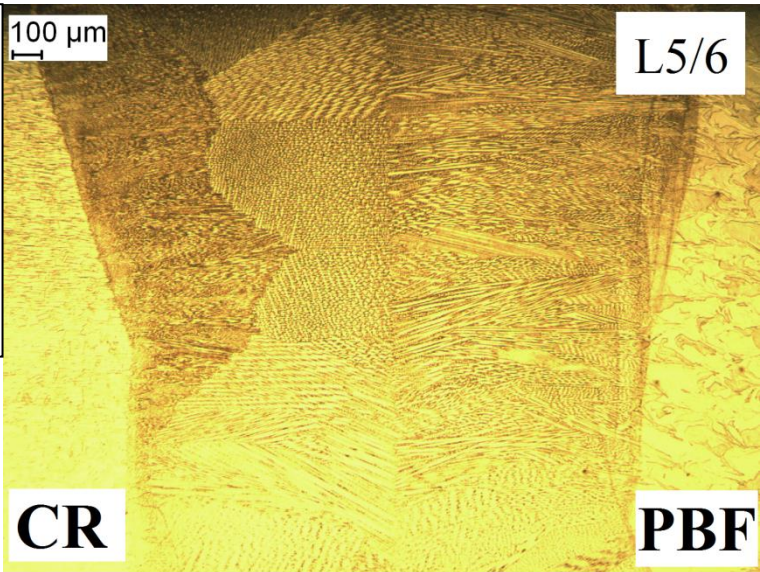
Sample: L1 and L2  
Solidification: A-F, F-A  
Optical fiber diameter: 600  $\mu\text{m}$   
Laser power: 6 kW  
Welding speed: 1000 mm/min  
Energy input: 360 J/mm



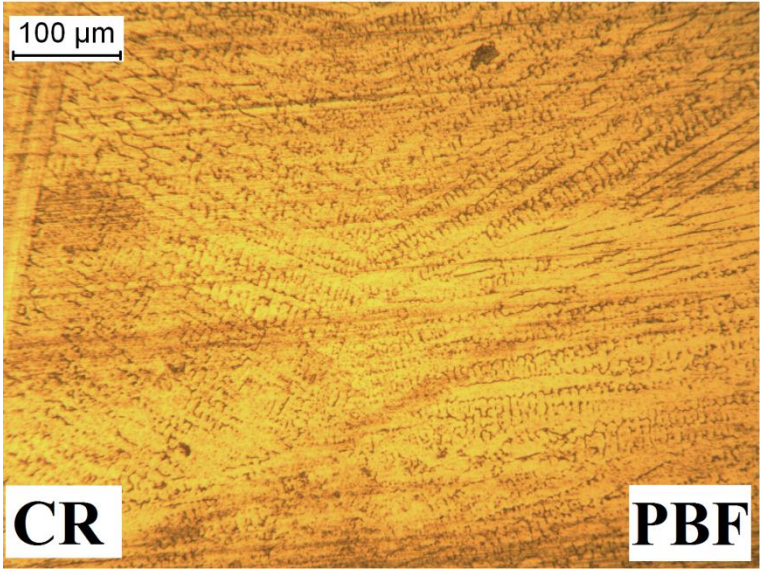
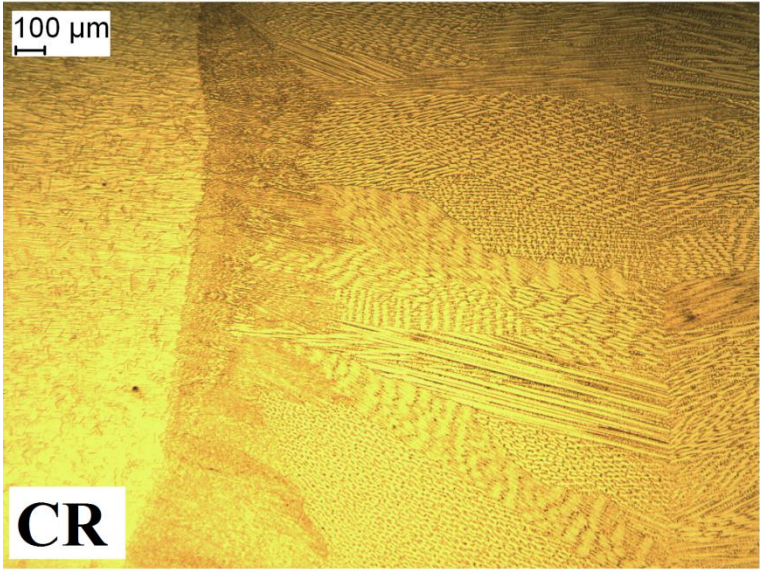
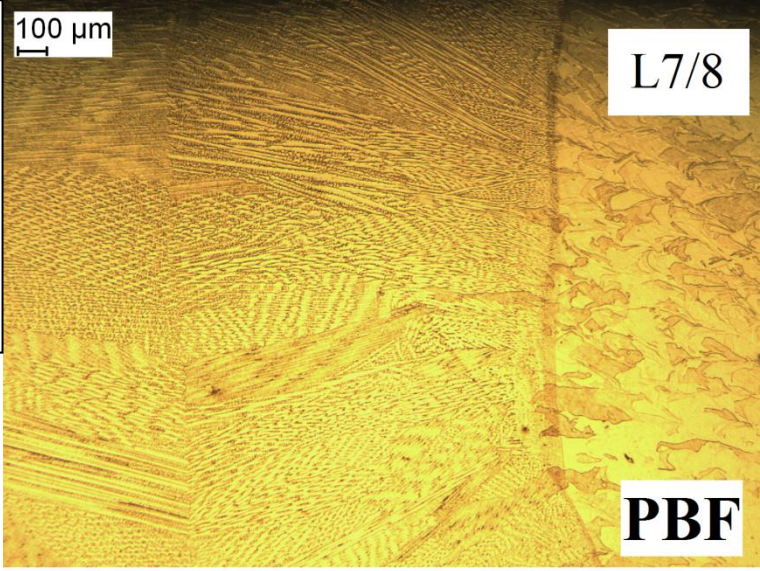
Sample: L3 and L4  
Solidification: A-F, F-A  
Optical fiber diameter: 600  $\mu\text{m}$   
Laser power: 6 kW  
Welding speed: 1500 mm/min  
Energy input: 240 J/mm



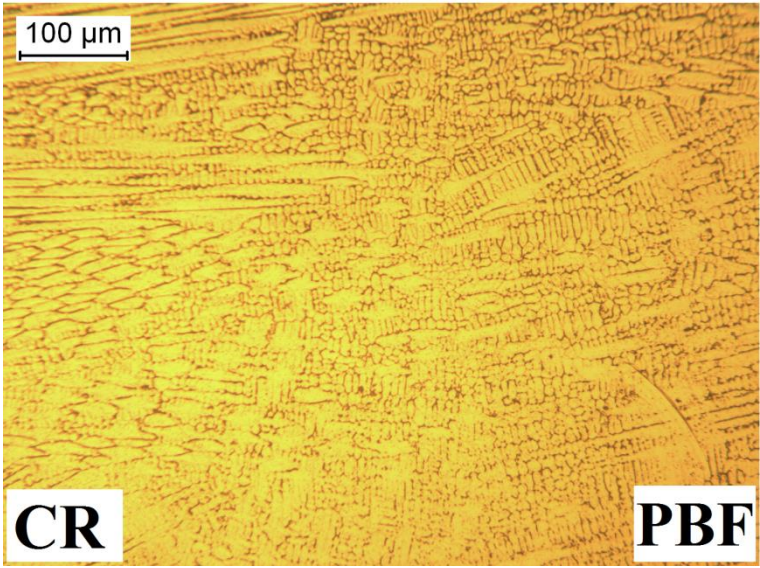
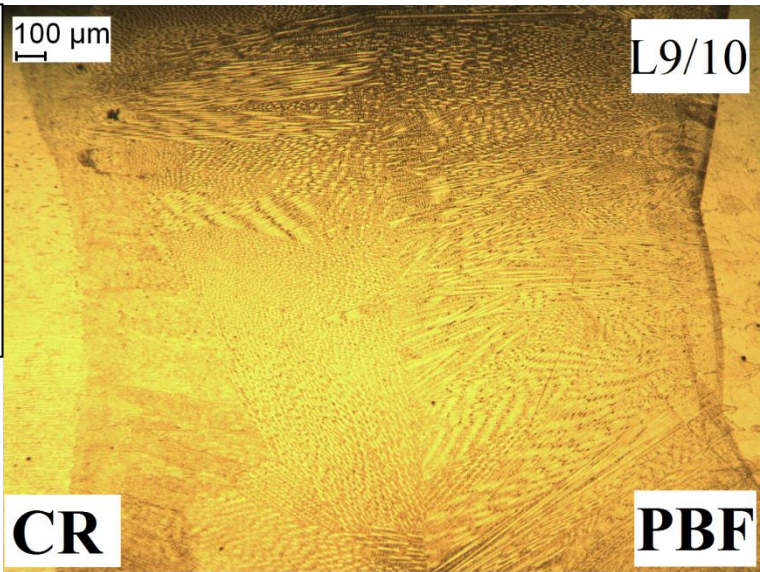
Sample: L5 and L6  
Solidification: A-F, F-A  
Optical fiber diameter: 600  $\mu\text{m}$   
Laser power: 6 kW  
Welding speed: 2000 mm/min  
Energy input: 180 J/mm



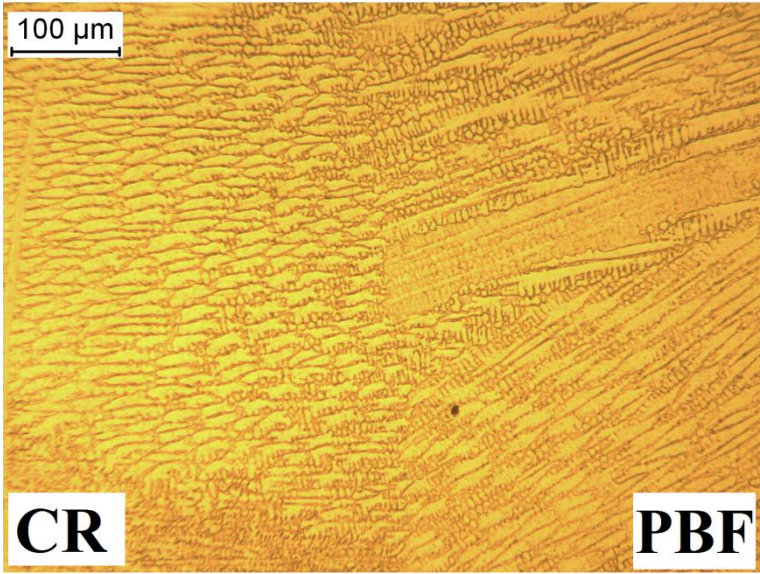
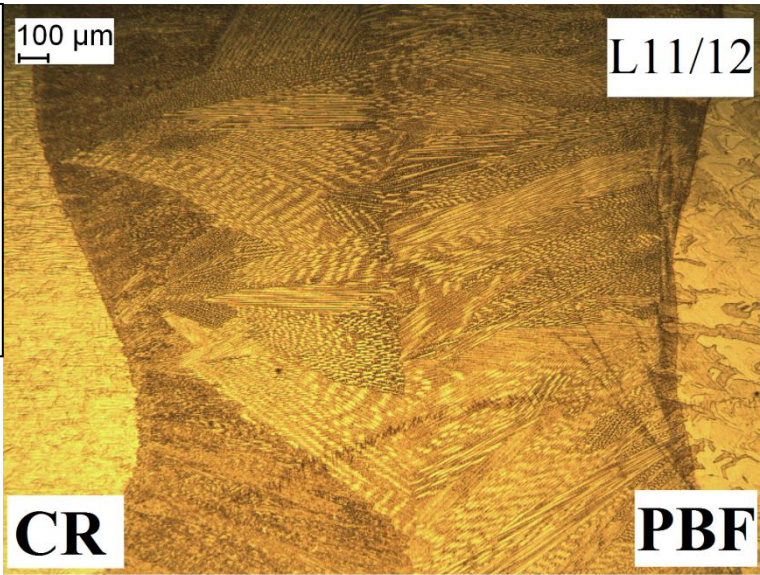
Sample: L7 and L8  
Solidification: A-F, F-A  
Optical fiber diameter: 600  $\mu\text{m}$   
Laser power: 6.5 kW  
Welding speed: 1000 mm/min  
Energy input: 390 J/mm



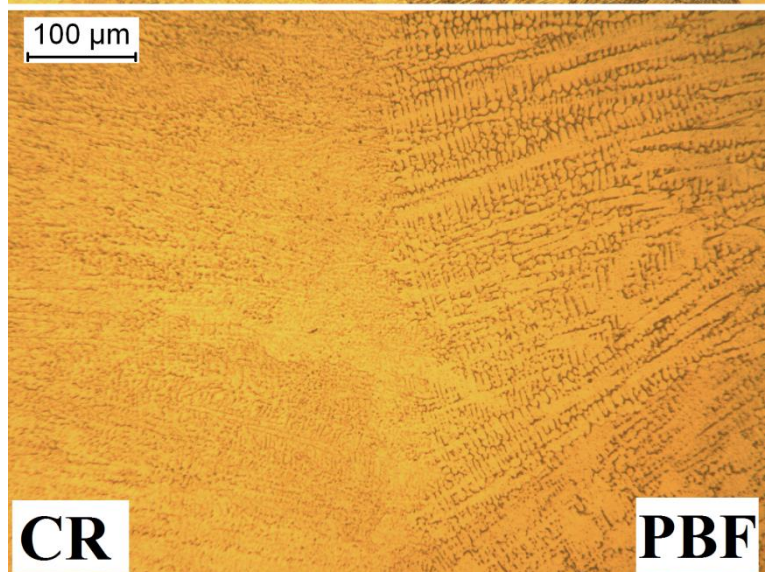
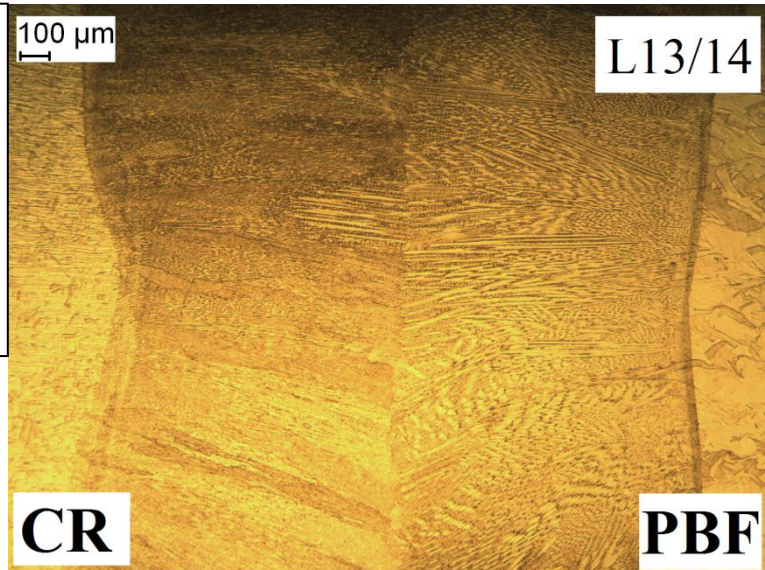
Sample: L9 and L10  
Solidification: A-F, F-A  
Optical fiber diameter: 600  $\mu\text{m}$   
Laser power: 6.5 kW  
Welding speed: 1500 mm/min  
Energy input: 260 J/mm



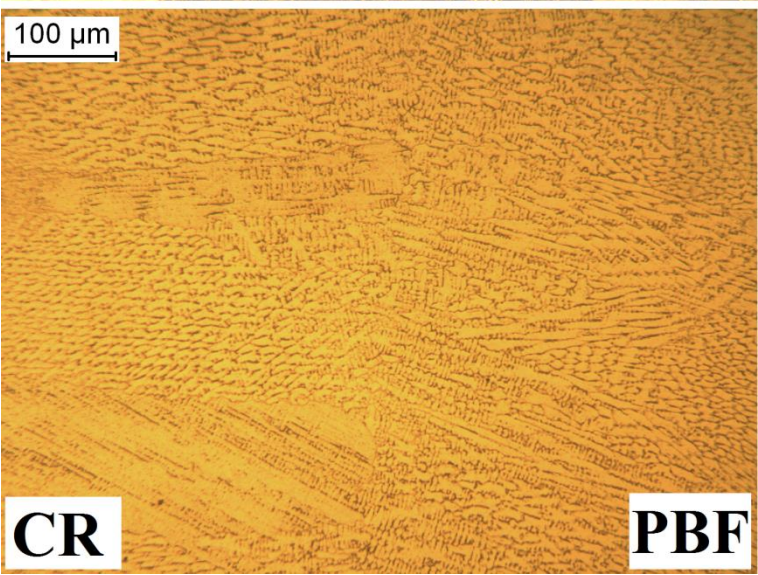
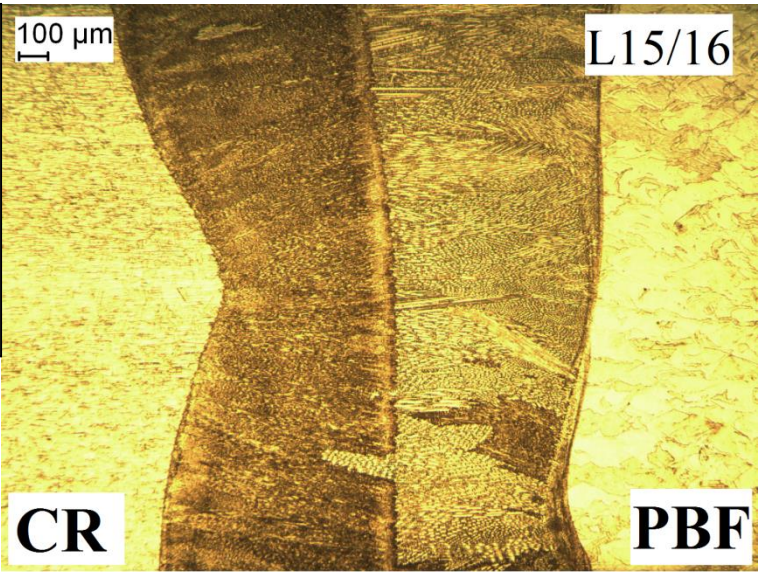
Sample: L11 and L12  
Solidification: A-F, F-A  
Optical fiber diameter: 600  $\mu\text{m}$   
Laser power: 6.5 kW  
Welding speed: 2000 mm/min  
Energy input: 195 J/mm



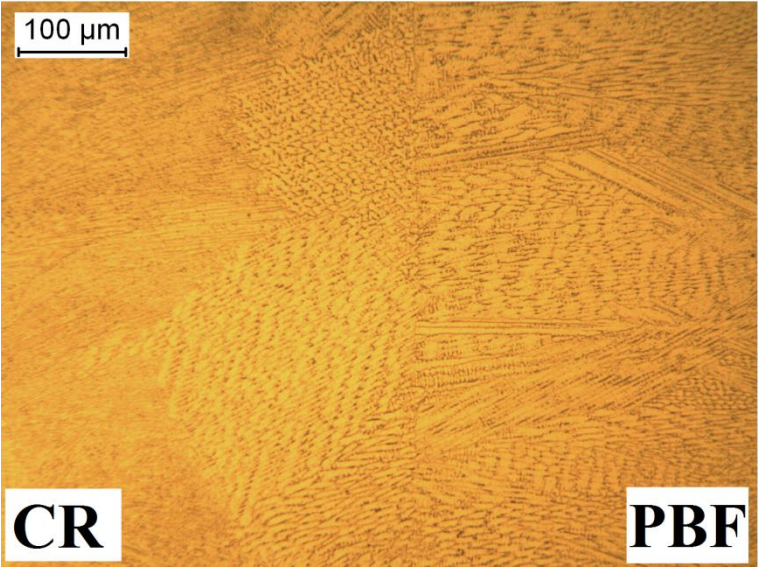
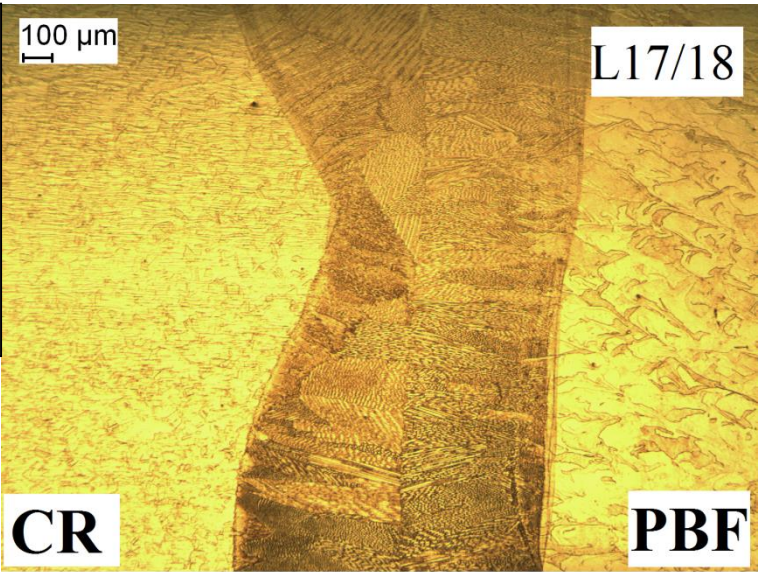
Sample: L13 and L14  
Solidification: A-F, F-A  
Optical fiber diameter: 300  $\mu\text{m}$   
Laser power: 4 kW  
Welding speed: 1000 mm/min  
Energy input: 240 J/mm



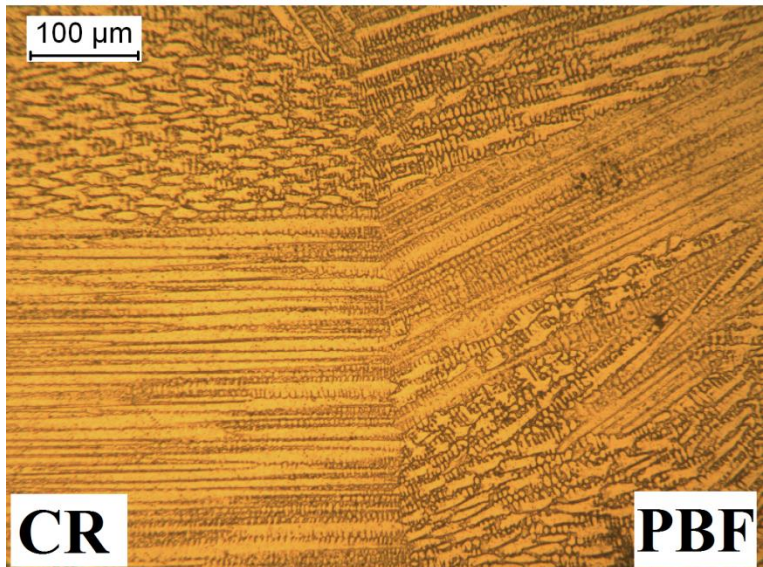
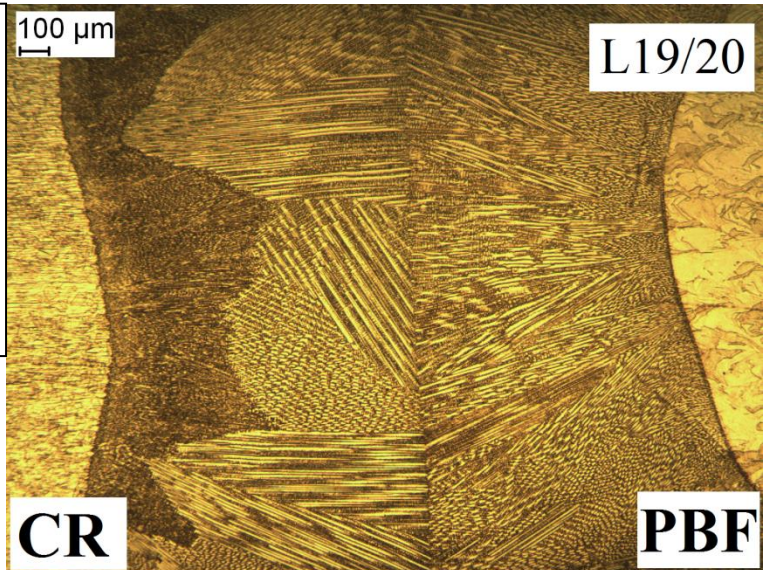
Sample: L15 and L16  
Solidification: A-F, F-A  
Optical fiber diameter: 300  $\mu\text{m}$   
Laser power: 4 kW  
Welding speed: 2000 mm/min  
Energy input: 120 J/mm



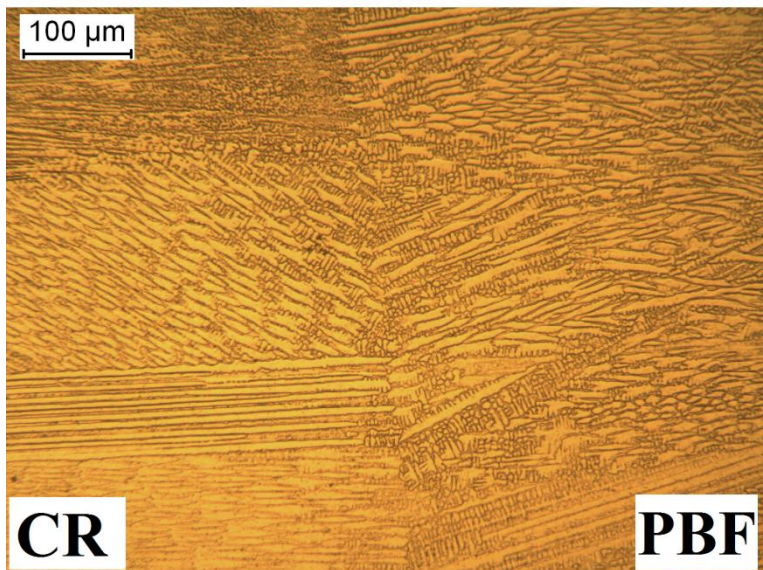
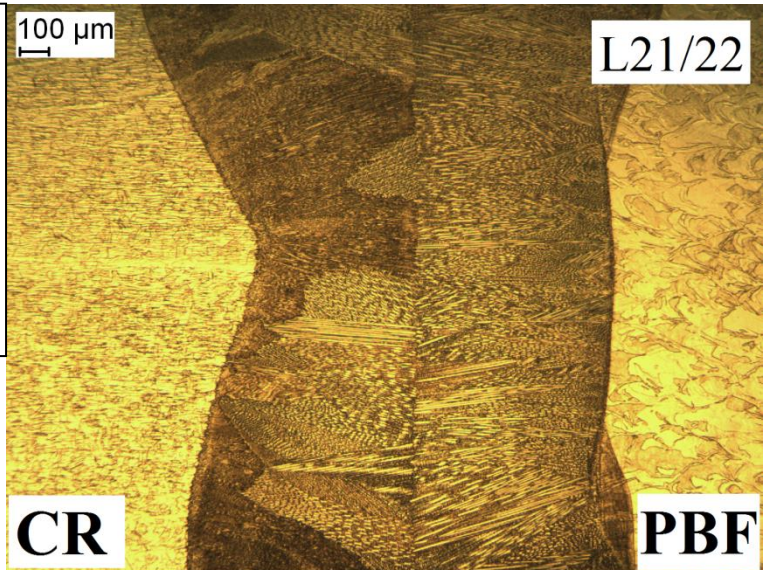
Sample: L17 and L18  
Solidification: A-F, F-A  
Optical fiber diameter: 300  $\mu\text{m}$   
Laser power: 4 kW  
Welding speed: 3000 mm/min  
Energy input: 80 J/mm



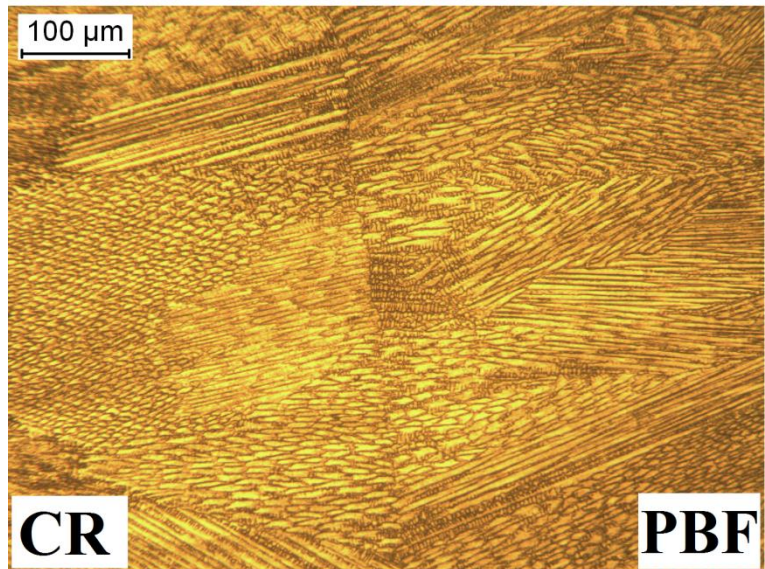
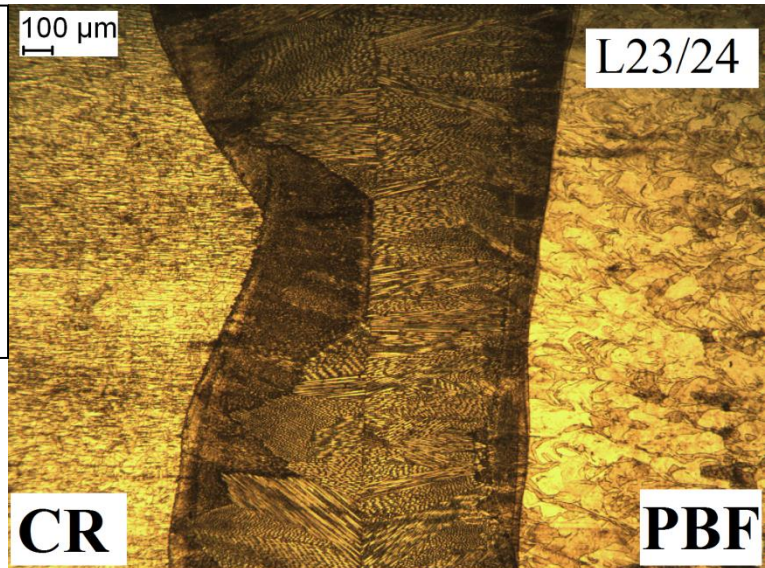
Sample: L19 and L20  
Solidification: A-F, F-A  
Optical fiber diameter: 300  $\mu\text{m}$   
Laser power: 4.5 kW  
Welding speed: 1000 mm/min  
Energy input: 270 J/mm



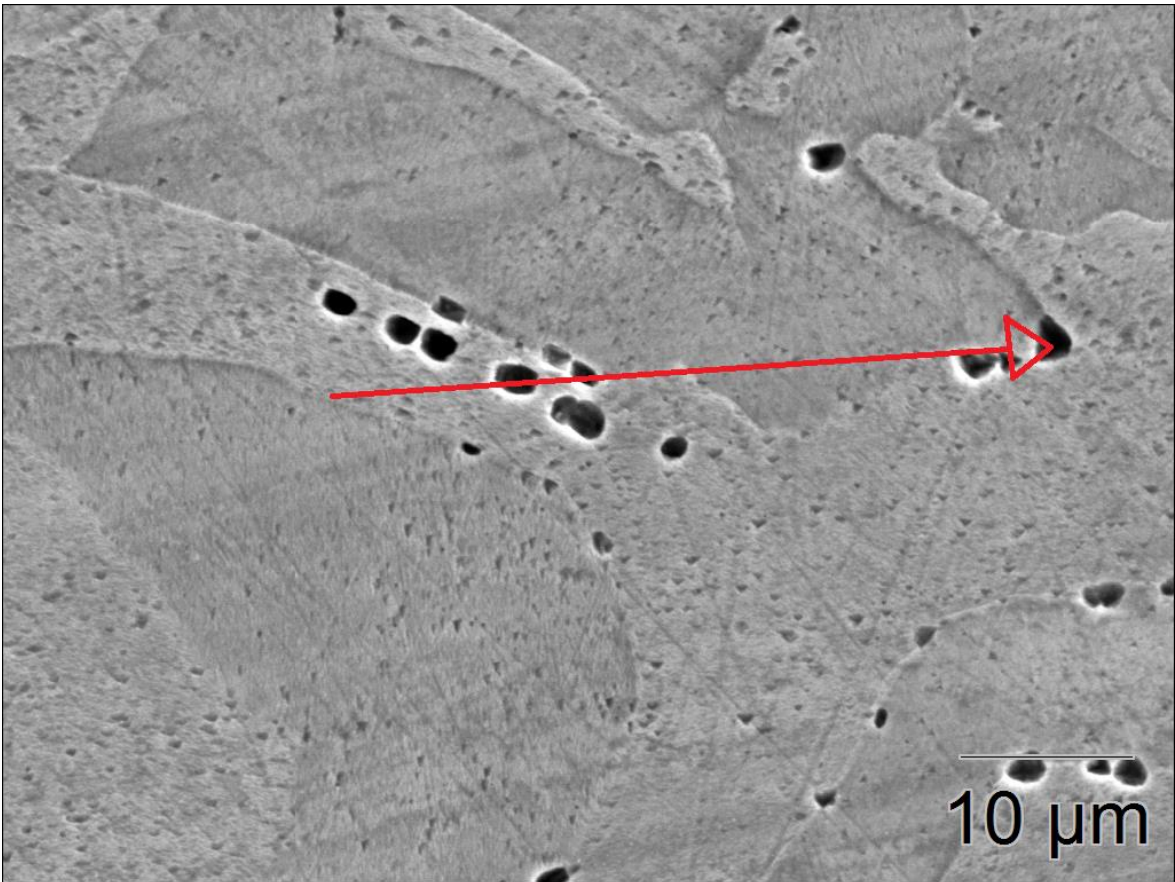
Sample: L21 and L22  
Solidification: A-F, F-A  
Optical fiber diameter: 300  $\mu\text{m}$   
Laser power: 4.5 kW  
Welding speed: 2000 mm/min  
Energy input: 135 J/mm



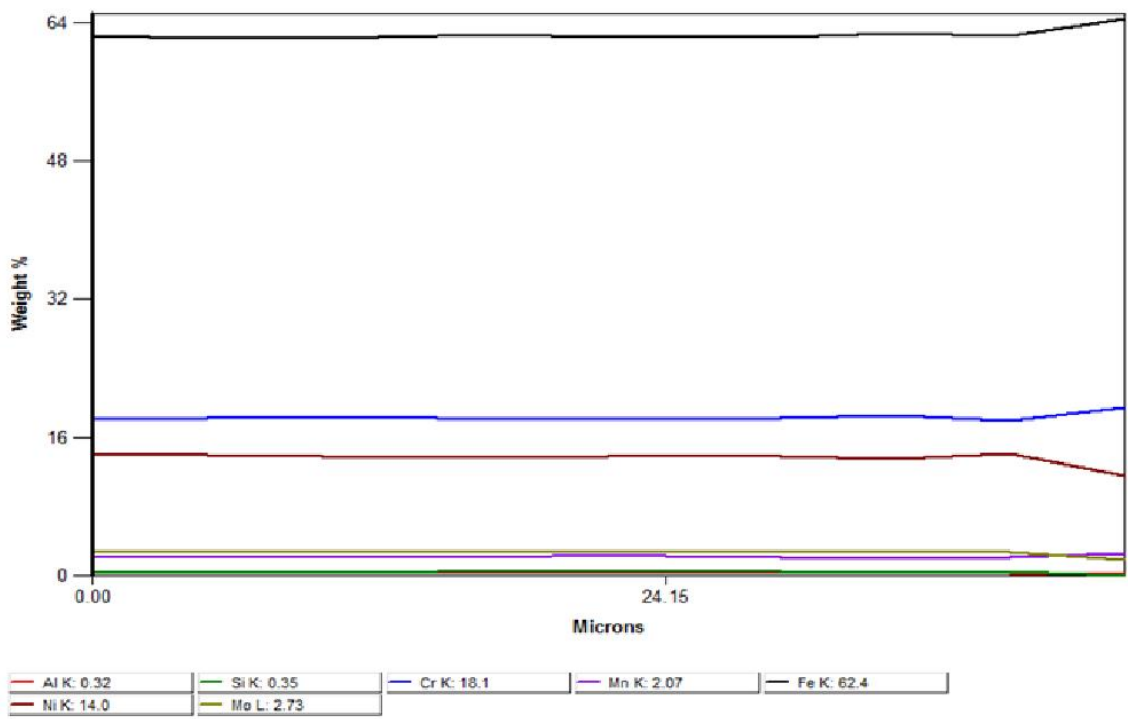
Sample: L23 and L24  
Solidification: A-F, F-A  
Optical fiber diameter: 300  $\mu\text{m}$   
Laser power: 4.5 kW  
Welding speed: 3000 mm/min  
Energy input: 90 J/mm

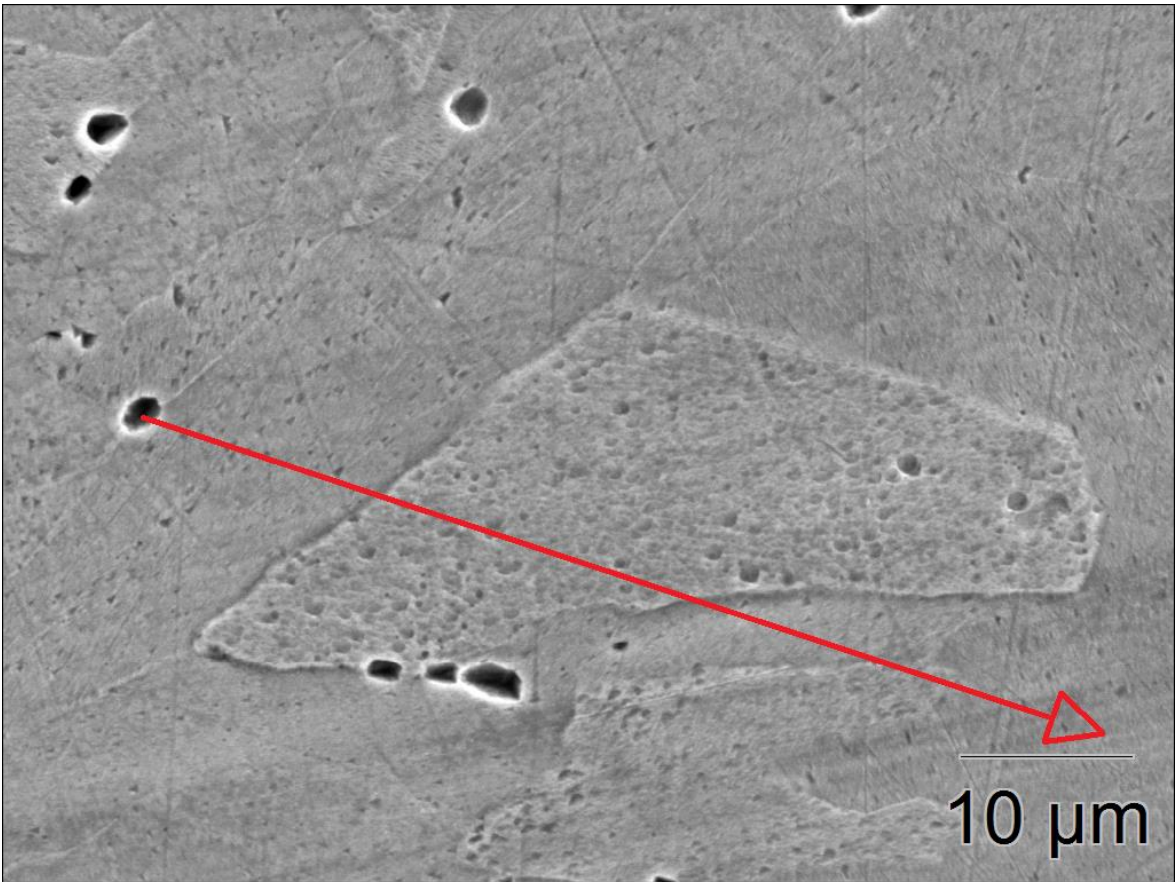


APPENDIX V, 1  
Energy-dispersive analysis

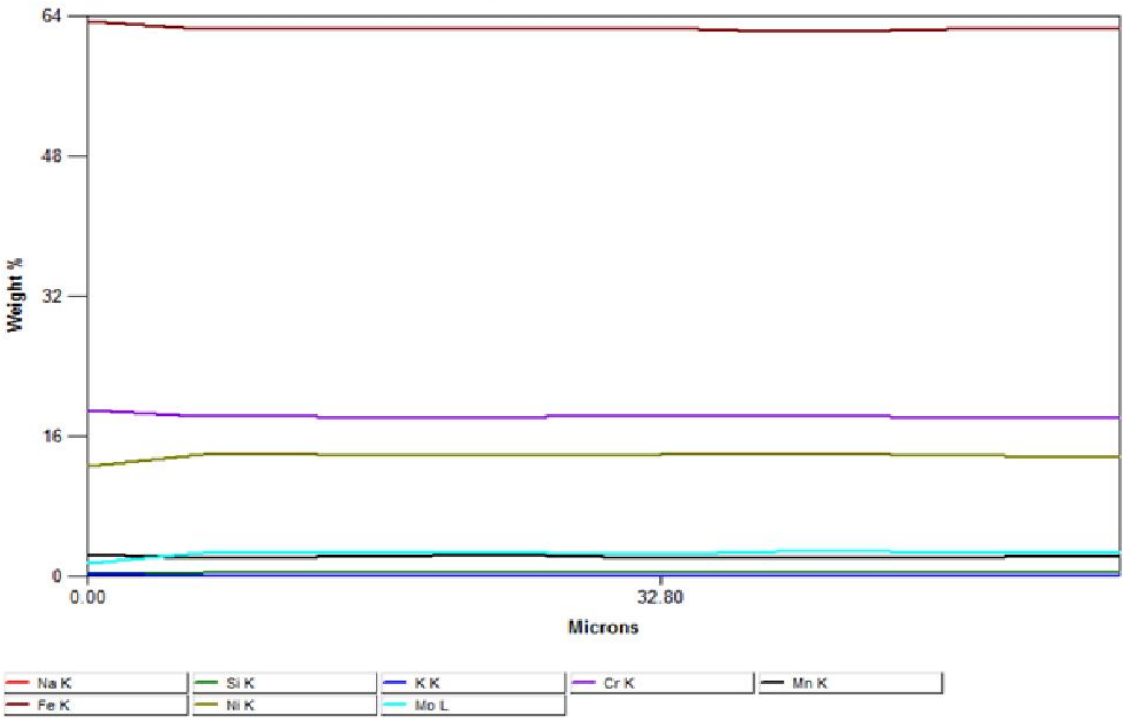


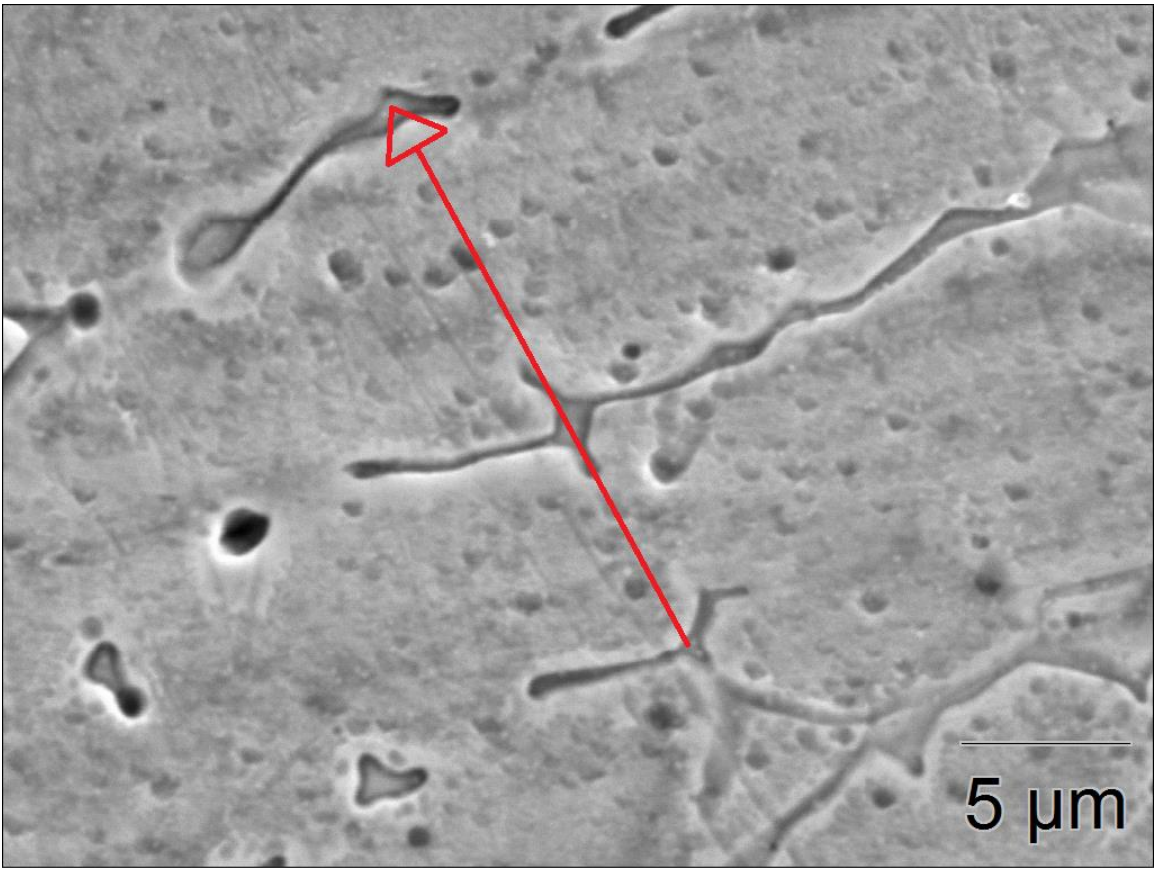
PBF 1



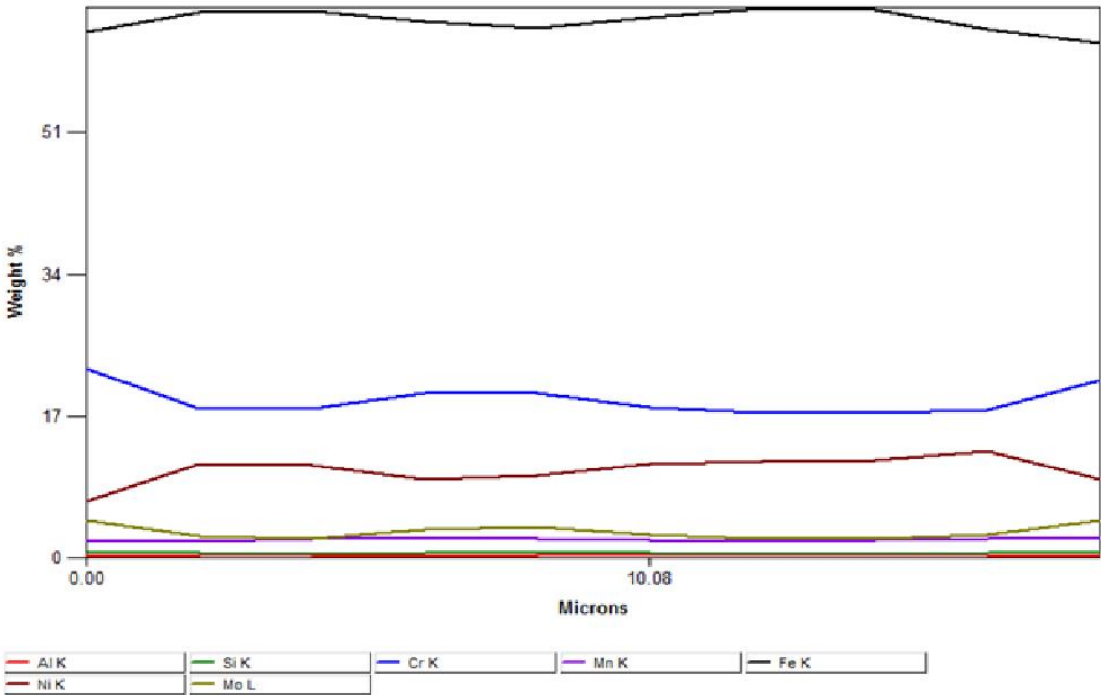


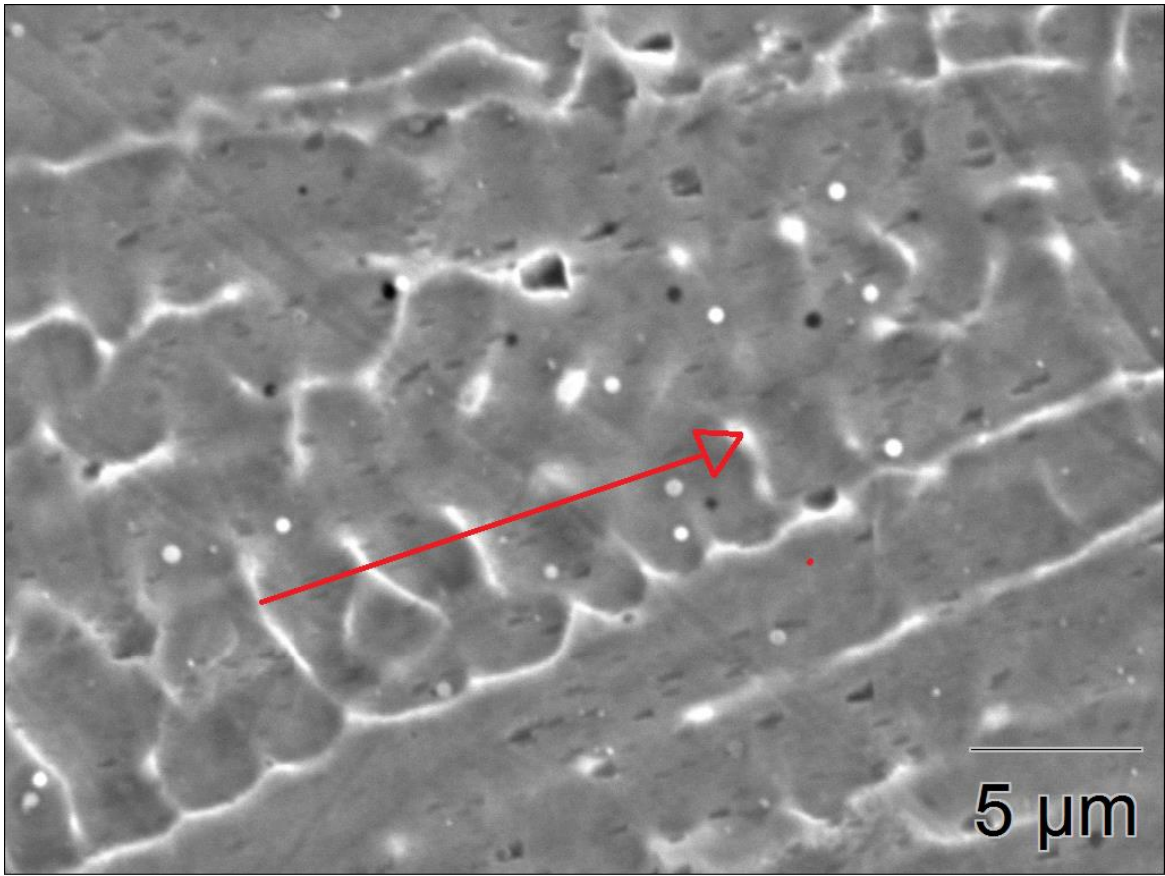
PBF 2



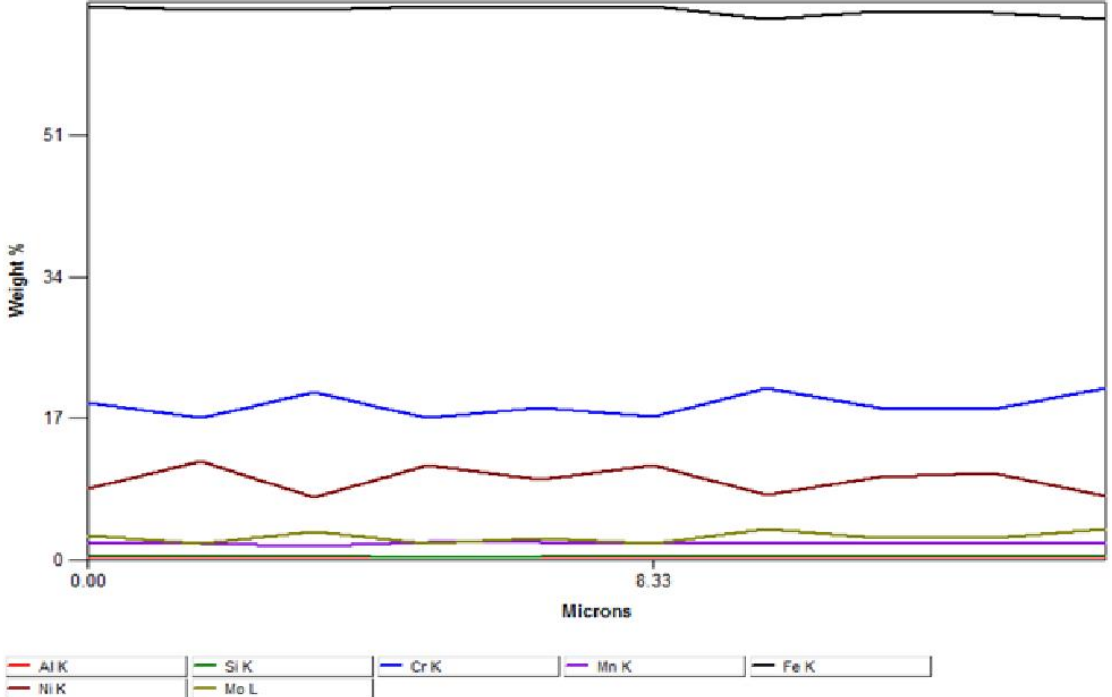


WELD 1





Weld 2



APPENDIX VI  
Results of the tensile tests

Test number	Ultimate tensile strength (MPa)	Elongation at break (%)	Location of the break
L1	547	36.2	Weld
L2	544	34.9	Weld
L3	549	44.5	PBF sheet
L4	560	45.9	PBF sheet
L5	553	42.4	PBF sheet
L6	553	44.9	PBF sheet
L7	550	36.4	Weld
L8	554	35.1	Weld
L9	553	36.7	PBF sheet
L10	555	38.7	PBF sheet
L11	557	31.8	PBF sheet
L12	557	41.2	PBF sheet
L13	545	29.0	Weld
L14	550	29.8	Weld
L15	548	46.1	PBF sheet
L16	558	43.1	PBF sheet
L17	555	43.9	PBF sheet
L18	553	44.3	PBF sheet
L19	547	30.8	Weld
L20	549	29.2	Weld
L21	555	43.9	PBF sheet
L22	555	45.1	PBF sheet
L23	555	41.4	PBF sheet
L24	560	44.2	PBF sheet